NASA Contractor Report 175013

Undercooling and Solidification Behavior in the InSb–Sb System

Jeffrey Alan Graves
University of Wisconsin
Madison, Wisconsin

September 1985

Prepared for the
Lewis Research Center
Under Contract NAS 3–14

National Aeronautics and
Space Administration

TABLE OF CONTENTS

INTRODUCTION

Rapid solidification of a material can have a variety of effects on the resulting product structure ranging from a reduction in microsegregation to the formation of supersaturated solid solutions, metastable intermediate phases or even amorphous solids. While the rapid cooling rates typically used to produce these structures preclude accurate measurement of the thermal history of the material, thermodynamic requirements alone often necessitate large undercoolings prior to the onset of nucleation.

An alternative approach to producing rapid solidification effects has been developed which allows both control and measurement of the nucleation undercooling using slow cooling rates. This technique involves the subdivision of a bulk ingot into droplets of size 10-150μm having a stable, non-catalytic surface coating.

The scale of a solidification microstructure is indicative of the rate at which solidification occurred and, as such, may be used to determine the thermal history of a sample. Often dendrite arm spacing measurements are utilized, however these spacings are subject to coarsening effects following their initial

formation in the undercooled liquid. An alternative measurement can be the interphase spacing of a eutectic alloy, particularly one in which low solid solubilities assist in minimizing post-solidification coarsening effects. This requires, however, that nucleation and growth of the solid take place within the coupled growth region and, furthermore, that this region be somewhat symmetric about the eutectic composition. A candidate system which offers both low solid solubilities and a melting range well suited to application of droplet techniques is the InSb-Sb eutectic alloy. This investigation thus focuses on evaluation of the undercooling and crystallization behavior of this faceted/faceted eutectic alloy in an attempt to correlate the solidification microstructure with the thermal history of the droplet sample. Once evaluated, this relationship may be used as a guide to estimate the undercooling experienced by droplets processed through alternative methods for which direct temperature measurements are difficult.

As a precursor to the examination of a eutectic alloy, it is desirable to evaluate the undercooling behavior of the pure constituents. As such, the initial stages of this investigation were devoted to

examination of pure Sb and InSb. The existence of high pressure polymorphic transitions in both materials offers the possibility of obtaining metastable structures in the undercooled droplet samples. Evaluation of the factors which influence undercooling behavior in the pure constituents assists in controlling the behavior of the eutectic alloy.

LITERATURE REVIEW

Undercooling

In the years since the development of rapid solidification processing techniques a wide variety of resulting structural modifications have been documented (1). These range from extensive refinement of the normal dendritic structure and grain size (2) to the formation of supersaturated solid solutions, metastable intermediate phases and amorphous solids (3, 16). Figure 1 illustrates the variety of microstructures often encountered following rapid solidification. While it is common to characterize these structures by the associated cooling rate employed to obtain them, it is of more fundamental importance to consider the level of undercooling attained prior to the onset of nucleation as well as during the subsequent rapid growth kinetics.

As a liquid is cooled below its thermodynamic melting point the available free energy can be dissipated by the formation of both equilibrium and nonequilibrium structures (4). Increasing the level of undercooling expands the number of reaction paths and product structures available to the system and allows competitive growth kinetics to play an important role in the evolution of

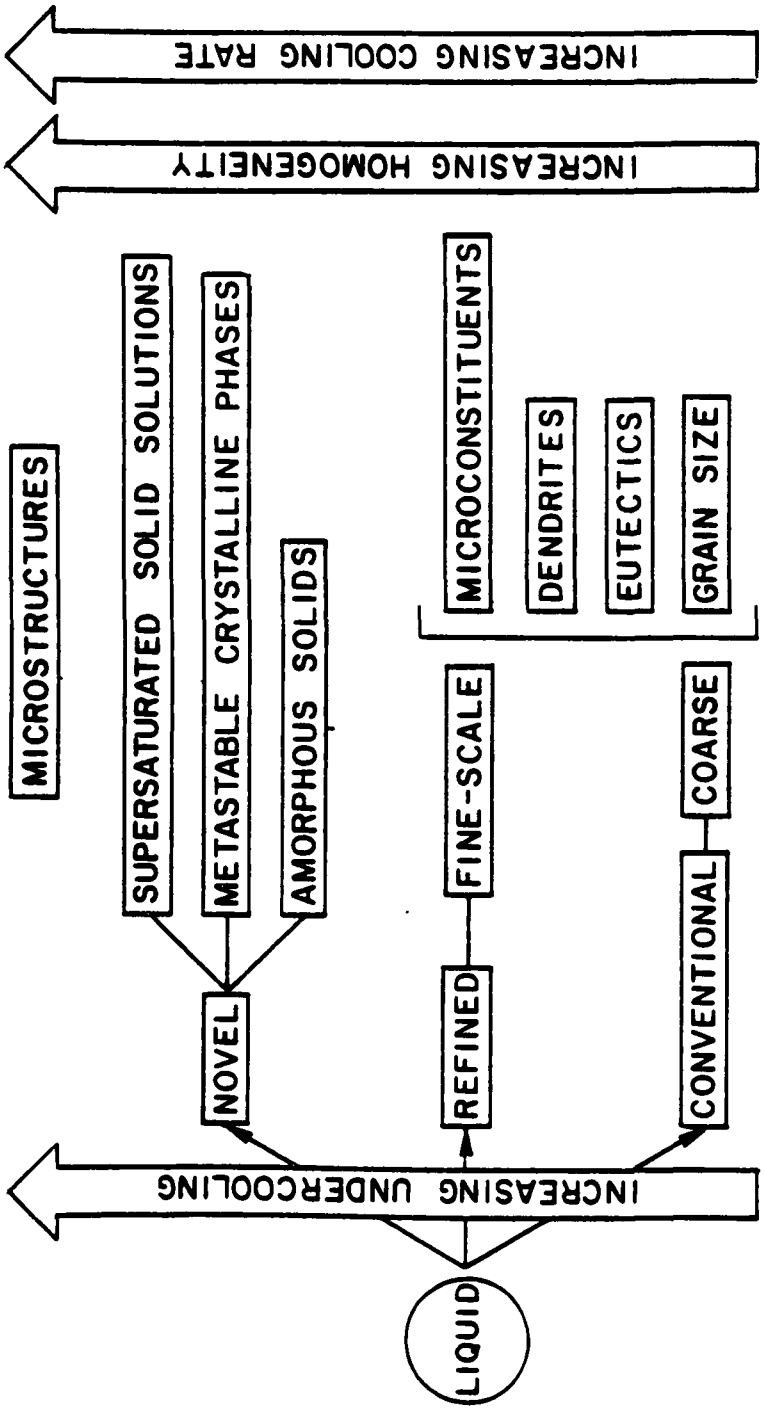

Figure 1. Microstructural consequences of undercooling.

different microstructural morphologies. Even at modest levels of undercooling (0.1 - 0.15T_m) obtained in some bulk melts, it has been possible to observe rapid solidification conditions and subsequent structural modifications (5).

If a liquid could be maintained under a condition in which it was exposed to no internal or external catalytic sites a maximum undercooling could be attained followed by the onset of a homogeneous nucleation process. In practice, however, the presence of residual nucleation sites acts to promote solidification at a lesser undercooling by a heterogeneous nucleation process. A more potent catalytic site requires less undercooling before solidification is initiated. When a material contains a number of nucleation sites of varying potency, the undercooling observed will correspond to the most potent site present under the specified cooling conditions.

Bulk materials typically solidify with small levels of undercooling. One of the primary reasons for this is the catalytic action of the mold wall. Successful attempts have been made to minimize the melt/mold interactions, enabling significant levels of undercooling (0.1 - 0.2T_m) to be attained in bulk materials.

One method involves enclosing the ingot in an inorganic glass crucible (6,7) which is believed to not only present the melt with a less catalytic surface, but also acts to deactivate potential nucleation sites within the liquid near the mold wall. Other methods which have produced significant undercoolings in bulk melts of Ni, Nb, and Fe-Ni alloys include levitation meltings (8,11) and solidification in drop tubes (9).

While impressive results have been obtained with bulk studies, by far the most effective means of achieving large undercoolings in a controlled manner is through the droplet method. The numerous nucleation sites contained in all bulk melts may be effectively isolated by subdividing the melt into a large number of fine droplets (10). The effect of this division is to isolate the most potent nucleants into a small fraction of the total droplet population such that the remainder may only be exposed to sites of lesser potency and thus achieve greater levels of undercooling prior to nucleation. There are several approaches to producing such a dispersion of droplets, some of which are illustrated in Figure 2, along with the glass encased bulk undercooling method.

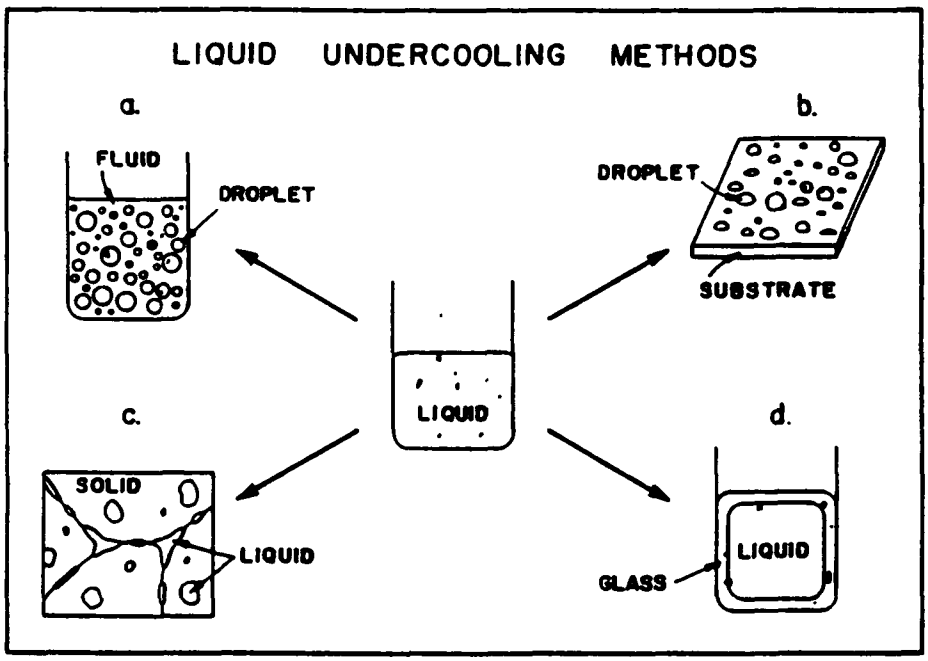

Figure 2. Illustration of the sample configuration for a variety of liquid undercooling methods.

The earliest detailed use of a droplet technique was noted by Vonnegut (12) who utilized both dilatometric and visual measurements to study the nucleation rate in tin and water droplets. Following this pioneering work, various refinements and modifications of the droplet technique occurred which have led to ever increasing undercooling levels being attained and recorded. One such development was the droplet substrate method (13) in which small droplets are placed on an inert glass substrate and melted under a controlled atmosphere. The onset of nucleation is then determined visually by noting either a change in the surface reflectivity of the droplet or the "blick" associated with droplet recalescence. Another is the entrained droplet technique (14,15) in which a bulk alloy sample is equilibrated in the two phase solid-liquid region with only a small fraction of the ingot existing as a liquid in contact with the primary solid solution. The undercooling of these entrained droplets may then be determined by thermal analysis. Other techniques which have been developed for droplet solidification studies include the use of exploding wires (17) and shotting (18). While most of the droplet techniques offer some means of temperature measurement, often the level of undercooling

is evaluated by a postmortem examination of the droplet microstructure. This is especially true of techniques which employ rapid cooling rates, such as atomization.

Of all droplet methods developed thus far, one of the most effective in allowing controlled undercooling studies to be carried out has been the droplet emulsion technique (19, 20). This technique involves dispersing a molten sample into a large number of fine droplets (10-20μ) in an appropriate carrier fluid such as oil or molten salt. This method not only provides effective isolation of the most potent catalytic sites into a small fraction of droplets, but also allows some degree of control over the droplet surface coating, whose nature often directly affects the level of attainable undercooling. While precise identification of the surface coating is often difficult, it may consist of metallic compounds such as oxides or sulfides, as well as a wide variety of other reaction products some of which may have complex crystalline structures or may even be amorphous. Such surface coatings should tend to "wet" the liquid phase to a larger extent than the solid phase and thereby discourage surface catalysis (19). Figure 3 illustrates the pronounced effect that a change in surface

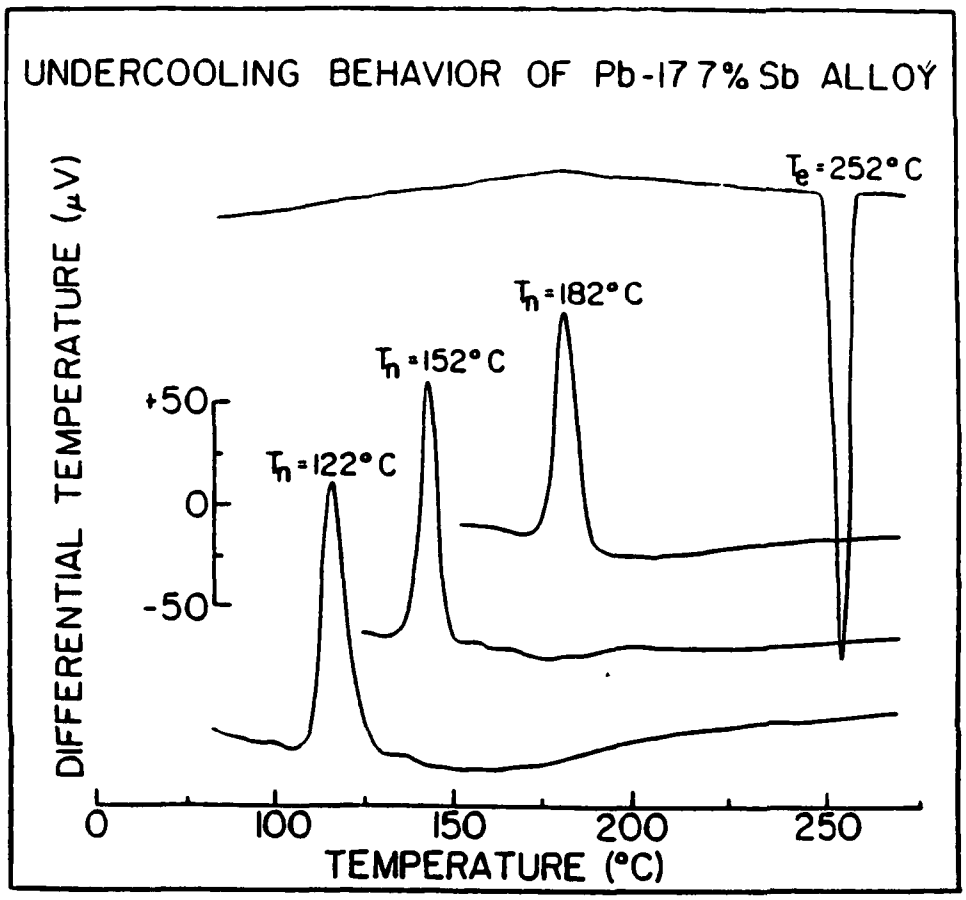

Figure 3. Effect of surface coating on level of undercooling for a Pb-17.7 at/o Sb droplet sample. (21)

coating may have on the level of undercooling obtained in a droplet sample of a Pb-Sb eutectic alloy. Such a variation in coating may be produced by the application of an appropriate chemical surfactant treatment during emulsification to similarly sized dispersions (21). Obviously this enhanced control over the level of undercooling allows for a more extensive control over the final solidification microstructure to be attained.

Of major importance in the droplet emulsion technique is the influence of droplet size on the undercooling behavior of a liquid. Figure 4 illustrates this dependence by a series of crystallization thermograms for high purity tin droplets (3), with the only system variable being the particle diameters (i.e. surface coating and cooling rate constant). The thermogram for the coarsest average particle size, $\bar{D} = 275\mu$, reveals a major crystallization exotherm at 184°C, an undercooling of 48°C, with several smaller exotherms extending to slightly lower temperatures. As the average particle size is decreased the initial exotherm at 184°C decreases in magnitude implying a smaller fraction of the droplet population is being affected by the catalyst corresponding to this level of undercooling. As this nucleation site is further isolated, other, less potent catalysts

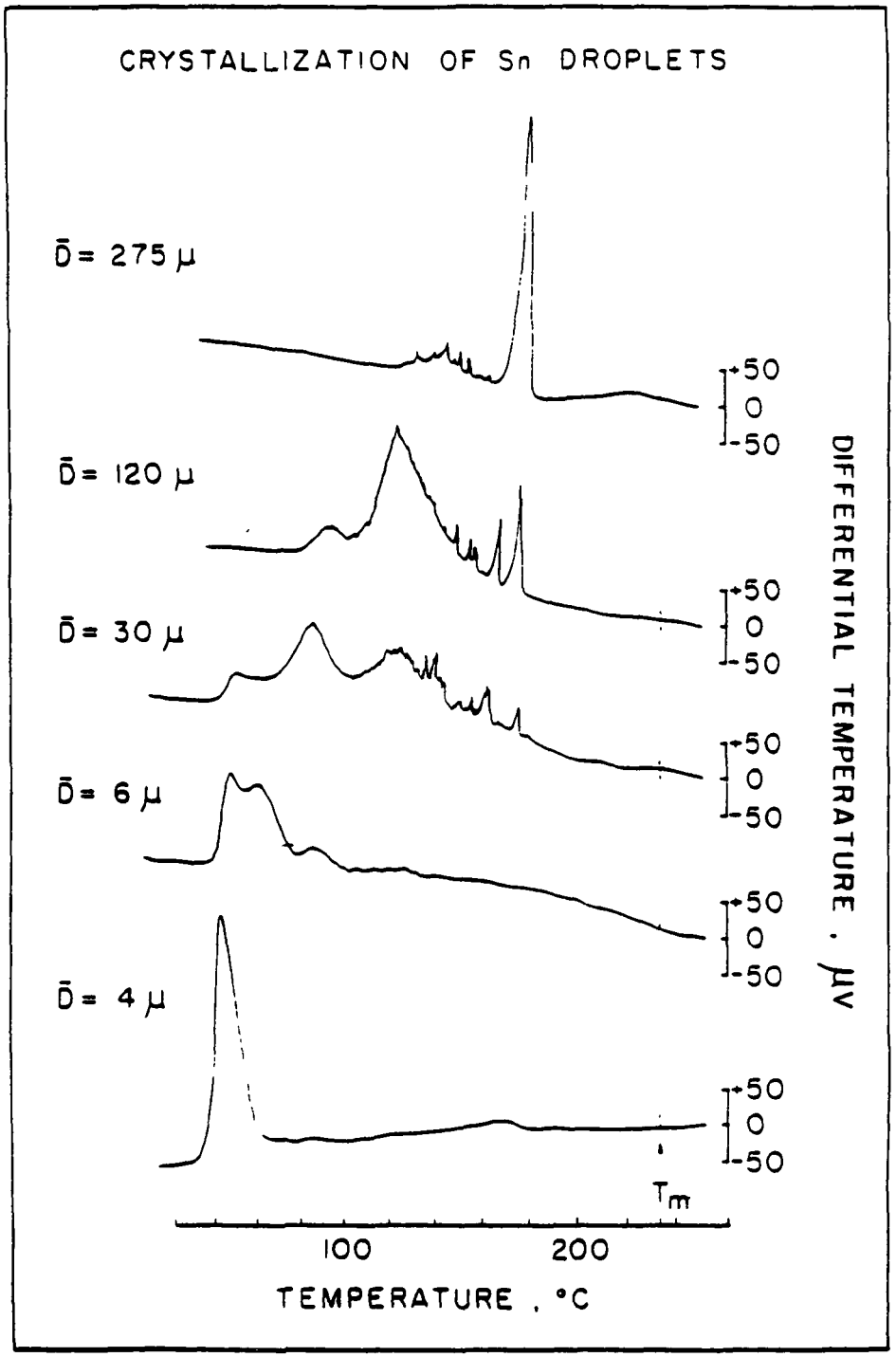

Figure 4. Effect of size refinement on the undercooling and crystallization of Sn droplets. (19)

are allowed to operate at deeper levels of undercooling in the remaining droplets. With each degree of size refinement further exotherms are observed at ever decreasing temperatures. The deepest undercooling are ultimately observed in the sample with the smallest average particle diameter as shown in the final thermogram, with $\overline{D} = 4\mu$. While it is convenient to describe each thermogram by the corresponding average particle diameter, it is also important to consider the size distribution of the droplet population. For $\overline{D} = 275\mu$ the size ranged from 160 to 400μ while at $\overline{D} = 30\mu$ the size range was 10 to 60μ. Finally at $\overline{D} = 4\mu$ droplet sizes from 1 to 9μ were observed. Therefore the deepest undercooling and most uniform crystallization behavior is observed in droplet samples with both a fine average particle diameter and a narrow size distribution, when all other system variables are held constant. It should be noted however that the appearance of a single crystallization peak at a large undercooling level in a droplet sample with a fine, narrowly distributed size range does not necessarily demonstrate the attainment of the maximum undercooling limited by homogeneous nucleation. This can only be concluded following a careful analysis of the size dependence of the nucleation rate for the

droplet sample (19). Based upon results obtained thus far, the droplet emulsion method offers an effective means of studying the undercooling behavior and solidification kinetics of both pure metals and alloys which can provide a basis upon which to evaluate the phase selection kinetics and microstructural development during rapid solidification processing treatments.

Nucleation Theory

a) Homogeneous Nucleation

The melting point of a material is defined thermodynamically as the temperature at which the free energy of the liquid is equal to that of the solid. Therefore as a liquid is cooled below this point there exists a driving force for solidification to occur which increases in magnitude with decreasing temperature. This volume free energy driving force, ΔG_v, may be expressed as a function of the latent heat, ΔH, and the level of undercooling, ΔT, for pure materials or dilute solutions, by the equation:

$$\Delta G_v = \Delta H \Delta T / T_m \qquad (1)$$

where T_m is the absolute melting temperature. This expression is, however, only an approximation due to the implied temperature independence of the latent heat

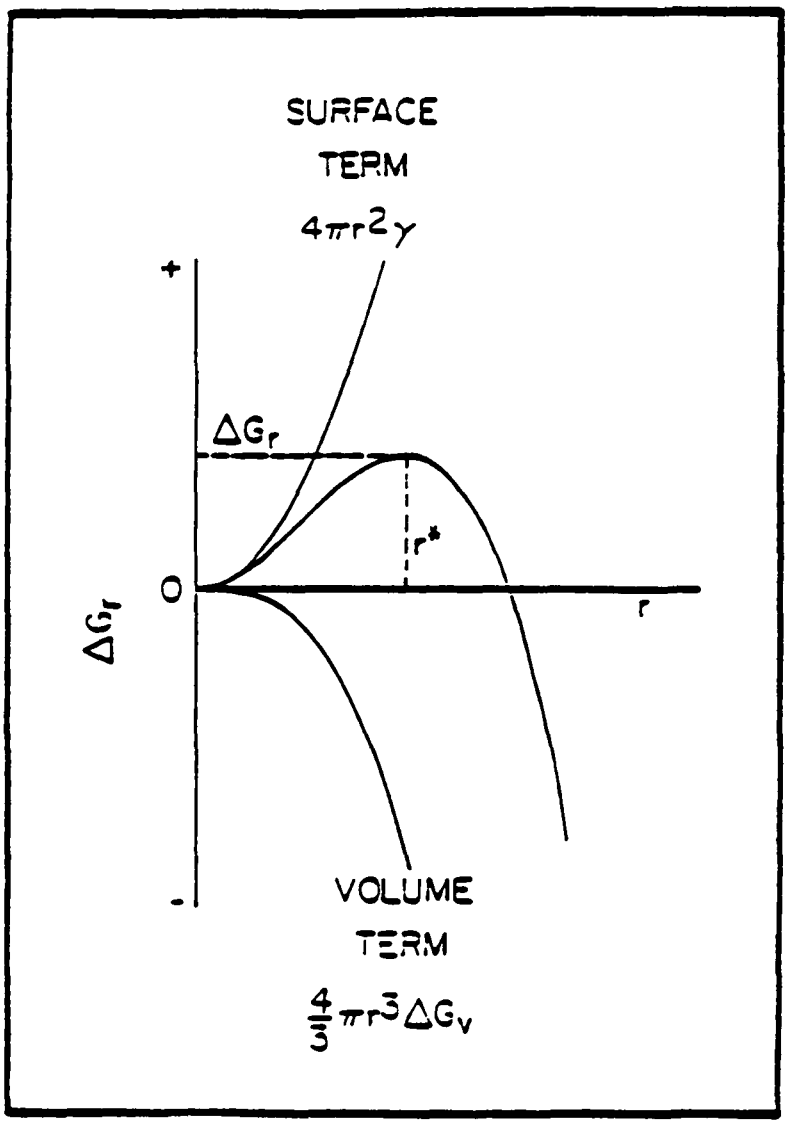

Figure 5. The free energy change associated with the formation of a spherical cluster of radius r.

of fusion. Opposing the liquid to solid transformation is the necessity of creating an interface between the phases. The associated surface energy, $\gamma_{s/l}$, acts to increase the free energy of the system, thus inhibiting nucleation. The contribution of the two opposing factors to the overall free energy associated with the formation of a spherical cluster of radius, r, may be expressed by:

$$\Delta G = 4/3\pi r^3 \Delta G_v + 4\pi r^2 \gamma_{s/l} \qquad (2)$$

and is illustrated in Figure 5. For very small clusters the surface term dominates and the net free energy increases with increasing r. However, once a critical size (r*) is reached, the volume term dominates and any further increase in size will lead to a decrease in the total free energy of the system. By maximizing the expression for ΔG, the critical radius is given by:

$$r^* = -2\gamma_{s/l} / \Delta G_v \qquad (3)$$

and the corresponding critical free energy of formation is given by:

$$\Delta G(r^*) = 16\pi \gamma_{s/l}^3 / 3\Delta G_v^2 \qquad (4).$$

This expression for the critical free energy then represents the barrier to the formation of a spherical cluster of critical size or, in other words, the barrier to "homogeneous nucleation".

According to classical theory, the steady state homogeneous nucleation rate, J_s, may be expressed as (22):

$$J_s = ZD^*C_o(n^*) \qquad (5)$$

where D^* is the impingement frequency of atoms on a critical cluster, $C_o(n^*)$ is the equilibrium concentration of critical clusters which can be expressed as a function of ΔG^* by:

$$C_o(n^*) = C\exp(-\Delta G^*/kT) \qquad (6)$$

where C is the concentration of unassociated atoms, k is the Boltzmann constant, T is the nucleation temperature, and Z is the Zeldovich "nonequilibrium constant" representing the nonequilibrium concentration of critical clusters in the system. By combining equations (4), (5) and (6) an expression may be developed for the homogeneous nucleation rate as a function of common material parameters and the level of attained undercooling prior to nucleation:

$$J = K_v\exp(-16\pi\gamma_{s/l}^3 T_m^2 / 3kT\Delta H^2\Delta T^2) \qquad (7)$$

where K_v is a combined prefactor on the order of $10^{42}m^{-3}sec^{-1}$ (23). Using reasonable values for the solid/liquid surface energy, equation (7) predicts that the required undercooling for nucleation of the solid is large. It has been repeatedly demonstrated however that typical undercoolings prior to nucleation are relatively

small unless extreme conditions are imposed. The seeming dichotomy may be resolved by consideration of the effect of nucleant catalysts on nucleation behavior.

b) Heterogeneous Nucleation

The primary effect of nucleation on a foreign body, or "heterogeneous nucleation", is to decrease the surface energy created by embryo formation and thereby reduce the barrier to nucleation. Classical theory depicts the embryo as a spherical cap forming on the foreign body, or catalyst, as illustrated in Figure 6. A catalyst may then be characterized by the associated "wetting angle", θ, which reflects the potency for nucleation on that substrate. As θ approaches 0^{o}, more complete wetting of the substrate by the embryo occurs and less undercooling is attained prior to nucleation. For θ approaching 180^{o}, less wetting occurs and the undercooling tends toward the limit imposed by homogeneous nucleation. In order to express this catalytic effect in the nucleation equations, an expression may be developed for the "contact angle function", $f(\theta)$:

$$f(\theta) = (2+\cos^{3}\theta - 3\cos\theta) / 4 \qquad (8).$$

This function may then be incorporated into the nucleation rate expression by first modifying the nucleation

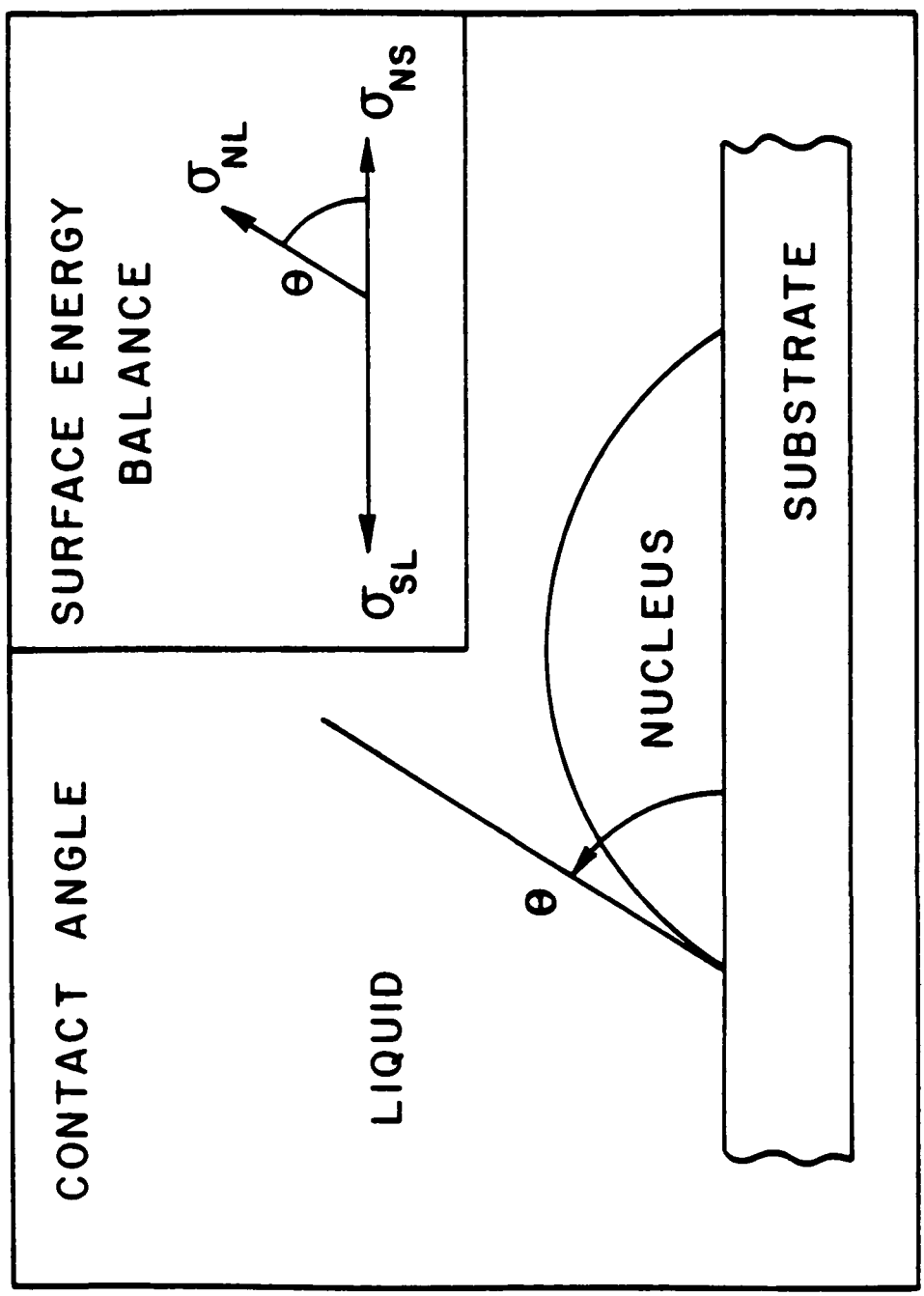

Figure 6. Heterogeneous nucleation of a spherical cap on a substrate.

barrier to reflect the effect of the catalyst. Equation (4) then becomes:

$$\Delta G^*_{het} = \Delta G^*_{homo} f(\theta) \qquad (9)$$

and subsequently the heterogeneous nucleation rate expression is given by:

$$J = K_s \exp(-16\pi\gamma^3_{s/l} T_m^2 \,/\, 3kT\Delta H^2 \Delta T^2 \cdot f(\theta)) \qquad (10)$$

where K_s is on the order of $10^{31} m^{-2} sec^{-1}$ (24). Thus each catalytic site in a system has associated with it a discrete contact angle function and therefore a unique nucleation rate expression. This, in turn, may be used to explain the results obtained in droplet experiments in which sites of lesser potency are allowed to operate by isolation of the more potent catalytic sites into a small fraction of the droplet population.

c) Nucleation Kinetics

Examination of the nucleation rate expressions, (7) and (10), can assist in understanding the phase selection kinetics operating in an undercooled liquid. The exponential term dominates the overall net rate so that the phase with the lowest barrier to nucleation, ΔG^*, will be favored at any given level of undercooling.

Also of interest in the examination of nucleation kinetics is the effect of the imposed cooling rate on

phase selection. This can best be demonstrated by considering a series of time-temperature-transformation curves for both heterogeneous and homogeneous nucleation cases, as depicted in Figure 7. These curves are characterized by their C-shape which is indicative of the thermally activated nucleation process. In the diagram, curve A represents homogeneous nucleation while B and C are heterogeneous curves which could correspond to catalytic sites of varying potency and/or different solid phases which could nucleate from the liquid. The phase which ultimately nucleates will be determined by the point of intersection between the C-curves and the superimposed cooling curve. As the cooling rate is increased it is possible to attain deeper undercoolings and possibly shift from one nucleation site to another or one product structure to another. At sufficiently high cooling rates (which may vary between systems) it may even be possible to bypass the homogeneous nucleation limit such that a glass transformation is obtained before the nucleation of a crystalline phase occurs. Examples of this have been documented for many systems using splat cooling techniques with their associated rapid cooling rates.

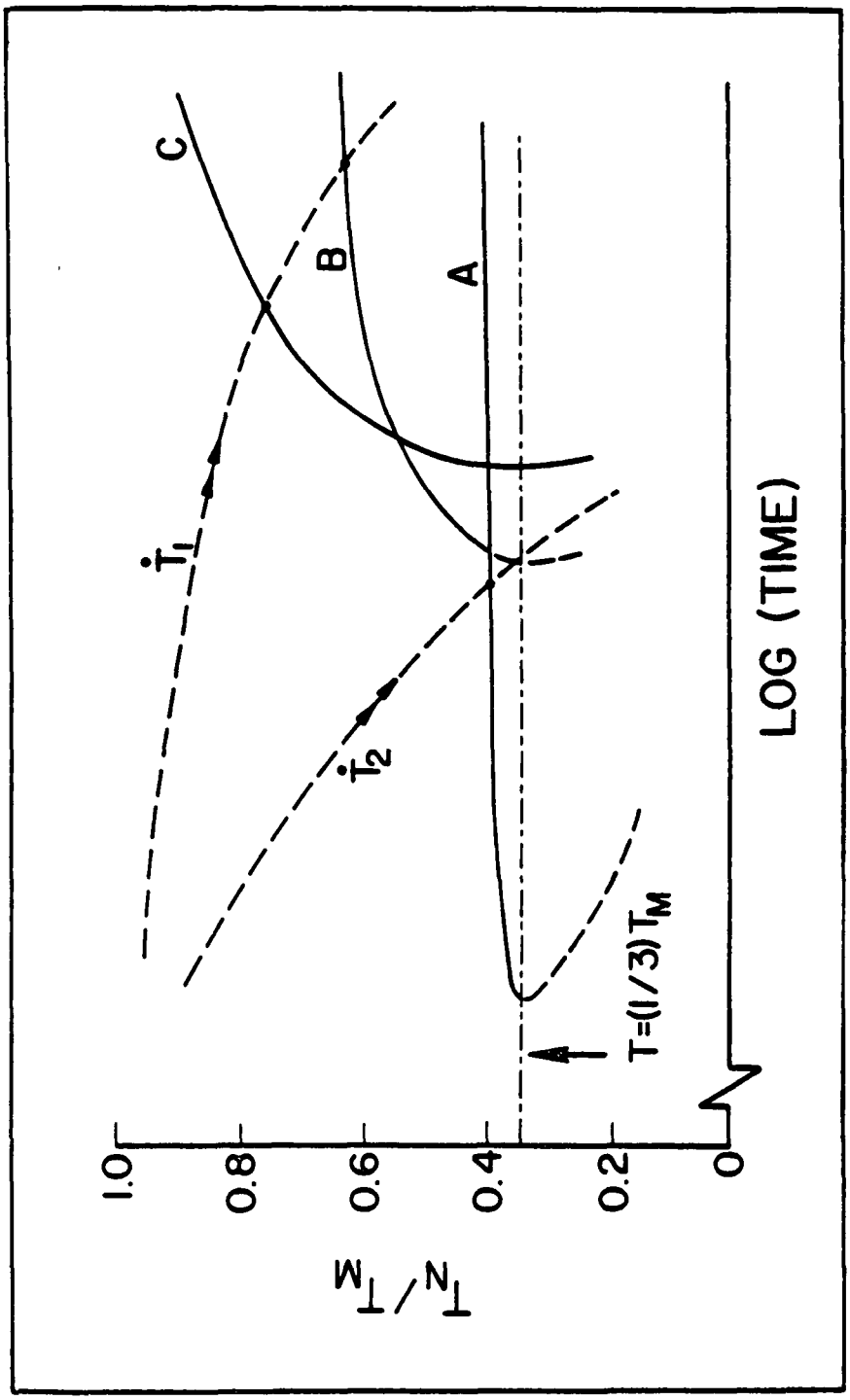

Figure 7. A series of time-temperature-transformation curves for both homogeneous (A) and heterogeneous (B,C) nucleation.

Growth Kinetics

Following the nucleation of a solid from its melt, growth occurs by the addition of atoms at the advancing solid/liquid interface until the transformation is completed. The mechanism by which atoms attach themselves to the interface is central to the growth process, as it affects both the rate at which the transformation occurs and the resulting solidification morphology. In order to consider the various growth mechanisms and the conditions under which they operate, it is helpful to examine first the nature of the solid/liquid interface.

Theories concerning the detailed description (on an atomic scale) of the solid/liquid interface evolved from studies on the growth of crystals from the vapor phase (32). This approach led initially to the designation of two distinct types of interface and thus two corresponding growth mechanisms. Figure 8a depicts an atomically flat interface in which the transition from liquid to solid is envisioned to take place across a single atomic layer. Motion of such an interface occurs by the propagation of steps parallel to the interface, with the front advancing a single step-height with the passage of each successive layer. This is known as "lateral (stepwise) growth". A second type of interface, which was

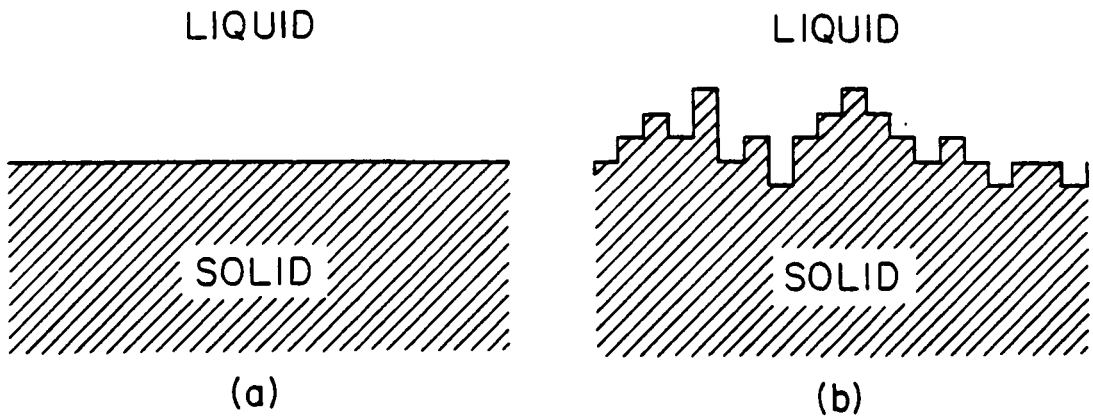

Figure 8. Illustration of both ideally flat (a) and rough (b) solid/liquid interfaces.

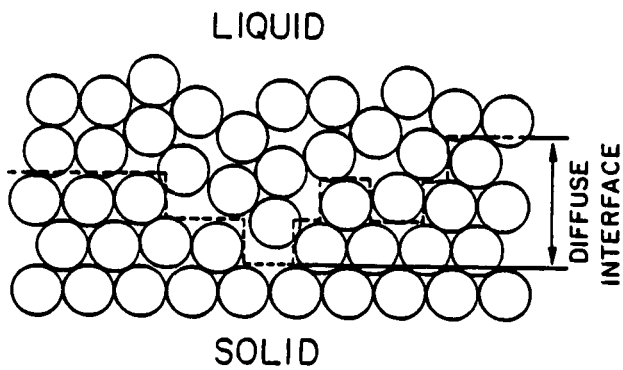

Figure 9. A more realistic depiction of an atomically diffuse interface in which atoms gradually move from the disordered liquid to their equilibrium positions in the solid.

thought to exist at higher temperatures, is shown in Figure 8b. This is termed a "diffuse (or rough) interface" and may be characterized by a gradual transition from liquid to solid across a number of atomic layers. For an ideally diffuse interface most lattice sites are favorable for atomic attachment and so propagation of the front is relatively uniform and growth is said to be "continuous". Early theories on crystal growth from the melt considered the solid/liquid interface to be similar to that of the ideally diffuse type and thus predicted that a continuous growth mechanism should always dominate (25). However, subsequent experimental evidence forced modification of this idea by demonstrating that a certain critical driving force must be attained in order for continuous growth to occur (26). This required driving force varies between systems, becoming smaller as the interface becomes rougher (i.e. more diffuse). Using an approach suggested by Jackson (27), the degree of roughness of an interface may be qualitatively evaluated by consideration of common material parameters. The two-level model used in this approach depicts an initially flat interface upon which atoms are randomly added. An assumption is made that the probability of any atom having a neighbor is proportional to the

fraction of surface sites which are filled. The free energy change associated with filling a fraction, x, of surface sites is then given by:

$$\Delta F_s / NkT_m = \alpha x(1-x) + x\ln x + (1-x)\ln(1-x) \quad (11)$$

where N is the number of surface sites, k is the Boltzmann constant and T_m is the equilibrium melting temperature. The α parameter in equation (11) may be expressed as:

$$\alpha = (L/kT_m)\xi \quad (12)$$

where L is the latent heat and ξ is the fraction of the atomic binding energy associated with the layer. For small values of α (≤ 2) the interface is atomically rough and the corresponding critical driving force for continous growth is small. For large values of α (≥ 2) the model predicts an atomically smooth interface and that the critical driving force is relatively large. The ξ term in equation (12) varies from zero to one, attaining its largest value for the closest packed face. Also, the term L/kT_m may be equivalently expressed as $\Delta S/R$, where ΔS is the entropy of fusion and R is the molar gas constant. Thus, the atomic details of the solid/liquid interface and the primary growth mechanism may be qualitatively assessed by consideration of the entropy change and orientation of the crystal during the solidification

process. Table I presents typical values of $\Delta S/R$ for a variety of selected materials (27). An additional advantage of using the α parameter to distinguish probable growth mechanisms is that it also provides a convenient means by which to predict the solidification morphology of a material. Metals (with small $\Delta S/R$) tend to exhibit rounded interfaces characteristic of uniform growth, while materials with larger $\Delta S/R$ values tend to exhibit faceted interfaces characteristic of a lateral growth mechanism.

While the distinction between lateral and continuous growth is most easily illustrated in relation to a particular type of interface, it is more realistic to picture the solid/liquid interface as a region in which atoms gradually move from a relatively disordered liquid configuration to the equilibrium positions in the solid state (29). Such a treatment, as depicted in Figure 9, implies that the interface may always be characterized by some degree of diffuseness, however, the degree will vary between systems and between crystal planes within a particular system. Theoretically, the existence of a diffuse interface does not preclude the requirement of growth by a lateral mechanism at sufficiently low driving forces (28). Thus, crystal growth from the melt may

TABLE I

$\Delta S/R$	MATERIAL	TYPE
1	Metals	ionic
2-4	Ge, Bi, Sb, Ga	crystals
4-8	most organic materials	organic
8-50	complex molecules	crystals
>100	polymers, etc.	

in general, be described as the advance of an atomically diffuse interface which has an associated driving force below which growth occurs by the lateral motion of rudimentary steps. At higher driving forces a transition in growth regimes gradually occurs which is bounded at some critical level by a continuous growth mechanism.

Criteria have been developed which can quantitatively predict the regimes of the alternative limiting growth mechanisms based upon the magnitude of the free energy change per unit volume, ΔF_v, or in other words, the driving force for solidification (28). The driving force may be expressed as:

$$\Delta F_v = (L\Delta T/V_m T_m) \qquad (13)$$

where V_m is the molar volume of the solid and ΔT is the undercooling. At low driving forces lateral growth mechanisms dominate with the upper free energy bound for this regime being:

$$\Delta F_v^* = -\sigma g/a \qquad (14)$$

where σ is the interfacial energy, a is the step height and g is a "diffuseness parameter" whose value depends sensitively on the number of atoms comprising the transition from liquid to solid at the melting point. For sharp interfaces g is on the order of 1 with the value decreasing rapidly as the interface becomes more diffuse.

As the driving force increases a transition from lateral to continuous growth gradually occurs, with the continuous mechanism becoming dominant for:

$$\Delta F_v^{**} > -\pi g\sigma/a \qquad (15).$$

Thus the growth mechanism which ultimately prevails will depend upon both the thermodynamic driving force (or undercooling) and the degree of diffuseness of the interface. As such, all materials should theoretically possess conditions under which growth will occur by both lateral and continuous mechanisms, however, for very diffuse interfaces (i.e. $g \to 0$), the transition to continuous growth occurs at such a low driving force that experimental observation of the actual transition becomes exceedingly difficult (26, 29).

One of the most effective means of characterizing a particular growth mechanism is through its associated rate expression. Experimentally, this implies that measurements of growth rate as a function of undercooling may be directly related to the operating crystal growth mechanism (26). In developing general rate expressions for lateral growth, it is necessary to distinguish between the various subdivisions of this category based upon the origin of the surface steps. For a crystallographically perfect surface, steps must

originate by a two-dimensional nucleation process along the interface. This requires the attainment of some minimum undercooling, the level of which will vary between systems, prior to obtaining any significant growth. In studies on tri-α-naphthylbenzene (30) and pure Gallium (31) lateral growth by a two-dimensional nucleation process appears to operate, with the required undercoolings for observable growth being 2° and 0.5° C respectively. At greater levels of undercooling the nucleation of new steps becomes so rapid that the observed growth rate approaches that which would be expected for a continuous growth mechanism.

While two-dimensional nucleation of steps may be required for a perfect interface, two types of crystallographic imperfections are known to enhance the lateral growth rate by providing a perpetual source of steps (26): (1) dislocations which terminate on the surface having Burgers vectors lying out of the interfacial plane (such as screw dislocations); (2) multiple twins which terminate on the surface thereby forming re-entrant grooves. For a crystal with a screw dislocation emerging at the solid/liquid interface the close-packed face cannot be flat, but must instead contain a step. This surface step not only obviates the need for two-dimensional

nucleation and the associated minimum undercooling requirement, but will also be self-perpetuating as it winds continuously about the dislocation terminus with the addition of each new atomic layer (32). An expression for the crystal growth rate, G, associated with this lateral mechanism has been developed by Cahn et al. (26) and is given by:

$$G = \frac{\beta(1+2g^{1/2})}{g} \cdot \frac{D_L L^2 (\Delta T)^2}{4\pi R\sigma V_m T_m^3} \qquad (16)$$

where D_L is the diffusivity of the liquid and β is a modifying factor which may be expressed as:

$$\beta = 6(a/\lambda)^2(\nu_{LS}/\nu_L) \qquad (17)$$

where λ is the mean jump distance in the liquid and ν_{LS} and ν_L are the jump frequencies onto the solid interface and within the liquid respectively. Figure 10 illustrates both the parabolic relationship between growth rate and undercooling for this mechanism as well as the effect of interface diffuseness on the extent of this growth regime. As the interface becomes more diffuse deviation from equation (16) occurs at smaller undercoolings. The operation of this dislocation mechanism of lateral growth has been well documented, particularly for various organic materials such as β-Methylnaphthalene and Salol (26).

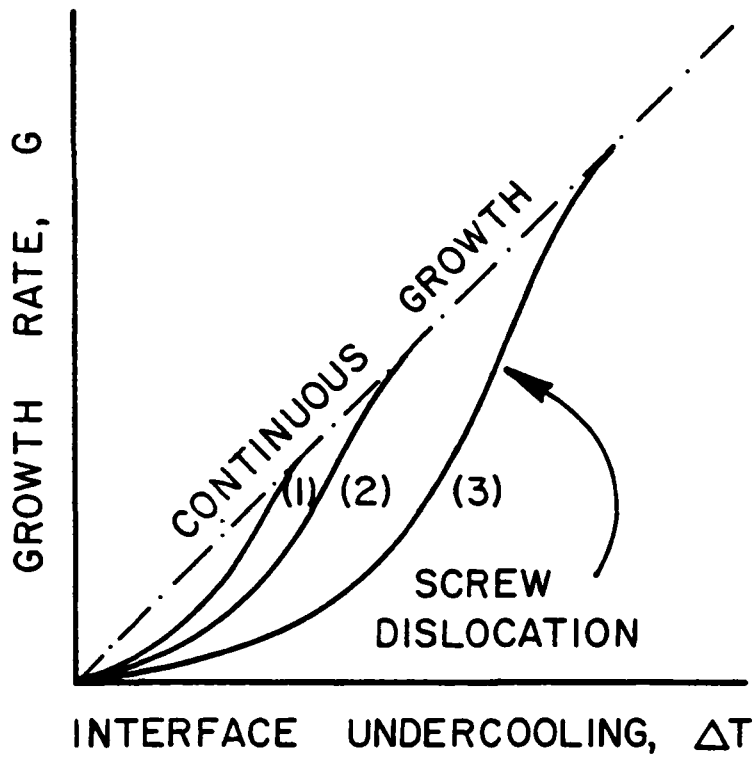

Figure 10. Illustration of the parabolic relationship between crystal growth rate and interfacial undercooling for the operation of a screw-dislocation growth mechanism. Curve 3 represents an atomically flat interface ($g=1$) while curves 2 and 1 hold for increasingly diffuse interfaces ($g \to 0$).

Based upon early experimental observations on the growth of Germanium crystals in undercooled melts (33), Wagner (34) and Hamilton and Seidensticker (35) proposed a second source of crystal imperfection which could enhance lateral growth. In this model, which requires a minimum of two twin planes, growth begins at the re-entrant corners which are formed by the intersection of habit faces on either side of the twin planes. Growth is rapid in these grooves because of favorable nucleation on the step occurring at the center line which, in turn, encourages atom layers to quickly spread over the entire surface of the groove. Furthermore, these favored growth sites will not disappear, but instead will allow growth to continue indefinitely in two or more of the favored growth directions. The resulting crystal will thus have a strong tendency to exhibit sixfold $\langle 211 \rangle$ propagation and branching with the product structure being bounded by flat, close-packed $\{111\}$ planes (35). While no corresponding kinetic law for re-entrant twins has been developed, this growth mechanism has been experimentally observed in systems other than Germanium which also have the diamond or zinc-blende structure such as InSb and Si (36).

When the solidification driving force exceeds the limit set by equation (15) crystal growth should occur

by continuous advance of the interface thereby circumventing the need for step formation and propagation as required for lateral growth. An expression has been developed which describes the variation in observed growth rate with undercooling for continuous growth which is given by (26):

$$G = \beta D_L L \Delta T / a R T_m^2 \qquad (18).$$

Thus the growth rate described by a continuous mechanism should vary linearly with undercooling and will have a non-zero value at all undercooling levels. At intermediate driving force values (between the bounds set by equations (14) and (15)) a smooth transition in growth kinetics occurs implying a change from a lateral to a continuous growth mechanism in this region. Figure 11 illustrates the three growth regimes, lateral ("classical"), transitional and continuous, with the boundaries being expressed in terms of undercooling. As defined by Cahn et al. (26), ΔT^* is given by:

$$\Delta T^* = -\sigma g V_m T_m / aL \qquad (19).$$

Thus in terms of undercooling, the observed transition in growth kinetics occurs between the bounds set by ΔT^* and $\pi \Delta T^*$, with the extrapolated intersection of the two limiting regimes occurring at an undercooling of $4\pi\Delta T^*$.

One of the most important practical consequences of

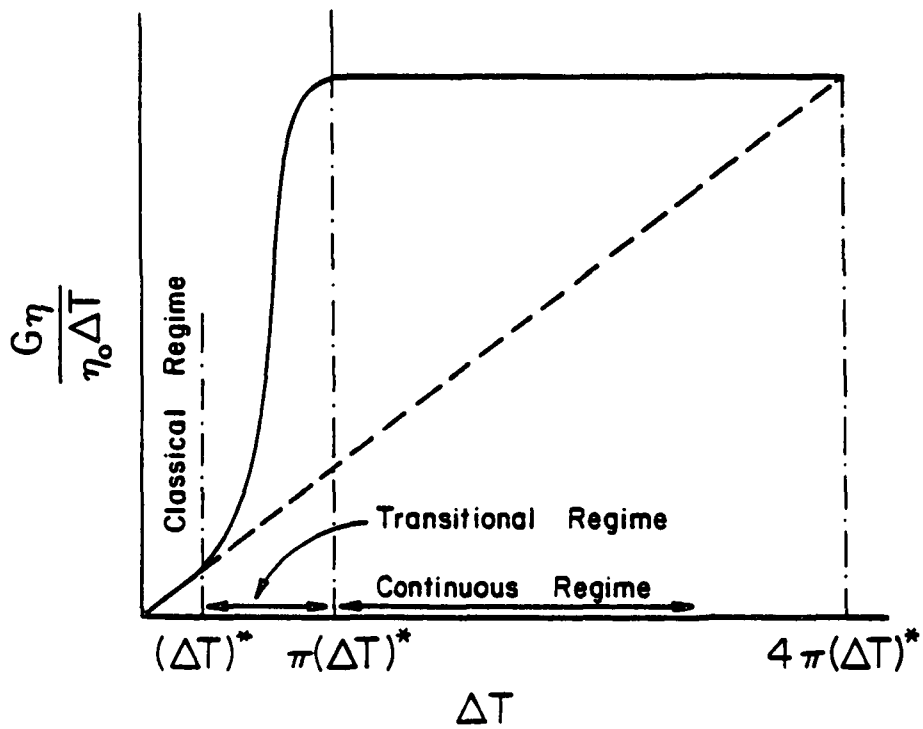

Figure 11. Illustration of the transition in growth mechanisms from lateral ("classical") at low undercoolings, through a transitional region and ultimately to continuous growth at larger interfacial undercoolings. Note that the growth rate has been adjusted for the temperature dependence of the melt viscosity. (26)

the operation of a particular growth mechanism in a system is that it will be directly reflected in the resulting morphology. Materials in which growth is primarily by a lateral spreading mechanism will exhibit faceting on low index faces, with higher index faces disappearing due to their more rapid relative growth rate. For such a material growing into an undercooled melt, the undercooling along the faceted face will vary, becoming largest at the corner due to divergence of heat flux. This nonuniform interfacial undercooling results in an increased step density near the center of the face (where the undercooling is smallest) which encourages flatness by allowing the surface to advance everywhere with the same velocity. Consequently, one of the most significant aspects of lateral growth kinetics is that the faceting of the crystal acts as a stabilizing influence, discouraging breakdown of the plane front interface. At small undercoolings the conditions for stability of a growing faceted crystal can be expressed approximately by (37, 29):

$$Gr/D_L \lesssim -\Delta T/m_L C_o(1-k) \qquad (20)$$

where r is the radius of the crystal, m_L is the slope of the liquidus, C_o is the nominal composition and k is the equilibrium partition ratio. If the conditions of

equation (20) are not fulfilled the planar interface becomes unstable and the resulting cellular or dendritic structure will be highly faceted. In addition to the effect on interfacial stability, the departure from equilibrium associated with faceting can result in a significant change in the measured partition ratio (k) for this system. In studies on tellurium-doped indium-antimonide carried out by Hulme and Mullin (38) the presence of (111) facets was associated with anomalously high tellurium incorporation in the faceted region, with the concentration being approximately nine times that in the nonfaceted regions. Qualitatively similar results have been obtained in studies conducted on melt-grown oxide crystals (39). Thus, knowledge of the primary growth mechanism for a system, as may be surmised by consideration of material parameters and crystallographic orientation, can be used to both predict and interpret certain aspects of the solidification process such as the resulting solidification morphology and the segregation patterns associated with the product structure. Experimental verification of these predictions, however, is often complicated by additional effects such as the presence of minute impurities on step density, interface energy and anisotropy, which are difficult to model in a simple manner.

Solidification

a) Solidification of Pure Materials

1) Crystal Growth in Undercooled Melts

In the conventional casting of a pure material a positive temperature gradient typically exists in the liquid ahead of the advancing solid/liquid interface which acts to stabilize plane front crystal growth. However, if the liquid is undercooled below the equilibrium melting point a perturbation on the surface can be stabilized leading to breakdown of the plane front interface. The resulting dendrites which are formed by thermal undercooling alone are termed "thermal dendrites". Using white phosphorus to model the behavior of pure metallic systems, Glicksman and Schaefer (40) have measured the growth velocity of thermal dendrites as a function of bath undercooling. Phosphorus was particularly useful in this instance due to its favorable thermophysical properties which allow attainment of normalized undercoolings in excess of unity. Figure 12 shows a logarithmic plot of dendrite velocity versus the degree of normalized undercooling prior to the onset of solidification, where the dimensionless undercooling, ΔU may

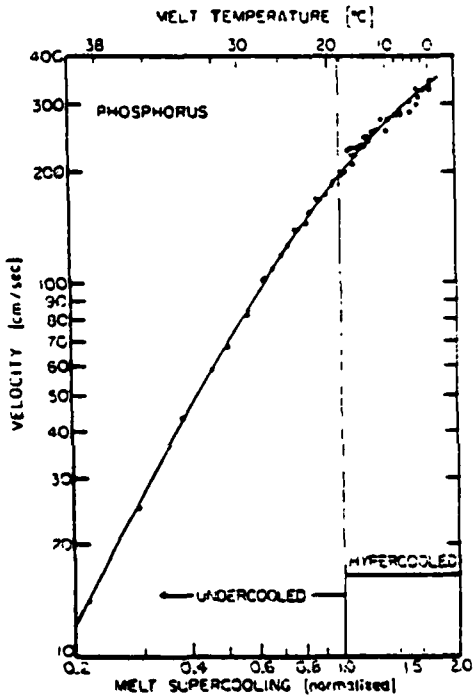

Figure 12. Illustration of dendrite velocity as a function of melt undercooling. (40)

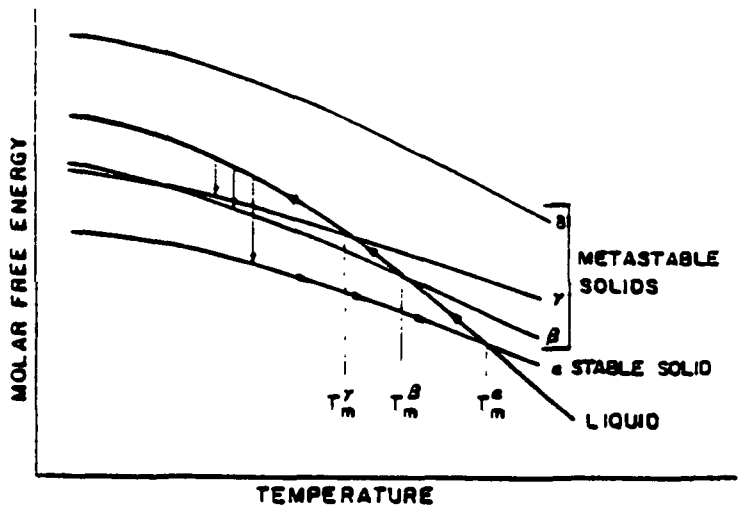

Figure 13. Illustration of the change in free energy with temperature for a liquid and various potential solid phases in a one component system. (4)

be defined as:

$$\Delta U = C_l \Delta T / L \qquad (21)$$

and C_l is the specific heat of the liquid. Once the level of undercooling exceeds unity, no further heat need be extracted from the system to obtain complete solidification. One of the most significant features of Figure 12 is that no discontinuity in slope, or other peculiarity, appears as the system enters the "hypercooled" region. For dimensionless undercoolings less than unity the experimental measurements of growth velocity are approximately of the form:

$$R = a\Delta T^n \qquad (22)$$

where R is the dendrite-tip velocity, a is a constant and n is on the order of 2. Typical experimental measurements have yielded values of n between 1.5 and 3 (29). For undercooled liquids (i.e. $\Delta U < 1$) the growth rate passes through a maximum and then decays rapidly as the release of latent heat raises the temperature of the melt (41). However, for hypercooled liquids ($\Delta U \geq 1$) the entire sample may solidify at a rapid growth rate.

While many theoretical attempts have been made to calculate dendrite growth velocities in undercooled melts, modeling such a process remains a complex matter. Most calculations have involved simplifying

assumptions such as neglecting depression of the equilibrium melting point of the dendrite tip due to interface curvature or the kinetic undercooling required to transport atoms across the solid/liquid interface. Further complications arise when the interactions of thermal fields of neighboring dendrites are considered or the steady-state growth assumption is not made. It is obvious that a detailed model must account for many of these parameters in order to obtain any significant degree of accuracy, however, it is interesting to note that excellent agreement between theory and experiment have been obtained by Huang and Glicksman (42) for dendrite velocities up to 1.5 cm/sec without including the effects of interface attachment kinetics. Their model predicts that the growth rate is controlled by diffusion of heat and curvature of the dendrite tip. This serves as an example of the progress that is being made in modeling the dendrite growth process in undercooled melts, the solutions of which are increasingly in line with observed experimental results.

2) Metastable Phase Formation in Pure Materials

As a liquid is progressively cooled below its equilibrium melting point it may become metastable not

only with respect to the equilibrium solid phase but also to solids which are thermodynamically disallowed under normal solidification conditions (i.e. $\Delta T \approx 0$). While thermodynamics alone cannot predict precisely which solid will form from the melt, it does allow for an assignment of the maximum potential for generating metastable products (4). Using a hypothetical single-component example, Figure 13 depicts the variation in Gibbs free energy with temperature for a liquid and various solid phases (4). As this is a single-component situation, the constant-pressure phase rule dictates that, in general, only one phase can exist over a range of temperatures and two phases can coexist only at a fixed temperature. Therefore each solid phase whose free energy curve intersects that of the liquid will have an equilibrium melting point associated with it at the temperature of intersection. Figure 13 illustrates this point for the α, β and γ phases. The fourth phase, δ, has no melting point for the range of conditions shown in Figure 13 and thus cannot form from the liquid.

Upon cooling from temperatures above T_m^{α}, if the nucleation of the α phase is suppressed the liquid will become undercooled and will continue to follow

the liquid free energy curve. Similarly, if the nucleation of β and γ is avoided the liquid will continue to exist, becoming metastable with respect to these phases as well. If either β or γ had nucleated at its melting point reversible solidification of that phase could have occurred. In this manner thermodynamic criteria may be used to predict which product phases are eligible for formation from the liquid. However, the solidification reaction path ultimately followed by the system will be contingent upon the nucleation kinetics involved. The nucleation rate of a phase depends upon many factors; the volume free energy of formation, the interfacial energy and the presence of heterogeneous nuclei, none of which needs to favor the stable phase. For example, by definition the stable phase in a single-component system has the largest driving force per mole for its formation. But, if its density is low, it need not have the largest driving force per unit volume, which is the important free energy quantity in nucleation theory (4).

While studies concerning metastable phase formation from undercooled liquids have primarily dealt with multicomponent systems, a number of enlightening observations have been reported for pure component systems. Among

these, one of the most extensive examinations has focused upon the crystallization of metastable phases from undercooled gallium (43, 44, 45). As revealed in the initial studies on bulk melts, continuous samples of gallium have a fairly large degree of undercooling potential (43). When the sample is subdivided using the droplet emulsion technique (46) this potential is greatly enhanced yielding terminal undercoolings in excess of one-half the melting temperature of the stable α phase. Figure 14 illustrates the crystallization behavior of such a gallium emulsion (3) as well as the complex melting behavior encountered upon heating the droplet sample. Five distinct endotherms are observed which can be matched with the various possible gallium crystal structures, some of which may be stabilized under high pressure. Furthermore, while a major crystallization exotherm terminates the undercooling of the liquid gallium, a significant portion of the droplet sample crystallized over a wide range of temperatures at lesser undercoolings, with the undercooling limit being dictated by the crystallization kinetics of metastable product phases (3).

The study of metastable phase formation in pure component systems is not limited to the observations

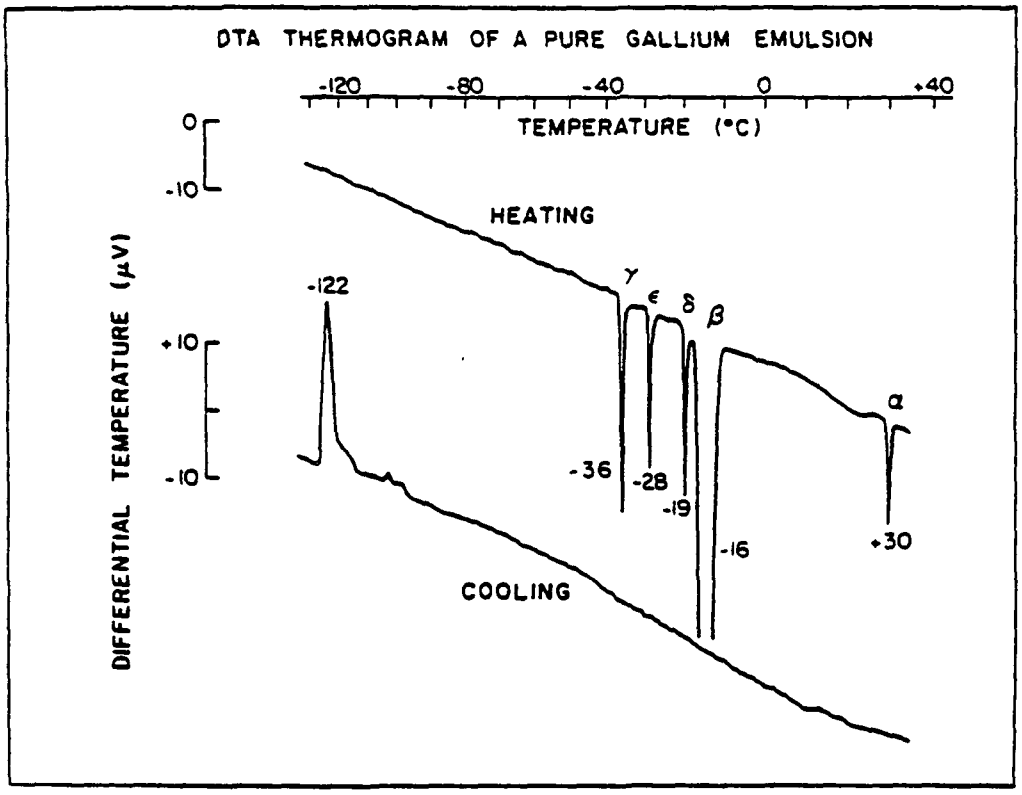

Figure 14. DTA thermogram showing the crystallization of pure gallium at maximum undercooling. Upon heating, the presence of both metastable and equilibrium phases is revealed through the appearance of melting endotherms.

on gallium. Studies have revealed that droplets of bismuth may crystallize into a metastable structure corresponding to the bismuth II phase (3), which is stabilized at high pressure. In addition to bismuth, several metastable structural modifications have been observed to form during the rapid solidification of pure antimony (47). Once again, many of these structures correspond to equilibrium high pressure antimony phases. Thus, at ambient pressures and high levels of undercooling, different structural modifications may have favorable nucleation kinetics so that they compete successfully with the equilibrium structure and crystallize directly from the liquid (3).

3) Studies on Pure Antimony

Antimony is a group IV metalloid which crystallizes in the rhombohedral structure under ambient pressures and normal casting conditions. In a manner similar to other elements of this group (i.e. P, As and Bi), antimony undergoes high pressure polymorphic transformations which were first examined using electrical resistance measurements (48, 49). Subsequent experiments involving high pressure x-ray (50) and thermal analysis treatments (51, 52, 53) yielded information concerning

both the crystal structure and stable regions of the high pressure polymorphs. Based upon precise measurements of the melting temperature (54, 55, 52, 51) two triple points have been observed in the temperature-pressure diagram for pure antimony. The first triple point occurs at 3.8 kbar, 627.8°C (52) and is associated with SbI (rhombohedral)-SbII (simple cubic)-liquid phase equilibrium. Despite early arguments to the contrary, the rhombohedral/simple cubic transformation has been shown to be of first order, with an associated volume change of 0.5% (56) for temperatures approaching the melting point. The second triple point occurs near 59 kbar, 564°C (53) representing equilibrium between SbII (simple cubic)-SbIII-liquid phases. The crystal structure of the high-pressure SbIII phase has variously been reported as hcp (50), distorted hcp (56), monoclinically distorted SnS-type structure (56) and tetragonal (57). While supporting x-ray evidence seems to favor either the monoclinic or tetragonal structure of SbIII, conclusive proof has not been established and thus the issue remains unresolved. Figure 15 shows the currently accepted temperature-pressure diagram for pure antimony. Attempts to discover the phase transformation at temperatures intermediate between the melting curve

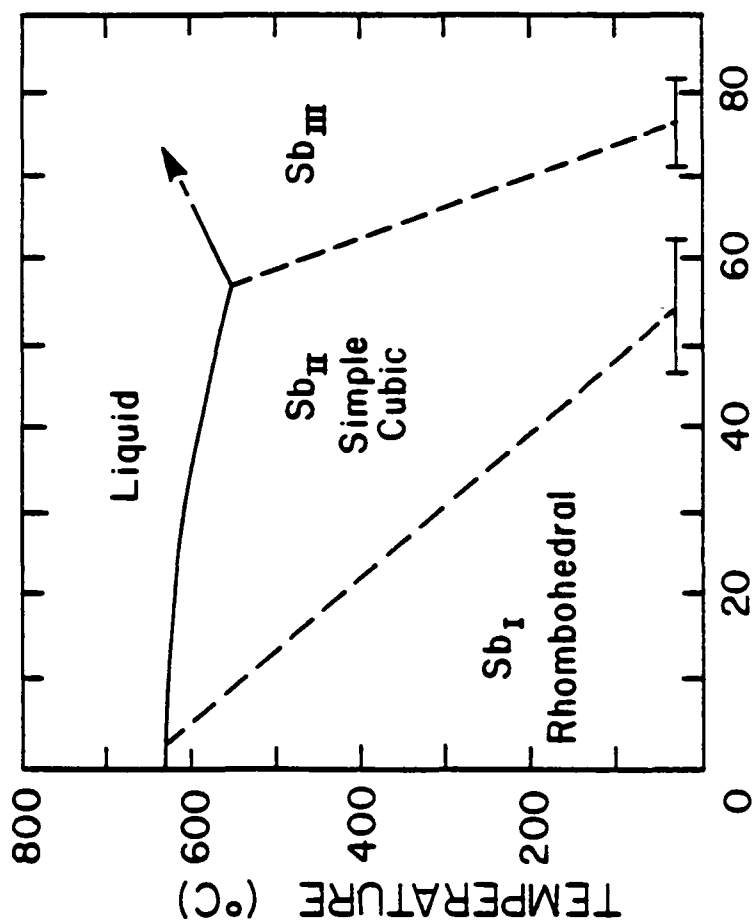

Figure 15. Temperature/pressure diagram for pure antimony. Dashed lines indicate extrapolated transition boundaries for intermediate temperature regions.

and room temperature have not produced conclusive results, therefore the equilibrium lines corresponding to these transformations are usually entered on the T-P diagram in dashed form.

Metastable phase formation in antimony has been examined through the use of splat-quenching from the liquid state and vapor deposition onto cooled substrates (47, 58, 59). Subsequent characterization of the product phases utilized both differential thermal analysis and electron diffraction techniques which yielded information primarily concerning the crystal structure and transformation kinetics of the resulting phases. A variety of structural modifications were detected in splat-quenched foils produced using the "gun" technique (47), a summary of which is presented in Table II (58). The variable in this case is the diaphragm rupture pressure, the magnitude of which influences the thickness of the foil and thus the resulting solidification rate. Foils obtained at the lowest rupture pressure (20 kg cm^{-2}) produced the equilibrium rhombohedral, hcp, fcc and simple cubic phases. The equilibrium phase appeared primarily in the thicker portions of the foil with the hcp phase dominating the thinner regions. Only in extremely thin regions did evidence

TABLE II

Rupture Pressure ($kg\ cm^{-2}$)	Structures Observed In Splat Quenched Foils
20	equil. rhomb., hcp, simple cubic, fcc
40	hcp, simple cubic, fcc, "new" rhomb.
60	simple cubic, fcc, "new" rhomb., tet.
80	simple cubic, fcc, "new" rhomb., tet.

of the fcc and simple cubic phases appear. Upon heating with an electron beam the fcc and simple cubic phases transformed to the hcp phase which resisted subsequent transformations. Foils obtained at greater rupture pressures (40 kg cm^{-2}) exhibited hcp, fcc, simple cubic and "new" rhombohedral phases. The hcp, fcc and simple cubic phases demonstrated transformation behavior similar to that previously discussed. However, the metastable rhombohedral phase transformed directly to the equilibrium structure upon electron beam heating. Foils produced by still greater rupture pressures (60 and 80 kg cm^{-2}) did not exhibit either the hcp or equilibrium phase, but instead formed an additional metastable tetragonal phase. Once again the fcc, simple cubic and tetragonal phases transformed directly to the equilibrium phase upon application of heat. The flow chart illustrated in Figure 16 summarizes the metastable phase formation and transformation tendencies as well as the associated temperatures and heats of transformation as determined by differential thermal analysis (58). It is thus concluded that the cooling rates required to obtain the various metastable phases increase in the order: hcp, fcc, simple cubic,

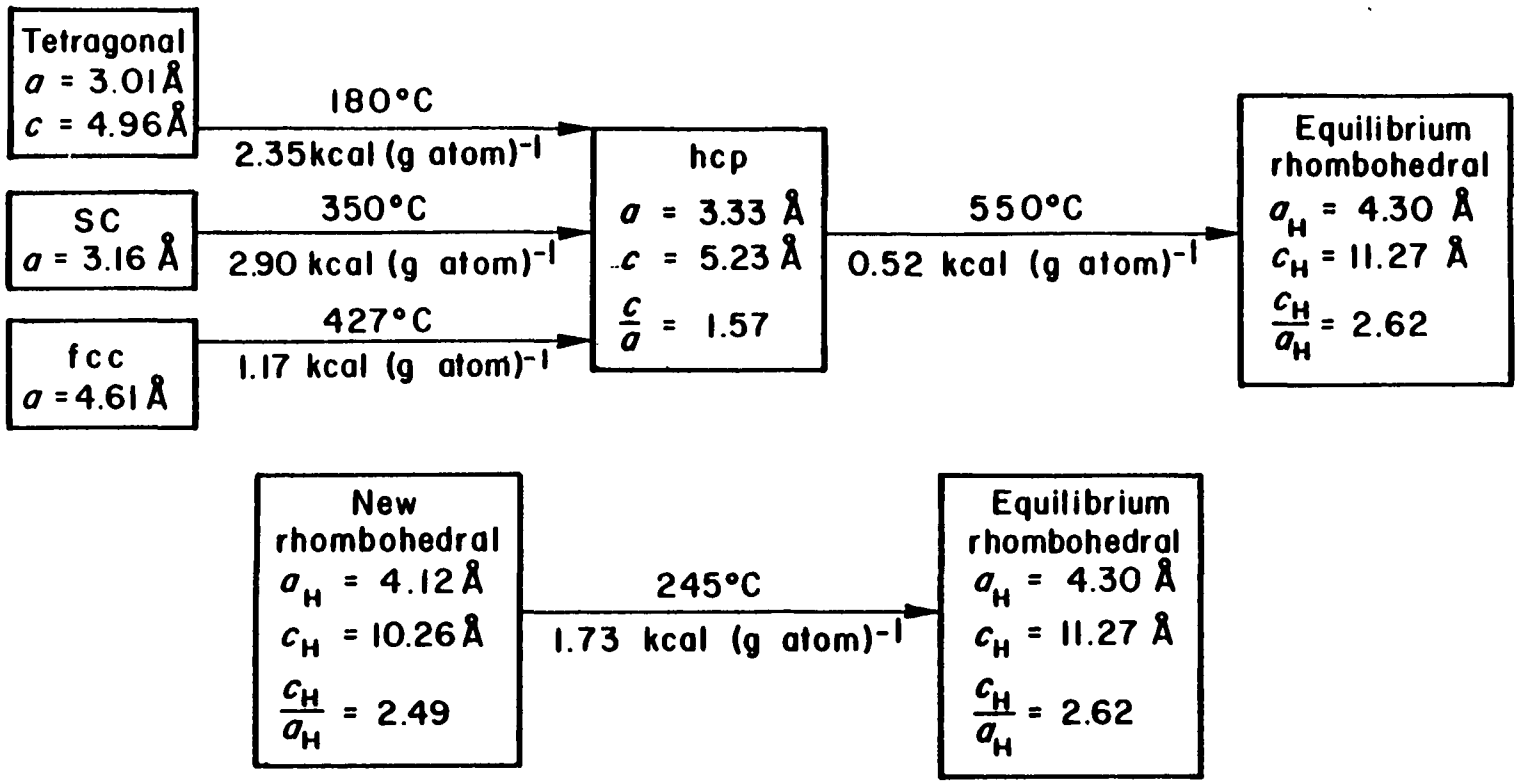

Figure 16. Summary of metastable phase transformation tendencies with with associated temperatures and heats of transformation for splat-quenched foils of pure Sb. (58)

"new" rhombohedral and tetragonal phase (58).

Examination of antimony films produced through vapor deposition yielded results similar to those of the liquid-quenched specimens. Films deposited onto substrates held at room temperature indicated the presence of both the metastable fcc and "new" rhombohedral phases as well as the equilibrium structure. On electron beam heating these phases transformed in a manner similar to that of the liquid-quenched foils. Deposition onto substrates held at liquid nitrogen temperatures yielded amorphous films which crystallized, upon heating, through a structurally complex phase before completing the transformation to the equilibrium rhombohedral phase (47). It is thus concluded that metastable crystalline phases observed in the liquid-and vapor-quenched samples may be directly related to equilibrium structures formed under high temperature/pressure conditions and, as such, may be used to predict possible polymorphic changes as yet undocumented (58).

b) Eutectic Alloys

1) Classification of Eutectics

The eutectic solidification process and resulting microstructures have been the focus of numerous studies

over the past 70 years. Throughout this period many attempts have been made to classify eutectic structures based upon a wide variety of criteria, the earliest of which was a simple microstructural evaluation. Using this method, Brady (60) and Portevin (61) distinguished three eutectic categories: lamellar, rod-like (or fibrous) and irregular. Generalizing this classification scheme somewhat, Scheil (62) proposed two basic eutectic categories based upon the underlying mode of crystallization rather than simply on morphological characteristics: "normal" microstructures, comprising mainly the lamellar or fibrous types, are formed from the simultaneous growth of the two solid phases in the form of parallel lamellae or parallel rods of one phase in a continuous matrix of the other; "abnormal" structures are formed when, for any reason, the two solid phases are prevented from growing at equal velocities. Furthermore, he suggested that a normal microstructure should be favored if the eutectic phases are present in nearly equal proportions while an abnormal structure should result if the volume fractions differ widely or if the minor phase exhibits marked growth anisotropy. While these criteria have subsequently proven overly simplistic, the classification categories have generally remained

in use. It should be noted that these two classifications (i.e. normal and abnormal) represent only the extremes in behavior and a virtually continuous series of intermediate cases can occur (63).

Following Scheil, a number of criteria have been suggested by which the eutectic solidification structure could be characterized. These include: lead distance (64): the tendency to form an abnormal microstructure increases as the lead distance of one phase over the other during growth increases; constitutional undercooling (65): the tendency to form an abnormal microstructure increases as the ratio (1-k)/k increases; reciprocal nucleation (66): the tendency to form an abnormal microstructure increases with increase in the parameter ψ:

$$\psi = \frac{\Phi_\alpha - \Phi_\beta}{\Phi_\alpha + \Phi_\beta} \quad \text{and} \quad \Phi = L/_V 2/3$$

where L is the latent heat of fusion and V is the atomic volume; activity coefficients (67): a normal microstructure is favored by positive deviations of the activities while an abnormal structure is favored by zero or negative deviations. Any of these methods may be used to provide readily accessible criteria for prediction of simple binary eutectic solidification

structures. However, each has been only partially successful in predicting any but the most extreme variations in microstructure.

An alternative approach to classification of eutectics is based upon a proposal by Hunt and Jackson (68) that eutectic structures are linked to the nature of the solid/liquid interface of each constituent phase. This proposal suggests that based upon the α-parameter (equation 12) of each constituent phase, three interface configurations are possible: (1) each phase may grow with an atomically rough interface ($\alpha \leq 2$); (2) one phase may grow with a faceted interface (atomically smooth, $\alpha > 2$) while the other grows with a rough interface; (3) both phases may exhibit facets during growth. These categories are described respectively as non-faceted/non-faceted (n.f./n.f.), faceted/non-faceted (f./n.f.), and faceted/faceted (f./f.). The eutectics consisting of n.f./n.f. combinations generally yield lamellar or rod-like morphologies while the f./n.f. and f./f. combinations produce either irregular or complex-regular morphologies. In extending this concept to systems involving intermediate compound phases the α-parameter is redefined as (67):

$$\alpha = \Delta S_\alpha \zeta / R \qquad (23)$$

where ΔS_α is the entropy of solution of the compound phase. Due to the occurrence of complex crystal structures in many of the compound phases it is often difficult to calculate α-values which have the physical significance of those calculated for close packed structures. Therefore, although the division is less well-defined, the occurrence of faceting may alternatively be predicted solely on the basis of ΔS_α. Empirically (69), the transition from non-faceted growth to a faceted morphology has been found to occur at ΔS_α = 5.5 cal/g·atom ^{o}K (23 J/mole ^{o}K). Based upon this concept, a more thorough classification scheme has been developed (70) which utilizes not only the ΔS_α term, but also the relevant volume fractions of constituent phases in order to predict the eutectic solidification structure. Figure 17 illustrates a correlation of eutectic structures with ΔS_α and volume fraction of constituent phases for a number of eutectic systems at a fixed growth rate of 5×10^{-4} cm/sec (70). From this diagram two broad fields of eutectic growth are distinguishable, those in which both phases have low ΔS_α-values ($<$5.5 cal/g·atom ^{o}K) and those in which one or both phases have larger ΔS_α-values. Further subdivision occurs through consideration of the relevant phasial volume fractions (V_F). At low volume fractions, rod

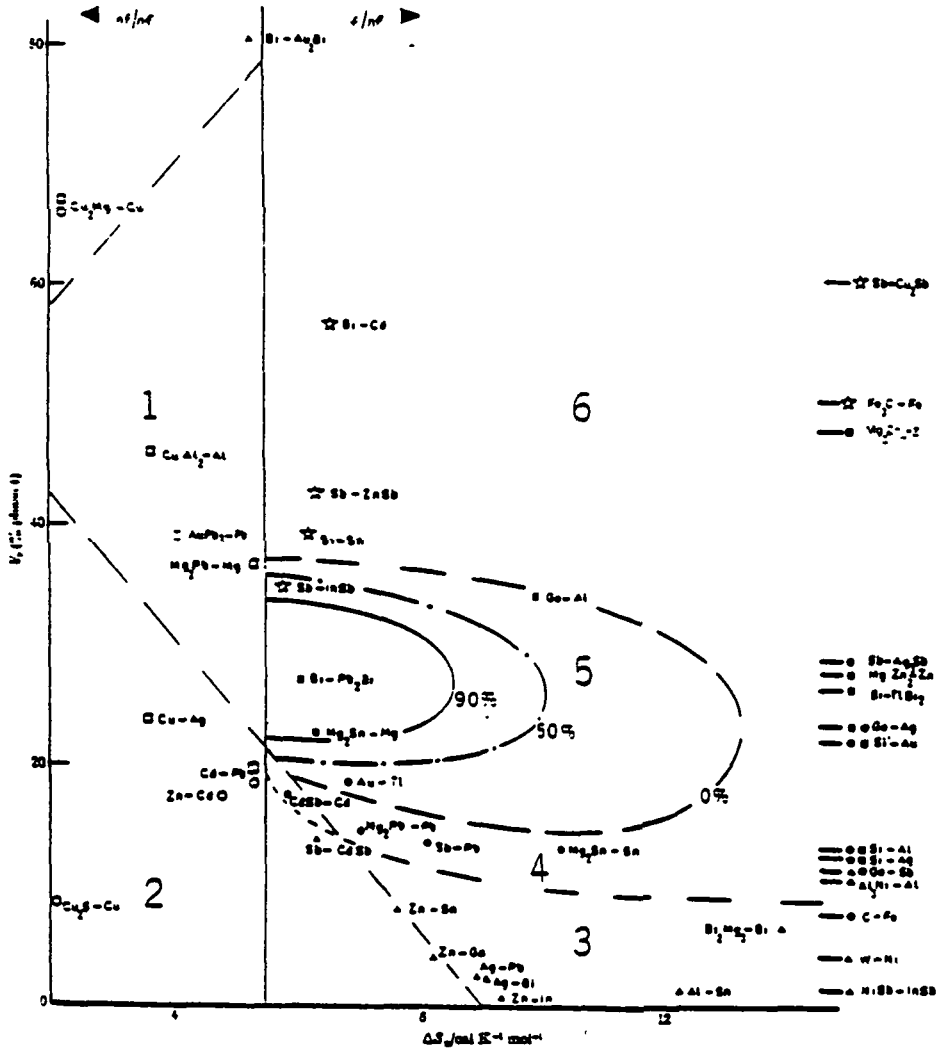

Figure 17. Correlation of eutectic structure with entropy of solution and phasical volume fraction for a number of eutectic alloys at a growth rate of 5×10^{-4} cm/sec. □ lamellar structure, ○ rod-type structure, ▲ broken-lamellar or fibrous structure, ● irregular structure, ■ complex-regular structure, ☆ quasi-regular structure. (70)

growth (region 2) is energetically favored over lamellar growth (region 1). However, since surface energy anisotropy increases as the tendency towards faceting increases, the boundary between regions 1 and 2 is displaced to smaller V_F as ΔS_α increases. Anomalous eutectics (i.e. $\Delta S_\alpha > 5.5$ cal/g·atom ^oK for one or both phases) exhibit more structural variety, but are primarily characterized by four types (regions 3-6). At low V_F (<10%, region 3) the dominant morphology is that of the broken-lamellar or fibrous type (depending on the applied growth conditions). Region 4 is characterized by a highly irregular morphology often referred to as a "chinese-script" structure. In region 5, as the V_F increases to values in excess of 20%, the irregular structures give way to "complex-regular" morphologies which are characterized by the presence of macrofaceted cellular projections at the growing solid/liquid interface (71). The final morphological variety observed in the anomalous groups of eutectics is represented by region 6 in which, as V_F increases still further, the high entropy phase tends to form the matrix of the eutectic. This group is characterized by structures similar to that of the n.f./n.f. eutectics and is thus termed "quasi-regular". The quasi-regular structures may consist of both fibrous and plate-like

morphologies and are very sensitive to changes in growth conditions. The increased regularity observed in these systems may arise from the reduced frequency of overgrowth resulting from the faceting phase now being the matrix (70). This inhibited overgrowth has been attributed to the microtopology of the solid/liquid interface which is such as to provide a continuous supply of growth steps for the matrix thus allowing unrestricted growth similar to that of a non-faceted phase (68).

In addition to phasial volume relations and entropy considerations, the growth velocity and liquid temperature gradient may also influence the eutectic solidification structure. Figure 18 illustrates the shift in observed structural boundaries as the growth rate (R) is altered (70). In general, all f./n.f. and f./f. eutectics show considerable variations in structure as R is increased. In contrast, n.f./n.f. eutectics show comparatively little growth-rate dependence. In considering the effect of increasing growth-rates, the following structural transitions may be observed (70):

1. degenerate regular → regular lamellar
2. degenerate rod → regular rod

] n.f./n.f.

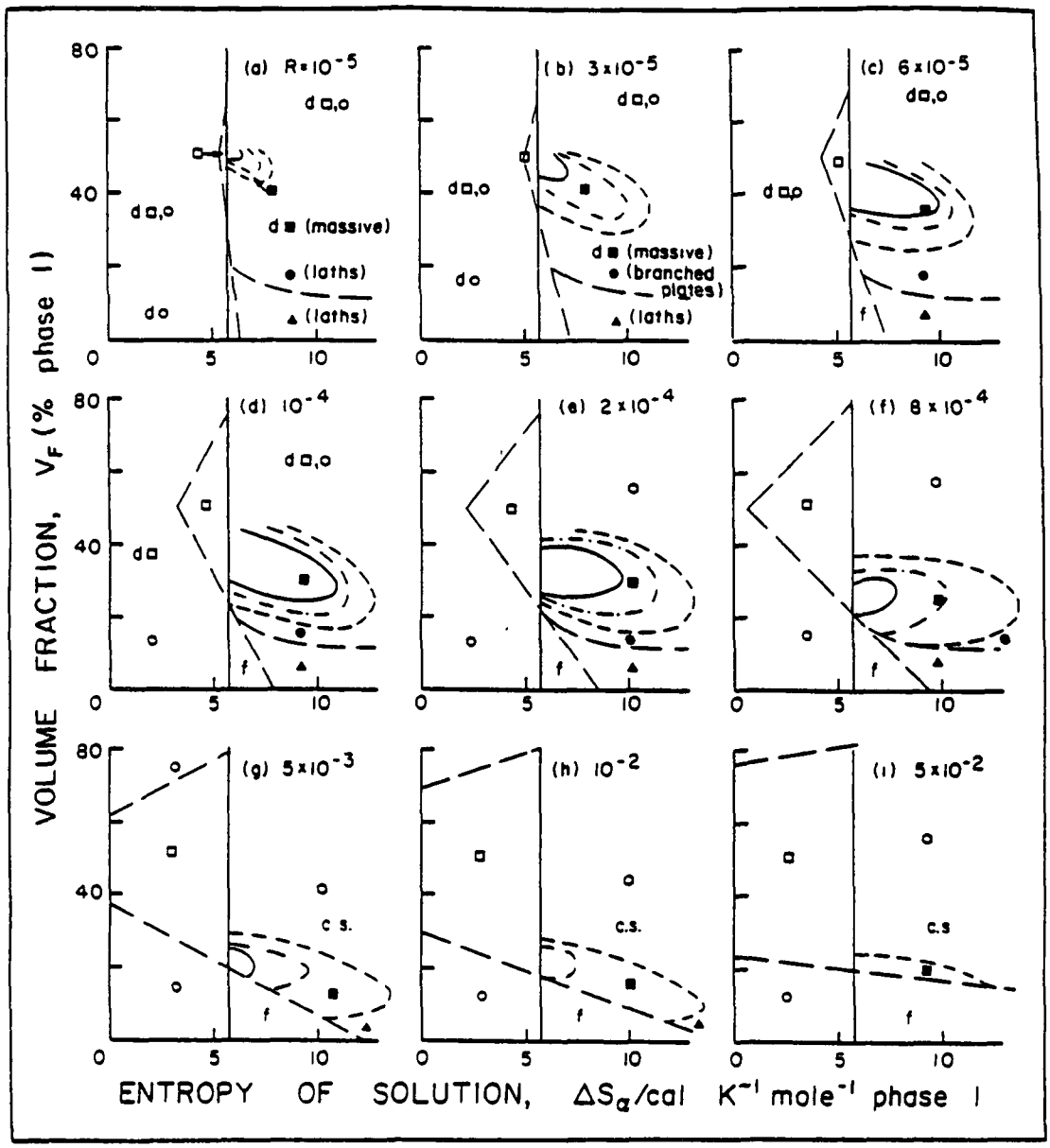

Figure 18. Effect of growth rate on observed microstructural boundaries (R: cm/sec). (70)

3. broken lamellar → fibrous
4. irregular (angular branched plates) → fibrous
5. irregular → complex regular → fibrous
6. degenerate complex regular → complex regular → chinese script
7. complex regular → quasi - regular
8. degenerate regular → quasi-regular

It is important to note, however, that these transitions only represent trends and that numerous exceptions have been found, particularly in f./n.f. systems. For example, item 3 is reversed in the W-Ni system (i.e. as R increases a fibrous → broken lamellar transition occurs) (72). An additional factor which under certain circumstances may directly influence the eutectic morphology is the presence of thermal anisotropy. In systems containing a rhombohedral constituent such as Sb (thermal conductivity is 150% greater in directions perpendicular to the trigonal axis than along the $[111]_{Sb}$ (73)) the high conductivity $(111)_{Sb}$ planes tend to align themselves with the crystal axis as the growth rate is increased. The resulting transition from a stable rod structure to that of a plate-like morphology appears to stem from this alignment of $(111)_{Sb}$ planes in the direction of heat withdrawl (73). Thus in addition to the properties

of the constituent phases themselves, the conditions under which the eutectic alloy is solidified can play a significant role in determining the resulting microstructure and therefore in general must be considered prior to classification of a particular eutectic system.

2) The Coupled Zone

The "coupled region" of a eutectic phase diagram has been defined as the composition and temperature range over which the solid phases can grow from the melt at equal velocities with a common interface to form a normal-type microstructure (63). Using model organic systems, Kofler (74) experimentally determined the boundaries of the region for a number of systems by varying composition and undercooling (below the eutectic temperature) and observing the points at which the velocity of either primary phase exceeded that of the eutectic. In this manner two principle types of coupled zones, illustrated in Figure 19, were defined (74). A type I coupled region does not include the eutectic composition at any except the eutectic temperature. As some degree of undercooling below this temperature typically occurs prior to nucleation, the presence of a type I coupled zone prevents

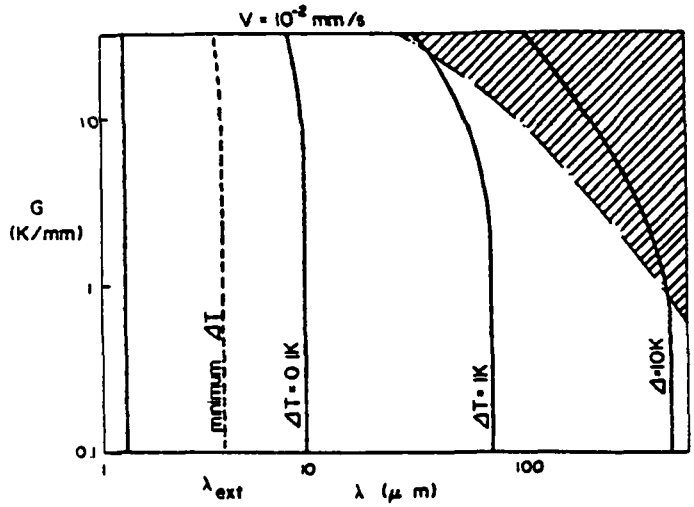

Figure 20. Relationship between interfacial undercooling, eutectic spacing and temperature gradient at a fixed growth velocity (10^{-2} mm/sec) for a faceted eutectic alloy. (81)

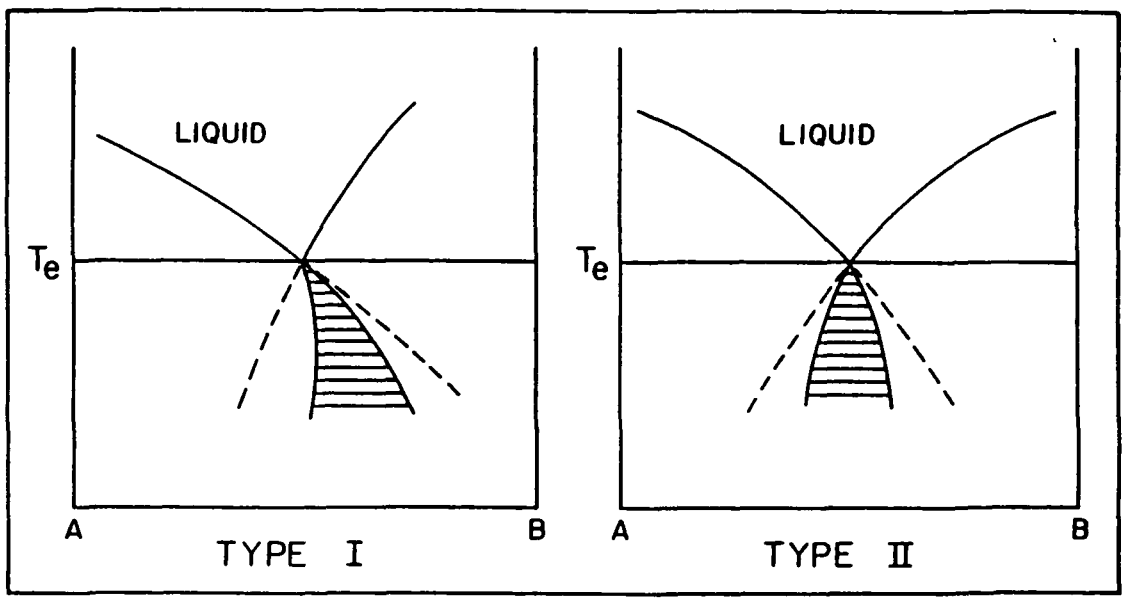

Figure 19. Illustration of cooperative growth regions for both skewed (type I) and symmetric (type II) coupled zones.

a normal structure from forming when the melt is of eutectic composition. The nucleation sequence is also important in determining the morphology of a type I eutectic. If phase A nucleates readily, primary crystals of A will form from the undercooled melt enriching the remaining liquid in B until it enters the coupled region where a normal structure may form. On the other hand, if A requires large undercooling, B may nucleate first, forcing the liquid composition away from the coupled zone until sufficient undercooling is obtained to nucleate A. Phase A then surrounds B returning the liquid toward the coupled zone. The subsequent solidification sequence depends upon the relative growth velocities and nucleation capacities of the two phases. A type II coupled zone includes the eutectic composition at all temperatures and thus, in this instance, undercooling of the liquid will not preclude coupled growth, providing both phases have successfully nucleated.

Prediction of the extent of coupled growth involves consideration of both imposed growth conditions and constituent phase properties. In the case of simple metallic eutectics (or others with low ΔS_f) the coupled region tends to be of type II and is symmetric about the eutectic composition. However, if a constituent phase

has a large ΔS_f (i.e. is faceted) the coupled region tends to be skewed in the direction of that phase and is of type I (63). This is often the case in systems containing a semi-metal or intermetallic compound phase. In the case where both constituents have a high entropy factor the strict definition of a coupled region becomes blurred. The two phases tend to grow simultaneously with similar velocities, but the macroscopic solid/liquid interface is somewhat rougher than for a n.f./n.f. system and the precise degree of cooperation between the phases is much more difficult to determine (68).

3) Lamellar-Fibrous Transition

Normal-type eutectic structures consist of alternating plates of the constituent phases or rods of one phase in a continuous matrix of the second, or, in certain cases, combinations of both morphologies. Most eutectic alloys show a strong preference for one growth form over the other. Following the analysis of Hunt and Chilton (75) this preferred morphology may be explained in terms of interfacial energy considerations. The morphology which minimizes the total interfacial energy will be the favored growth form. Based upon geometric relationships, lamellae will be favored

when (75):

$$V_A > 1/A^2\pi \qquad (22)$$

where V_A is the volume fraction of the minor phase and $A = \sigma_R/\sigma_L$ (i.e. the ratio of the interfacial energy of rods to that of lamellae). Thus the critical volume fraction above which lamellae will be energetically favored varies greatly with the ratio of interfacial energies. If the surface energies are isotropic (A = 1) a rod structure should be stable for $V_A < 32\%$. However, adoption of low energy, crystallographic habit planes can alter the energy ratio dramatically thus influencing the solidification morphology. For example, the Al-Co_2Al_9 eutectic typically forms a lamellar-type structure even though the Co_2Al_9 phase occupies less than 3% of the volume. This growth pattern has been attributed to the availability of a (100)/(100) plane matching which lowers the interfacial energy for this orientation relationship (63). Alternatively, the presence of two or more low energy planes can stabilize the growth of faceted rods even when the volume fraction exceeds 32%. Examples of faceted rod morphologies include systems such as Nb-Nb_2C, Ta-Ta_2C, Sb-MnSb and Sb-InSb (63). While attainment of low energy orientation relationships can influence solidification morphologies,

often the imposed growth conditions prevent these low-energy arrangements from occurring. For example if the advancing solid/liquid interface is slightly curved, lamellae lying off the cell axis will be forced out of their preferred growth direction (in order to remain perpendicular to the interface) thus increasing the lamellae solid/solid interfacial energy relative to that of the rod energy and thereby encouraging a transition from lamellae to rod growth morphology (63). Another cause of an orientation relationship change can lie in the thermal anisotropy of a constituent phase. If the preferred growth orientation does not coincide with the direction of highest thermal conductivity, the imposition of heat flow restrictions can encourage rotation of the growing solid and alignment of the high conductivity planes (73). This in turn alters the orientation relationship which influences the resulting solidification morphology (73). The importance of this conductivity effect has been particularly emphasized in eutectic alloys containing a rhombohedral phase such as Bi or Sb due to their pronounced thermal anisotropy.

4) Interphase Spacing vs. Solidification Rate

In the growth of a normal-type eutectic structure,

the interphase (i.e. rod or lamellar) spacing, λ, is determined by the interaction between the tendency to minimize λ in order to reduce the diffusion distance at the advancing solid/liquid interface and the opposing tendency to increase λ in order to minimize the solid/solid interfacial area and corresponding energy per unit volume (63). In a comprehensive treatment of this balance Jackson and Hunt (76) considered the solid/liquid interface to be undercooled by an amount, ΔT, given by:

$$\Delta T = \Delta T_D + \Delta T_C + \Delta T_K \qquad (23)$$

where ΔT_D is the undercooling necessary to provide a diffusion gradient between the phases, ΔT_C is the undercooling due to curvature of the interface and ΔT_K is the "kinetic" undercooling or the undercooling necessary to transport atoms across the interface. For n.f./n.f. systems ΔT_K is considered negligibly small however this assumption cannot in general be extended to f./n.f. or f./f. systems. Following the analysis of Jackson and Hunt (76) the solid/liquid interface of a n.f./n.f. eutectic is considered isothermal and is maintained so by a balance between ΔT_D and ΔT_C. Based upon this approach, the undercooling may be related to the eutectic spacing and growth velocity, V, by (77):

$$\Delta T = K_1 \lambda V + K_2/\lambda \qquad (24)$$

where K_1 and K_2 are constants given by:

$$K_1 = m_\alpha m_\beta C_o P(1 + \xi)^2/(m_\alpha + m_\beta)\xi D\pi^3 \qquad (25)$$

$$K_2 = \frac{2(1 + \xi)}{(m_\alpha + m_\beta)} \left[m_\beta \Gamma_\alpha \sin\theta_\alpha + m_\alpha \Gamma_\beta \sin\theta_\beta/\xi \right] \qquad (26)$$

where m_α and m_β are the (positive) liquidus slopes of the α and β phases, C_o is the eutectic composition, D is the diffusion coefficient, P is a tabulated function of the relative interphase spacing, ξ is the ratio of the half-width of the β-phase to that of the α-phase (S_β/S_α), Γ is the Gibbs-Thompson coefficient and θ is the junction angle of the phase boundary. If growth is assumed to occur at the spacing which minimizes the undercooling (i.e. the "extremum") the parameters λ, V and ΔT are related by:

$$\lambda^2 V = K_2/K_1 \qquad (27)$$

$$\Delta T/\sqrt{V} = 2\sqrt{K_1 K_2} \qquad (28)$$

$$\Delta T \lambda = 2K_2 \qquad (29)$$

Experimentally these relationships have been confirmed for numerous alloy systems through the use of directional solidification techniques (78). More recent studies involving the rapid solidification of Ag-Cu eutectics imply that the expressions are valid for growth rates in excess of 2 cm/sec at which spacings of approximately

200 Å have been measured (79). A theoretical limit to the extent of coupled growth however has been proposed to occur at a maximum velocity of approximately 4.9 cm/sec with a corresponding spacing of 78 Å (79). This may roughly be considered as an upper bound beyond which extrapolated values of the equations are physically meaningless.

Extending the analysis to f./n.f. or f./f. eutectics is a much more formidable task in that the resulting model must account for: (1) large variations in interphase spacings across an interface growing at constant velocity (80); (2) larger mean spacings than that found in n.f./n.f. eutectics for similar growth conditions; (3) larger corresponding interfacial undercoolings; (4) a dependence of both spacing and undercooling on the imposed temperature gradient at the interface. In attempting to account for these factors a model has been developed by Fisher and Kurz (81) which abandons the previous assumption of growth at the extremum and instead adopts morphological instability and branching limited spacing adjustment criteria. As a basic premise, the model assumes that the crystallographic anisotropy of the faceted phase prevents easy branching as the growth conditions are altered.

Thus the spacing must increase to a certain maximum value before morphological instability, and therefore branching, can occur to decrease the spacing. The observed spacings at any point in the system may lie between this maximum value and the value which gives the minimum undercooling (spacings smaller than this are inherently unstable (76)). This sets limits on the scatter in experimentally observed spacings along the interface. The functional relationship between λ, V and ΔT obtained with this model is identical in form to equation (24), with the constants K_1 and K_2 being given by (81):

$$K_1 = m_\alpha m_\beta C_o (1+\xi)/(m_\alpha+m_\beta) D\pi^3 (P+\Pi/f\xi) \qquad (27)$$

$$K_2 = \frac{2(1+\xi)}{(m_\alpha+m_\beta)} \left\{ m_\beta \Gamma_\alpha \sin\theta_\alpha + \frac{m_\alpha \Gamma_\beta \left[\sin\theta_\beta - \sin(\arctan g)\right]}{f\xi} \right\} \qquad (28)$$

where Π is a tabulated function of P and ξ and f is a function of the mean phase spacing. In order to determine the paired parameter relationships it is necessary to utilize the coupling condition which relates the temperatures of different parts of the interface via the imposed temperature gradient, G. In this way ΔT and λ are related (at any fixed growth velocity) as a function of G with the resulting curves being illustrated in Figure 20 (81). Thus, the relationship between each

pair of parameters (λ, ΔT and V) takes a functional form identical to that of equations (27), (28) and (29) with the only difference being the presence of a temperature gradient term in the "constants". Experimentally the proposed parameter relationships have been confirmed, with the Fisher-Kurz model providing a reasonable match to the data (81). While the present model derivation employs numerous assumptions, it provides a method of analyzing eutectic growth in faceted systems for which the Jackson and Hunt model is inappropriate. The rough agreement with experimental data as well as the "reasonable" explanations of observed phenomena act to justify the application to this category of eutectic alloys.

5) The Antimony-Indium System

The Antimony-Indium binary system is dominated by a line compound, InSb, and two eutectic reactions, as illustrated in the phase diagram of Figure 21 (82). The InSb-Sb eutectic reaction is of particular interest in that the entropy of solution for both phases is relatively large (ΔS_{Sb} = 5.79 $\pm$ 0.28 cal/mole ^{o}K, ΔS_{InSb} = 5.60 $\pm$ 0.12 cal/mole ^{o}K (70)) thereby placing it in the f./f. eutectic category. As is characteristic of many eutectics in this class, the solidification

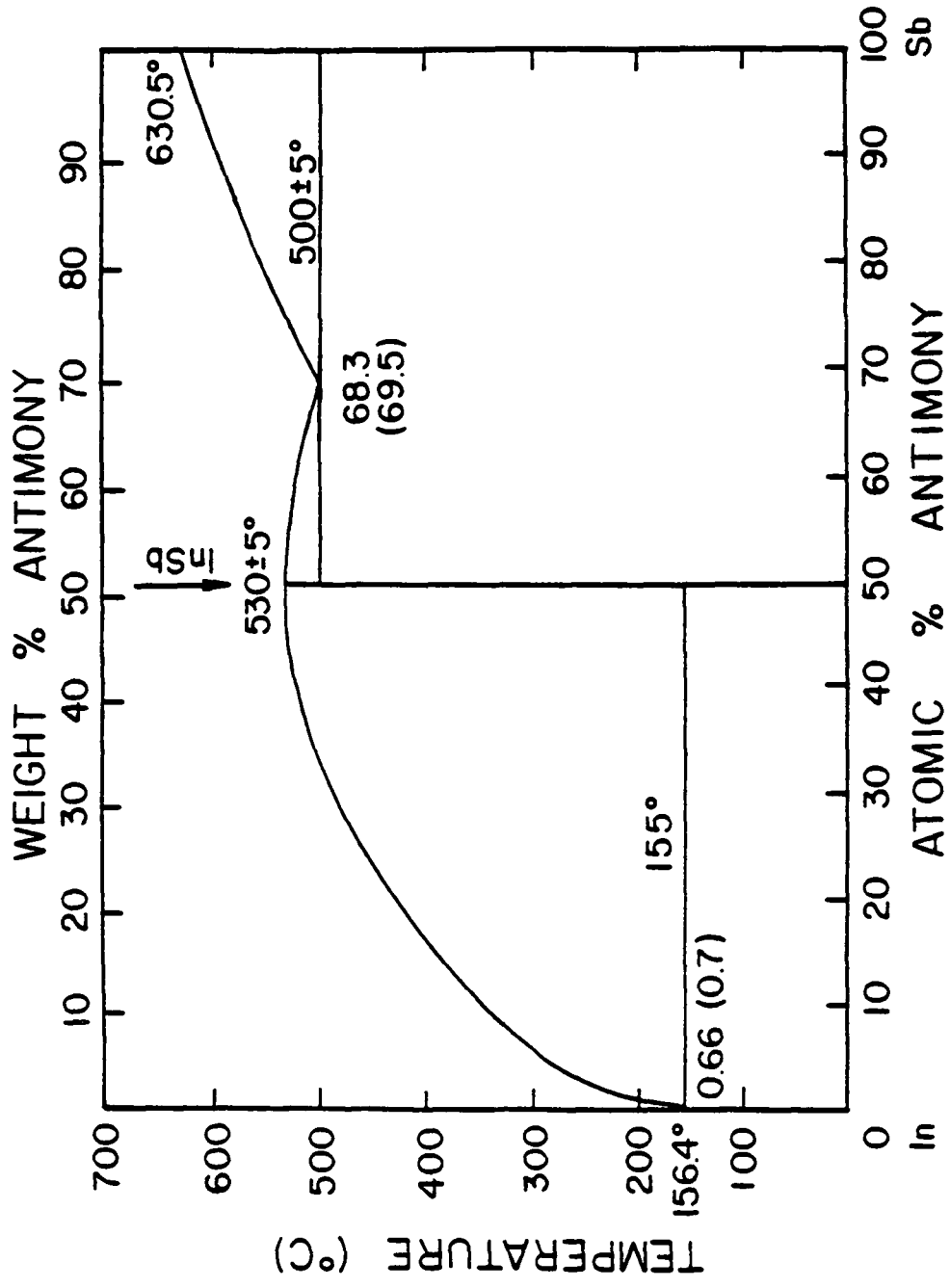

Figure 21. Phase diagram for the In-Sb system. (82)

morphology is highly sensitive to applied growth conditions. At moderate growth rates (1×10^{-5} - 7×10^{-4} cm/sec) a normal-type structure forms and is comprised of triangular rods of Sb in a matrix of InSb. This rod-type structure, while not immediately implied by volume fraction considerations ($V_{F(Sb)}$ = 35% (83)), may be attributed to a highly stable low-energy orientation relationship between the two phases. Antimony crystallizes in a rhombohedral structure with a lattice constant of 4.50 Å while InSb forms an fcc, ZnS (zinc-blende) type structure with the {111} plane's atoms arranged in a rhombohedral network and the corresponding interatomic distance being 4.56 Å. Therefore, a low energy interface between these phases may be formed by a series of interfacial steps, where the surface of each step has a {111} and {100} orientation for the InSb and Sb respectively. Liebmann and Miller (83) have confirmed the existence of this low-energy orientation relationship through detailed x-ray analysis techniques. Due to the normality of this structure, it has been possible to obtain meaningful data relating eutectic spacing (or equivalently rod size) to growth velocity, the results of which are illustrated in Figure 22 (83). As is predicted from theory (81) a linear relationship is

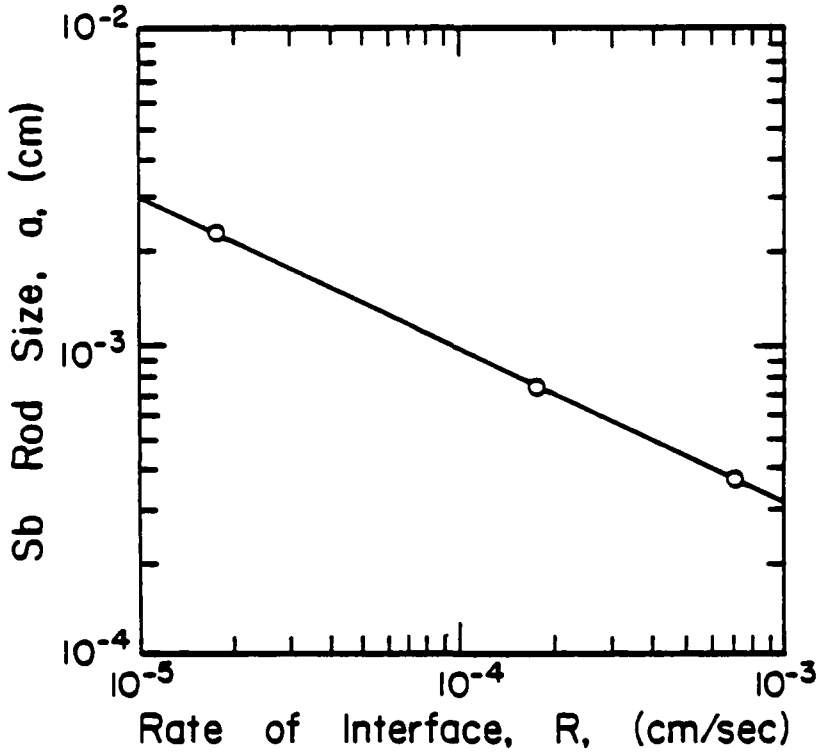

Figure 22. Relationship between rod size and growth velocity for the InSb-Sb eutectic system. (83)

obtained between spacing and growth rate under a constant applied temperature gradient, which in turn, has allowed experimental determination of the solid/solid phase boundary energy. Results of this calculation indicate that σ = 890 ergs/cm^2 (83).

In order to form the low-energy orientation relationship between the Sb and InSb phases it is necessary for the Sb rods to grow in their preferred $[111]_{Sb}$ growth direction. However, since Sb has highly anisotropic thermal properties, increasing the growth rate can force a deviation from the $[111]_{Sb}$ direction in order to allow alignment of the higher conductivity $(111)_{Sb}$ planes to occur. This results in an increase in phase boundary energy as the low-energy orientation is destroyed and thus (according to the criteria of equation (22)) encourages a transition from a rod to a lamellar morphology (73). This has been confirmed through directional solidification studies with varying growth rates in which the transition from a rod to lamellar morphology was found to occur at growth rates in excess of 4×10^{-4} cm/sec.

Both of the eutectic constituents, Sb and InSb, are known to undergo high-pressure polymorphic transformations. As such, certain studies have focused on

the attainment of metastable phase formation in this alloy system through the use of splat-quenching techniques (84, 85). Examination of various compositions have indicated the presence of a metastable simple cubic (Sb) phase in alloy compositions between 60 and 90 weight percent Sb, with the highest percentage (~100% metastable) being produced near the eutectic composition. In addition to metastable phase production, a small shift in the lattice parameter of Sb indicated that some solid solution of In in Sb may have occurred upon quenching (85).

SELECTION OF EXPERIMENTS

Studies involving the solidification of eutectic alloys have often focused on metal-metal systems where each component has a relatively low entropy of fusion and the resulting microstructure is comprised of a normal-type (i.e. rod or lamellar) eutectic morphology. Theories concerning this type of solidification reaction have been developed which may be used to relate interphase spacing to solidification rate and level of undercooling at the solid/liquid interface. The assumptions involved with these traditional theories, however, limit their application to simple non-faceted/non-faceted eutectic systems.

Eutectic alloys in which one or both of the constituent phases have a large entropy of fusion are often of practical interest in industrial applications. While the presence of a single phase exhibiting faceted growth tends to shift the coupled-growth region to compositions rich in that phase, if both constituents favor faceted growth the coupled region may be more symmetric about the eutectic composition. This, in turn, may lead to the formation of normal-type eutectic morphologies in a number of faceted/faceted alloy systems. While

numerous studies have confirmed the presence of these microstructures, the precise solidification structure which forms is apparently more sensitive to the imposed solidification conditions than in non-faceted/non-faceted alloys. The normality of the structure in these f./f. alloys has allowed measurements to be made of eutectic spacing as a function of solidification rate, the results of which are similar to those involving n.f./n.f. alloys. Accompanying these measurements, theories have been developed which describe the functional relationships between phase spacing, interfacial undercooling and solidification rate as well as the branching mechanisms.

In order to examine the solidification behavior of a faceted/faceted eutectic alloy in more detail, a system has been chosen in which some initial data exist relating interphase spacing to solidification rate. In addition, the melting points of the constituent phases (preferably both) as well as the eutectic temperature should lie in the working range of the emulsification process (i.e. $<1000^{o}C$). The alloy selected for study is the In-Sb system with the eutectic constituents being InSb and Sb.

Through the use of the emulsification process the most potent nuclei are isolated into a small fraction

of the droplet population. This may result in a variety of undercooling levels being attained as a function of droplet size. Using differential thermal analysis the level of undercooling in the liquid prior to solidification may be monitored and subsequent microstructural evaluation carried out in order to correlate the resulting eutectic structure with the level of undercooling. In addition to the equilibrium eutectic phases, splat cooling techniques have been used to form metastable phases in the InSb-Sb eutectic alloy as well as in both pure constituents. In order to detect the presence of metastable phases in this study, x-ray diffraction techniques have been utilized prior to microstructural evaluation of the processed powder.

EXPERIMENTAL PROCEDURE

Alloy Preparation

Materials chosen for use in this investigation were selected primarily on the basis of purity. As the earliest portion of the study considered the undercooling behavior of the pure constituent phases of the eutectic, namely antimony (Sb) and indium antimonide (InSb), one point of interest was the effect of initial material purity on subsequent undercooling behavior. Thus, for this portion of the study, the materials used were 99.8% and 99.999% Sb. In considering the InSb constituent, semiconductor grade material was selected with a nominal purity level of 99.999%.

Preparation of the eutectic alloy was carried out using 99.999% Sb and 99.9999% In parent ingots. Due to a slight ambiguity in the precise eutectic composition of the alloy, three 5-gram trial ingots were prepared (as to suggested eutectic compositions (82)) as Sb-29.5, 30.0 and 30.5 Wt.% In. Metallographic examination of the cross-sections revealed the presence of primary Sb dendrites in all samples except the 30.5 Wt.% In ingot. Therefore this composition was selected to represent the eutectic alloy and a 10-gram ingot was

cast for further use in the investigation. The ingot production technique involved encapsulating the binary components in a quartz tube evacuated to less than 50μ. The components were then heated to 250°C and held for approximately 15 minuted to allow the strongly exothermic formation of InSb (solid) to occur at a temperature low enough to eliminate the risk of a rapid increase in the vapor pressure of the pure antimony. The InSb and Sb components were then heated to 700°C and held for approximately 4 hours with periodic agitation applied to ensure complete homogenization of the liquid. The capsule was then quenched in an ice-water bath in order to minimize the size scale of segregation during solidification. The weight of the resulting alloy deviated by less than 0.1% from the combined weights of the starting components and subsequent metallographic examination of a cross-sectional wedge removed from the ingot revealed no primary phase formation. Thus the ingot was deemed acceptable for use in the investigation.

Droplet Production

Production of droplets for both the pure components, Sb and InSb, and the eutectic alloy was achieved through the use of an emulsion technique derived from earlier

work on aluminum and aluminum alloys (86, 87). With this method droplets are produced by shearing a small volume of liquid metal in a suitable carrier medium such that a surface reaction occurs which coats the droplets and allows them to remain independent of one another. Figure 23 presents a schematic of the emulsification apparatus. A slotted alumina shearing rod is attached to a high speed motor capable of achieving 30,000 rpm. The metal/carrier fluid mixture is held in an alumina crucible containing an agitator ring which disrupts the fluid during stirring to enhance the shearing action. The time for emulsification may be varied according to the relative shearing and reaction rates within the carrier fluid.

Of primary importance in the use of this technique is the selection of an appropriate carrier medium for the material. The reaction which occurs must be such that only the surface of the molten droplet is involved and the coating produced must be stable enough to prevent subsequent coalescence of the droplets. Of secondary consideration is the solubility of the carrier medium. Following the emulsification of the alloy the surrounding media must be removed in order to classify the droplets according to size. Therefore, it is necessary

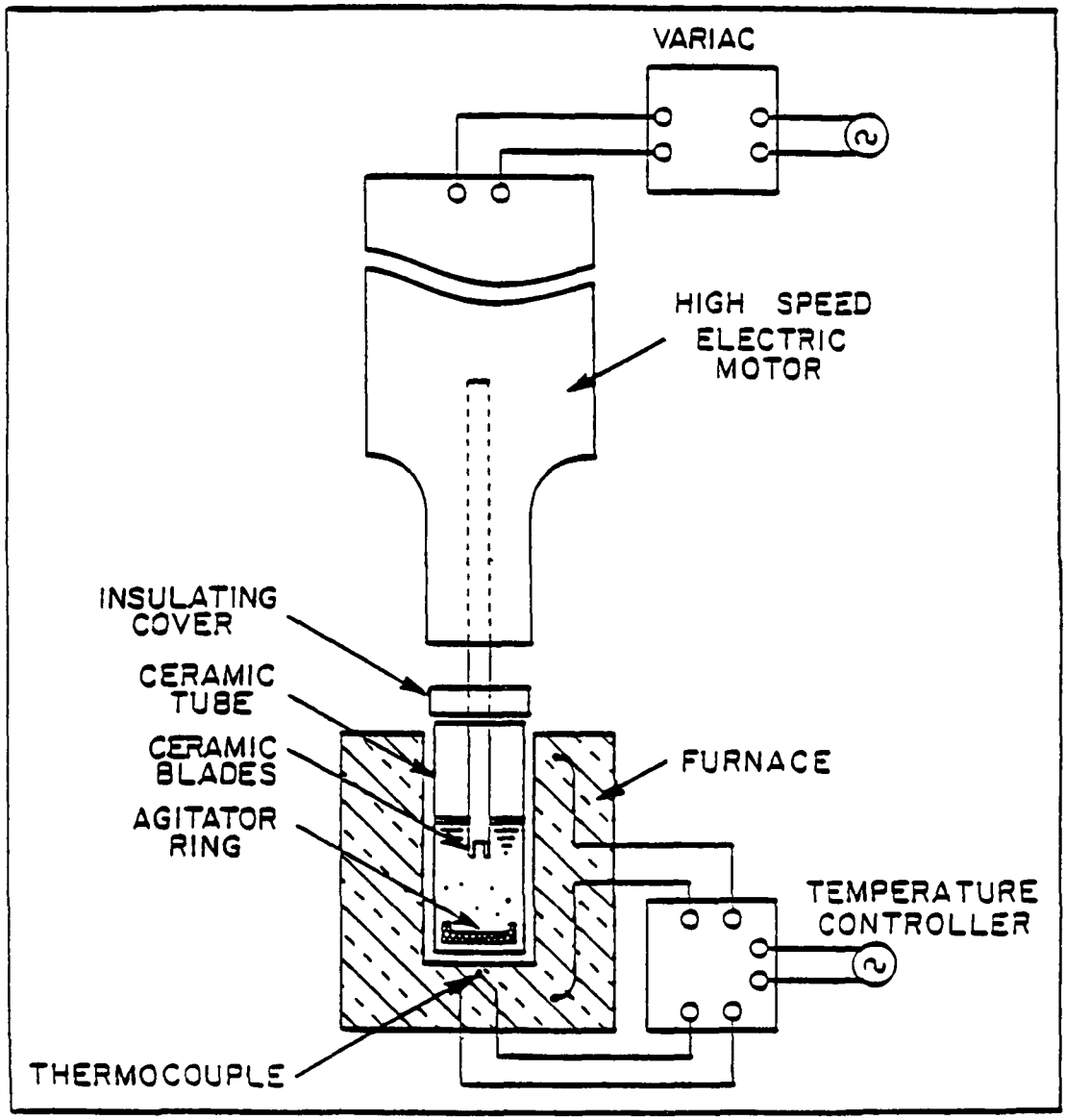

Figure 23. Schematic illustration of the droplet emulsification apparatus.

to use a carrier fluid that is soluble to some degree in a relatively benign solvent (i.e. one which will not attack the entrained droplets). The carrier medium chosen for the emulsification of pure antimony was a K_2SO_4-$ZnSO_4$ salt of eutectic composition (T_e = 458°C). While this salt met all criteria for successful emulsification, upon dissolution in distilled water an insoluble precipitate tended to form and remained with the Sb powder throughout subsequent processing. Emulsification of both InSb and the In-Sb eutectic alloy was conducted using a K_2SO_4-Li_2SO_4 eutectic salt (T_e = 547°C) whose high solubility in water avoided the formation of precipitates during dissolution. All emulsions were prepared using a ratio of 2 grams of metal to 20 grams of salt with the most favorable temperature/time combinations determined as:

Sb: T = 700°C, t = 3 minutes
InSb: T = 650°C, t = 3 minutes
Sb-InSb: T = 650°C, t = 3 minutes

Following emulsification the droplet/salt mixture is poured onto a polished aluminum chill plate and air cooled. Removal of the salt is carried out in a Nalgene 0.20 micron filter unit through which distilled water is flushed over the salt/metal mixture until no visible

salt residue remains. The metal droplets are then rinsed from the filter with methanol, collected and allowed to dry.

Droplet Size Classification

The droplet emulsion technique used in this investigation typically produces a distribution of droplet sizes ranging from a few microns to over 150 microns. Control over the range of droplet sizes to be examined is obtained through classification of the powder according to size following removal of the carrier media. Classification is achieved using an ATM Sonic Sifter which utilizes an oscillating air column to agitate the metal powders over a series of sieves. This agitation prevents entrapment of the powder in the sieves and improves the separation and classification process. The sieves are made of electroformed nickel and are capable of separating powders as fine as 5 microns. Precision nickel mesh sieves of 8, 18, 28, 37 and 44 microns were used in conjunction with standard Tyler mesh sieves of 63, 88 and 150 microns. Using this approach size ranges of -8, 8-18, 18-28, 28-37, 37-44, 44-63, 63-88 and 88-150μm were available for examination during the course of this investigation.

Differential Thermal Analysis

Differential thermal analysis (DTA) is a technique used for studying the thermal behavior of materials as they are subjected to heating and cooling cycles over a selected temperature range. As the name suggests, DTA measures the difference in temperature between a sample and an inert reference material in a common environment. The reference material is selected such that it undergoes no phase transformation over the range of interest (two common reference materials are Al_2O_3 and SiO_2). The temperature difference between the sample and reference material is recorded as a function of environmental temperature, a plot of which is referred to as a thermogram.

a) Apparatus

A Perkin Elmer 1700 DTA system was used in this study. The model 1700 is a micro-computer controlled high temperature differential thermal analyzer unit consisting of a system 7/4 Thermal Analysis Controller, a DTA 1700 Differential Thermal Analyzer and data processing station. A Hewlett-Packard plotter is used to graphically display the output signal. The DTA 1700 system with accompanying plotter is illustrated in Figure 24.

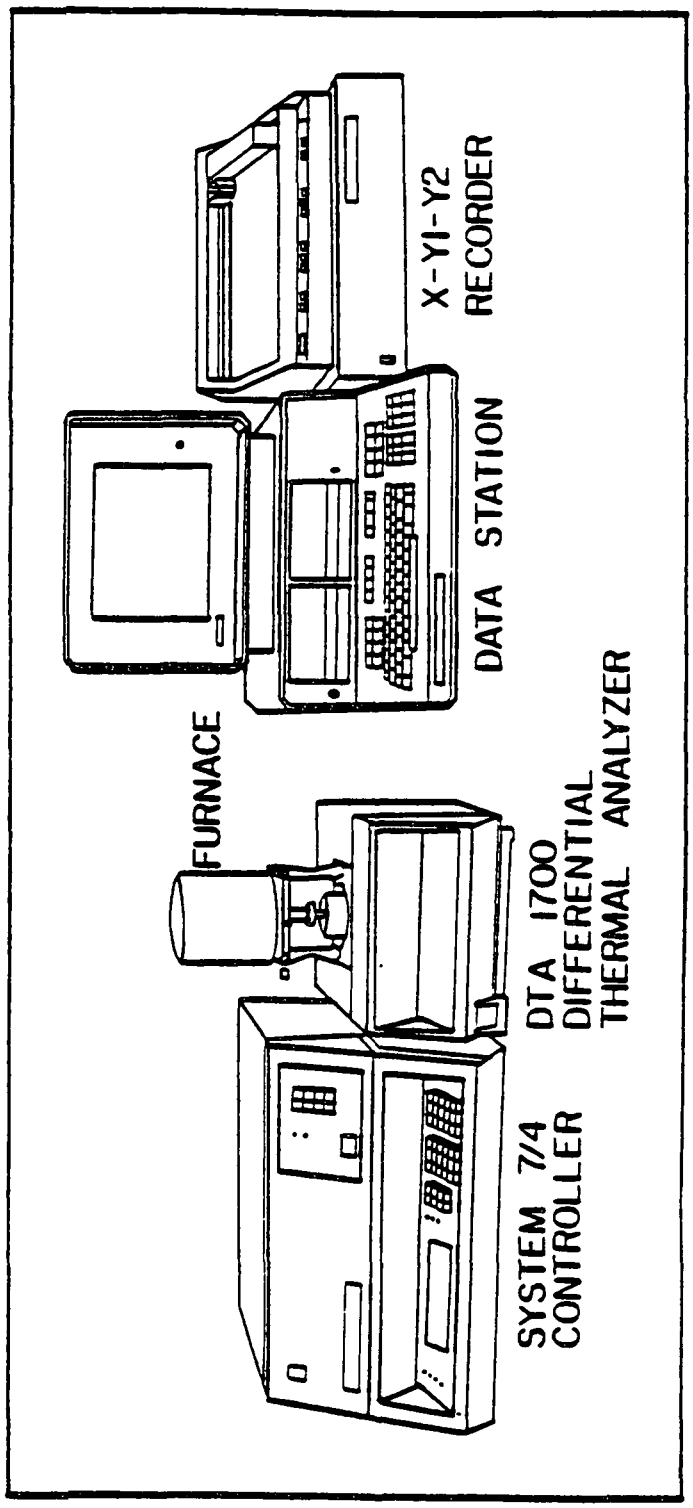

Figure 24. Schematic illustration of the Perkin-Elmer DTA 1700 system.

The system 7/4 Controller is a programmable micro-computer which regulates the furnace temperature such that it corresponds to the desired program temperature. It also monitors the differential temperature signal, providing several scaling and conditioning functions to optimize the output signal.

The DTA 1700 Analyzer consists of a Pt/Pt-40% Rh wound furnace with a temperature range from ambient to over 1400°C. The sample and reference materials are contained in aluminum oxide or silicon oxide liners (having a capacity of 60 mm^3) within a controlled atmosphere in the furnace. The liners are seated in platinum cups fitted atop tandem Pt/Pt-10% Rh thermocouples which monitor both the environment temperature and differential temperature between the sample and reference material, as illustrated in Figure 25. The reference materials used in this study were Al_2O_3 and SiO_2 (quartz). Atmospheric conditions within the sample/reference chamber are maintained through a high purity argon gas purge conditioned so as to limit residual O_2 and H_2O vapor to a minimum (86). The flow rate of the purified argon gas into the DTA system is held between 30 and 55 cc/min.

The Data Station is a micro-computer whose primary

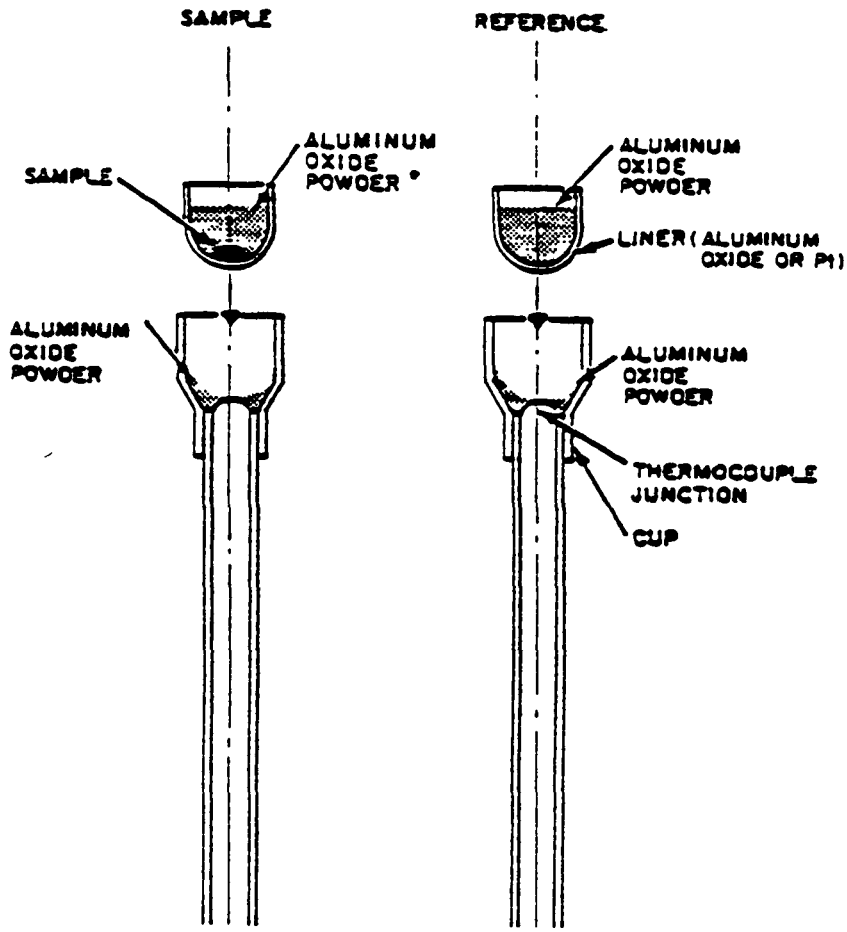

Figure 25. Illustration of the sample/reference configuration within the DTA 1700 system.

functions are to store raw data, optimize the thermal curves, perform data analysis and store the results of any such analysis. Data is stored on floppy disks and may be retrieved at any time for further reference and analysis. The Data Station may also be used to control the System 7/4 Controller.

b) Interpretation of Thermogram

A schematic representation of a DTA thermogram is shown in Figure 26. The curves are characterized by a baseline from which endothermic or exothermic reactions are observed during a phase transformation. An endothermic event is distinguished by a negative deviation from the baseline indicating absorption of heat by the sample which typically is the result of a melting reaction. An exothermic event is characterized by a positive deviation from the baseline indicating evolution of heat from the sample and is typically representative of a solidification reaction.

The melting point of a pure component or an invariant reaction in an alloy (such as the melting of a line compound or eutectic mixture) is shown as a negative spike in the curve. The temperature of this reaction is taken to be the onset of the endothermic

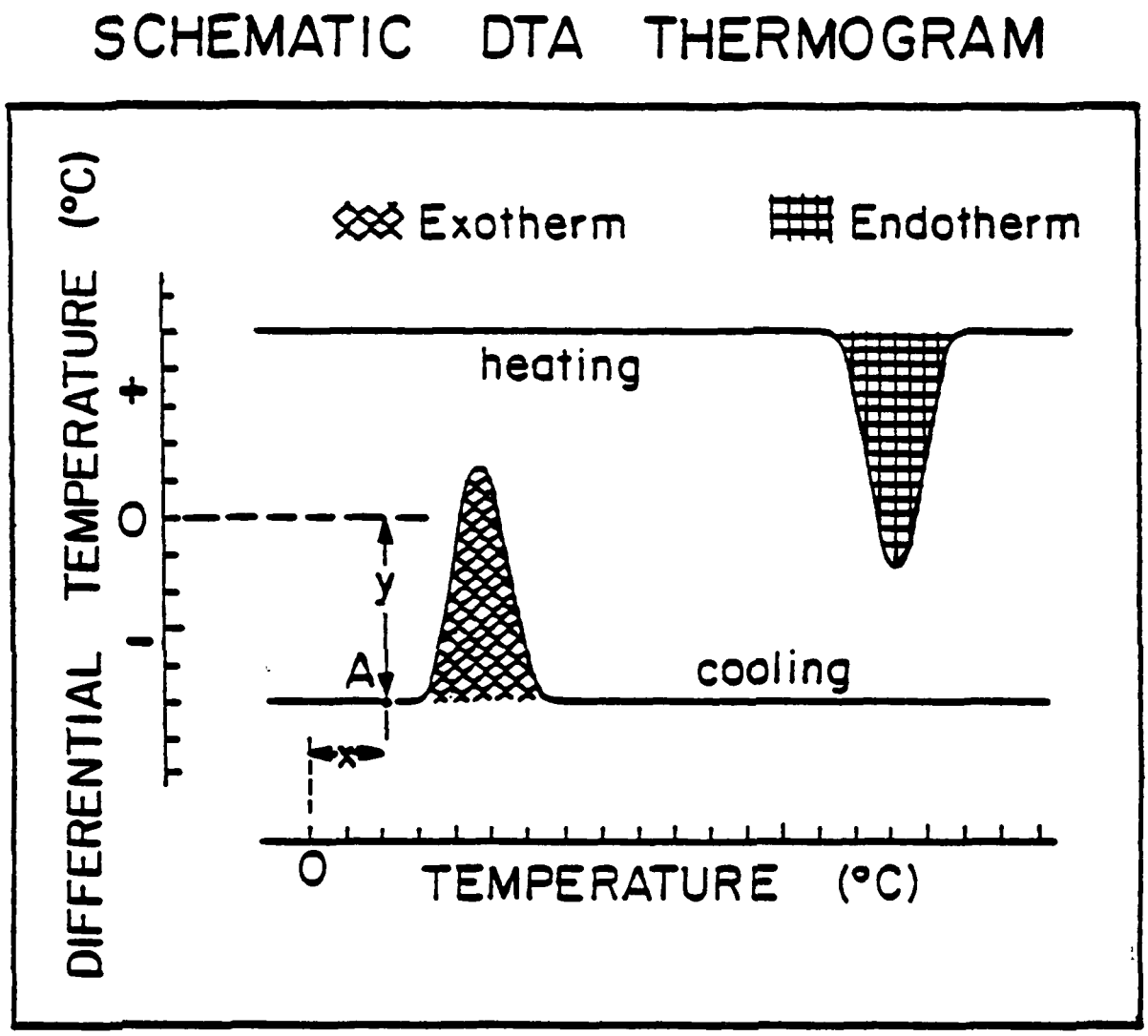

Figure 26. Schematic illustration of a DTA thermogram.

peak. The melting of a solid solution is seen as a gradual endothermic event with a more rapid rise to the baseline at the liquidus temperature. Temperatures associated with nucleation events are generally taken to be the maximum of the exotherm, however, application of certain cycling treatments may be used to reveal any significant exotherms in the tail region of the curve. Figure 27 illustrates typical temperature measurements taken from a DTA thermogram.

Quenching Apparatus

Specimens which are processed using the DTA 1700 system are unavoidably subjected to annealing treatments following solidification. This occurs due to the relatively slow cooling rate ($20^{o}C/min$) imposed during the analysis and the rather high nucleation temperature (relative to the melting point) of the sample. This annealing treatment is undesirable in that it encourages not only coarsening and alteration of the solidification structure, but also may allow for decomposition of metastable phases and supersaturated solid solutions prior to sample removal and subsequent structural analysis. The imposition of a more rapid cooling rate would discourage these effects while simultaneously promoting the attainment of deeper levels of undercooling.

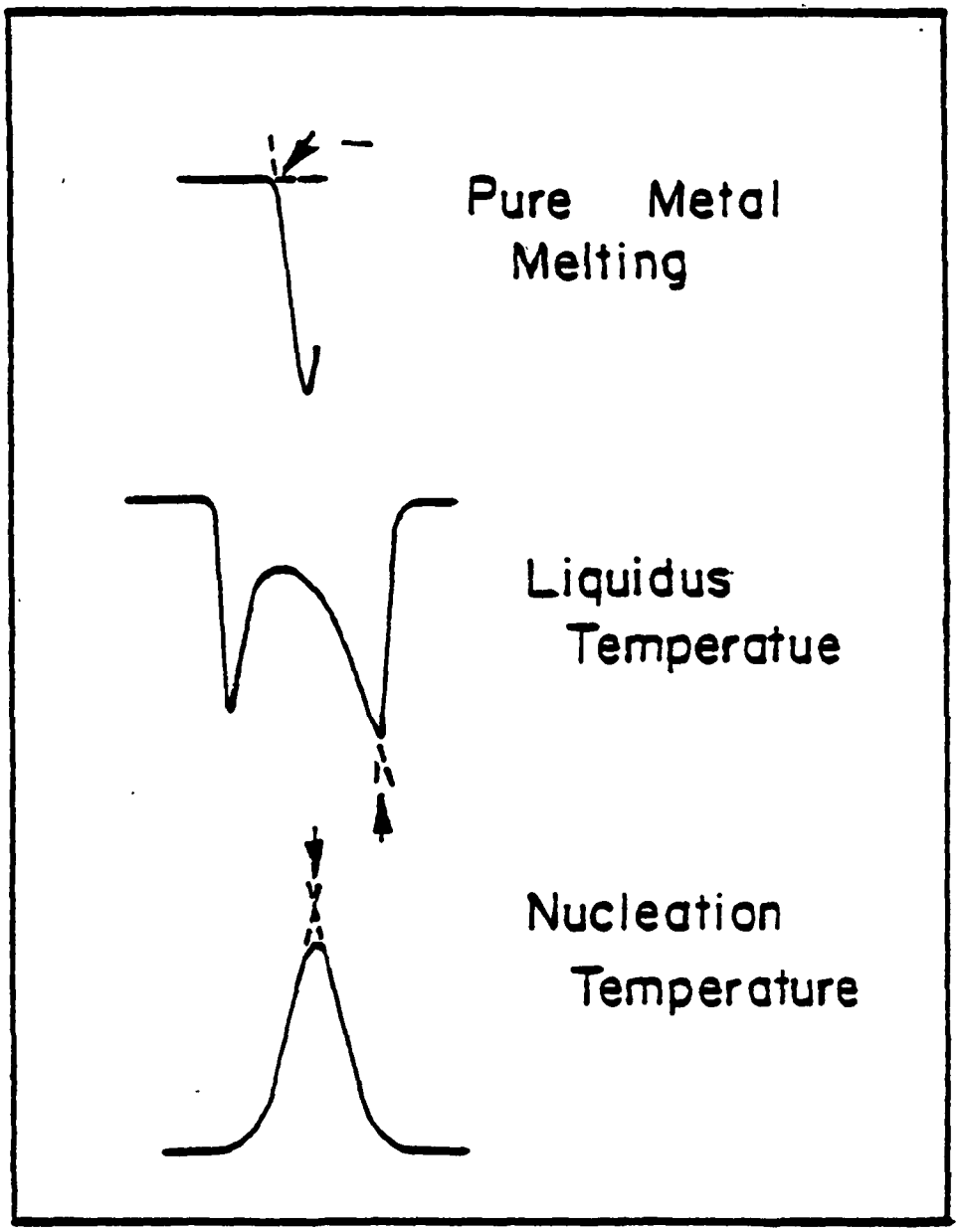

Figure 27. Examples of reaction temperature measurement with a DTA thermogram.

An apparatus which is capable of attaining these goals was developed in previous studies by LeBeau (86), Mueller (87) and Regan (88). The droplet sample is packed into a stainless steel tube (2.4 mm o.d., 1.65 mm i.d. and 4.5 cm in length) which is sealed on one end with a refractory cement. A fine gauge (36 AWG) chromel-alumel thermocouple is inserted into the powder through the open end of the tube. The small tube is then attached to a stainless steel support rod which is held in the hot zone of a vertically mounted tube furnace. Upon reaching the desired temperature the support rod is released allowing the sample to fall from the furnace into the open air or an ice water bath, depending on the desired cooling rate. Figure 28 illustrates the main features of the quenching apparatus.

The voltage output of the sample thermocouple is monitored as a function of time during both the heating and cooling cycles through the use of a Nicolet digital oscilloscope (model 201). Thus the temperature at which a phase transformation occurs as well as the cooling rate during any portion of the thermal cycle may be obtained. The digital oscilloscope also has the capability of storing the thermal results on floppy disks, allowing retrieval and further manipulation or plotting at a future time.

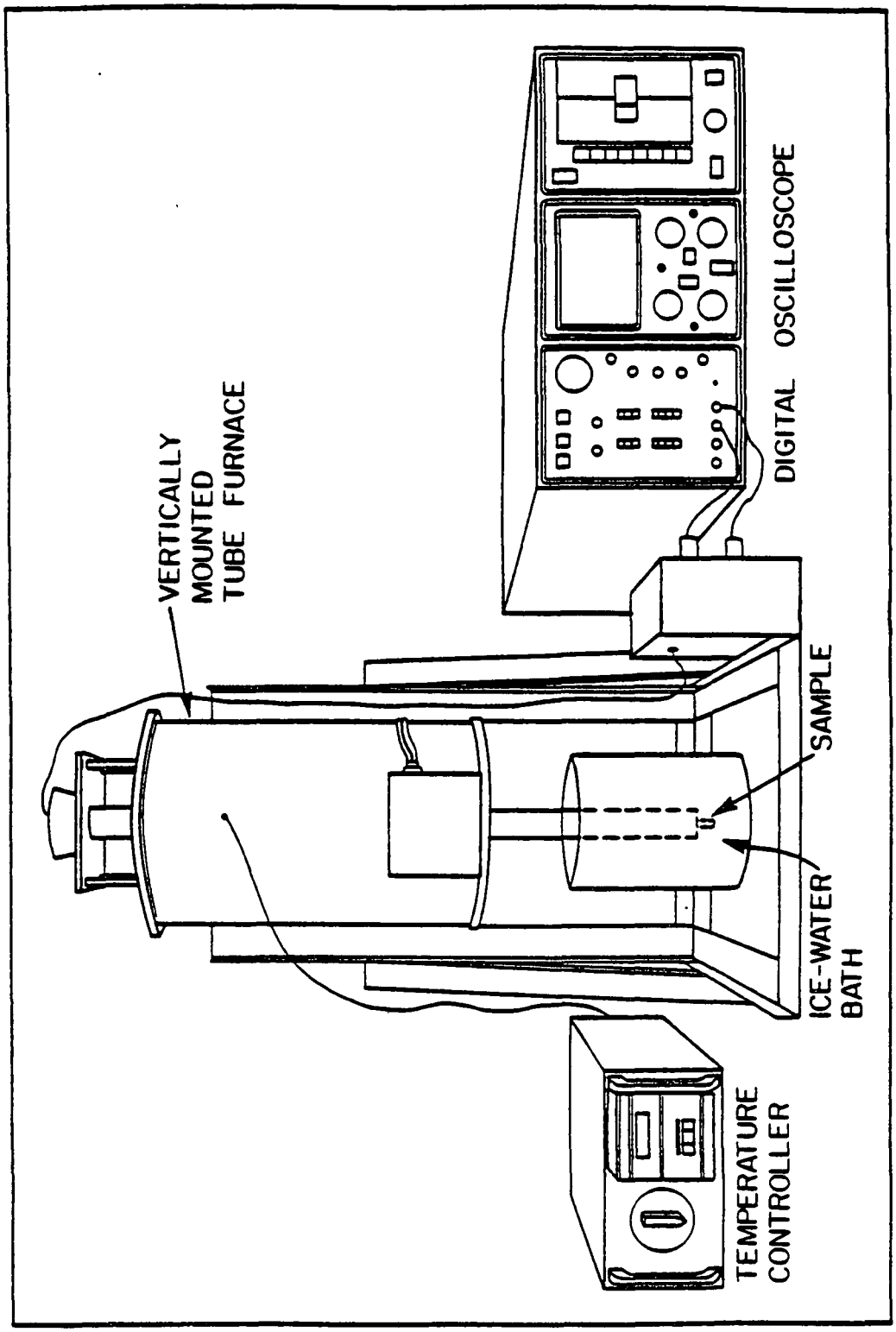

Figure 28. Schematic illustration of the quenching apparatus.

Drop Tube Apparatus

A portion of the current investigation is devoted to a microstructural comparison of powder samples processed in the DTA 1700 system and quenching apparatus to those processed in a recently developed laboratory scale drop tube. The drop tube is an environmentally isolated cylindrical quartz chamber three meters in length through which powder specimens are allowed to free fall, both melting and solidifying in transit. The drop tube offers the capability of processing powders under vacuum or in an inert gas environment. Due to the relatively low melting points of the materials used in this investigationmost processing was carried out in a helium gas environment at a pressure slightly greater than one atmosphere. Melting of the powder is accomplished by passing the sample through a resistance heated tantalum coil in the uppermost region of the chamber. Subsequent cooling and solidification of the molten droplets occurs as their free fall continues through the tube chamber. The processed powder is then collected in a detachable quartz cup at the bottom of the tube for structural evaluation. A schematic illustration of the drop tube apparatus is provided in Figure 29.

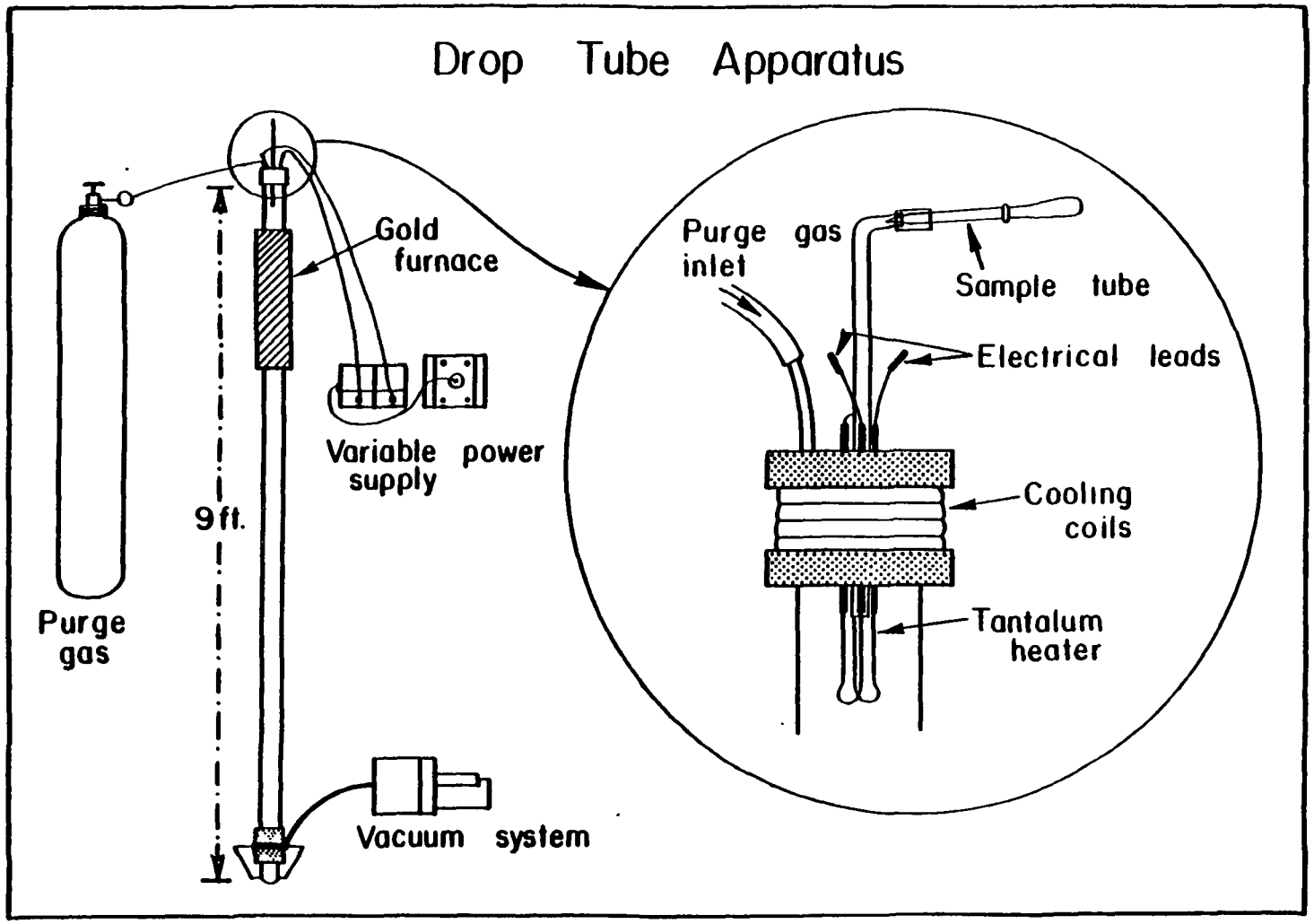

Figure 29. Schematic illustration of the laboratory scale drop tube apparatus.

Differential Scanning Calorimetry

Differential scanning calorimetry (DSC) is a technique used to study the thermal behavior of samples when heated or cooled. As used in this investigation, DSC provided information similar to that of DTA however use of DSC allowed cooling rates of 0-80°C/min to be obtained while also enabling the sample to be brought to room temperature within seconds of completing the final thermal cycle thereby minimizing potential coarsening in the solid state. The upper temperature limit was maintained at 550°C allowing both InSb and the InSb-Sb eutectic alloy to be processed with this technique.

DSC was conducted with a Perkin-Elmer 7 Series Thermal Analysis System which uses a micro-computer to both control the DSC 7 Differential Scanning Calorimeter and process the thermal signal upon completion of cycling. DSC differs from DTA in that the computer monitors the power required to maintain a known mass of sample at the same temperature as that of a reference material as both are heated or cooled. In this manner the heat absorbed or evolved during a cycle may be accurately evaluated providing information on the heat of transformation in addition to the melting and crystallization temperatures for the sample material.

X-ray Diffraction

Prior to microstructural observation, x-ray diffraction techniques were employed to evaluate the phases present in the processed powders. These specimens are ideally suited to powder diffraction techniques and thus both the diffractometer and Debye-Scherrer powder methods were used. A Picker, model 36668A, x-ray diffractometer provided most information and was used with a Cu target operating at 30 kV and 15 mA. However, on occasion, the sample amount would be too small to use the diffractometer method. In these instances the Debye-Scherrer powder method was employed. The camera used was 114 mm in diameter and was most effective when used with a Cu target and exposure times of approximately 6 hours. The nonsymmetrical or Straumanis method of film loading was used thereby eliminating the need to determine the amount of film shrinkage which occurred during processing. Both x-ray methods were effective in determining the phase identity of the processed powders.

Metallography

In order to examine the microstructure of both the bulk and powder specimens a cold mounting technique was employed which used an epoxy resin bonding agent as a

supporting media. After mounting, the samples were first ground smooth using 400 and 600 grit silicon carbide papers and then polished with 1.0, 0.1 and 0.05μm alumina solutions dispersed on a medium nap cloth. Samples were ultrasonically cleaned in distilled water between each grinding and polishing step to minimize the carry-over of abrasive by-products.

The Sb specimens were examined primarily in the unetched condition due to their favorable response to polarized light. Representative Sb samples were selected to be chemically etched using a 33% HF-17% HNO_3-50% glycerol solution in order to detect the presence of any solute contamination which may have occurred during the emulsification process.

The eutectic alloy required no etching for optical examination due to a large difference in optical reflectivity between the constituent phases. Examination with the scanning or transmission electron microscope, however, required the application of a saturated ferric chloride-methanol etching solution to the eutectic specimens. The etching time for TEM purposes was approximately 3-5 seconds while SEM examination required 12-15 seconds of application.

Examination of Microstructures

Initial examination of all microstructures was conducted on a Zeiss optical microscope having magnification capabilities in excess of 2300X. This magnification range proved to be adequate for examination of all Sb specimens. In addition the microscope offered the capability of using polarized light to reveal the presence of grain boundaries within the optically anisotropic Sb powders.

To achieve higher resolutions a JEOL model JSM-35C scanning electron microscope (SEM) was used. Image formation was primarily derived from secondary electrons however backscattered electron image formation was occasionally used in order to provide information on compositional variations within the sample. All specimens were coated with gold prior to examination with the SEM.

Certain of the eutectic specimens required a greater resolution than that available with the SEM. For these cases a transmission electron microscope (TEM) was employed through the use of a surface replication technique. This technique involved the following procedure:

1) Application of 2 layers of a collodian resin solution providing a fragile, but detailed replicate of the surface.

2) Application of an acetylcellulose "replication solution" which bonds with the collodian layers and strengthens them.

3) Stripping of the bonded layers away from the sample surface.

4) Evaporation and deposition of a thin carbon layer onto the acetate replica.

5) Dissolution of the acetate film using an acetone bath followed by an acetone vapor wash for 24 hours.

6) Shadowing of the carbon film with a metal of high atomic number such as Au, Cr, Pt or Pd (in this case Pt was used) to provide contrast in the image.

For the powder samples involved in this study the most critical step was the removal of the acetate film from the carbon. As the film begins to dissolve it tends to expand, forcing the carbon to fragment in the process. This effect is enhanced due to a more severe attack of the etching solution at the droplet perimeter which leaves a surrounding groove and corresponding stress concentration region in the carbon replica. Through a careful sample preparation technique, in which the etching time is minimized, this effect is sufficiently reduced to yield a highly detailed surface replica with resolution capabilities approaching 10^2 Å.

EXPERIMENTAL RESULTS

In order to conduct a comprehensive investigation of a eutectic alloy, particularly one in which both constituents tend to exhibit a faceted growth morphology with a corresopnding increased sensitivity to imposed growth conditions, it is beneficial to examine first the behavior of the pure constituent phases. As such, the earliest stages of this study were devoted to examination of the undercooling and crystallization behavior of the pure constituents, InSb and Sb.

Undercooling Behavior of Pure Antimony

a) Undercooling of Bulk Antimony

As a precursor to the application of droplet techniques for the study of the undercooling behavior in pure antimony it is necessary to characterize the behavior of the bulk material. One focal point of the study was to be the effect of material purity on undercooling. As such both 99.8% and 99.999% bulk antimony ingots were examined, the results of which are presented in Figure 30. The ingot of lower purity crystallized at 556°C ($\Delta T = 75°C$) while the high purity ingot crystallized at 552°C ($\Delta T = 79°C$), an increase of 4°C in undercooling. These nucleation temperatures were consistent

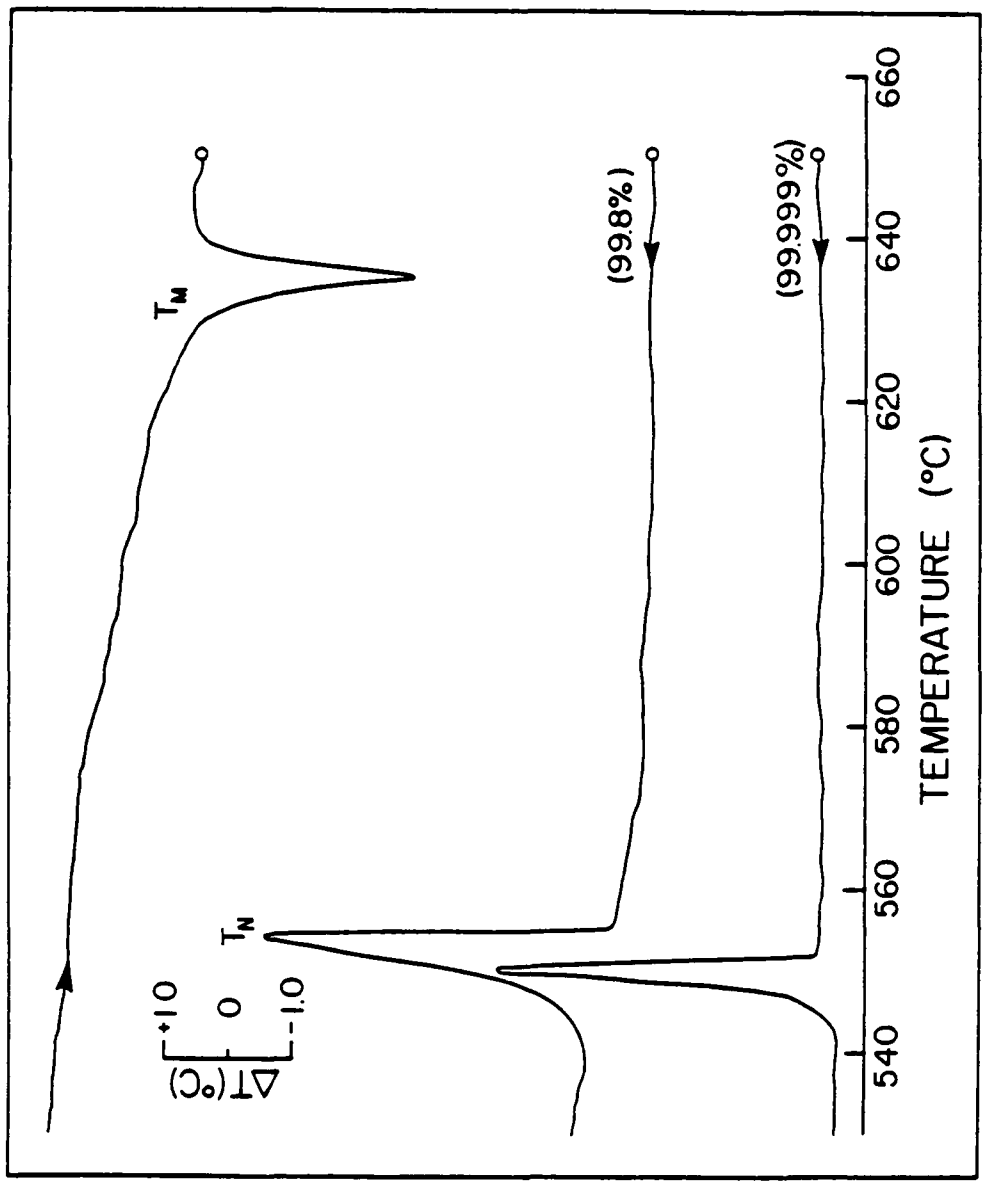

Figure 30. Undercooling behavior of bulk antimony of 99.8% and 99.999% purity.

through repetitive cycling treatments.

Antimony is a material in which the natural oxide coating, Sb_2O_3, has a melting point only slightly above that of the pure material ($T_{M(Sb)} = 631^{\circ}C$, $T_{M(Sb_2O_3)} = 656^{\circ}C$). It was therefore of interest to heat above this level and observe the effect on subsequent undercooling of the liquid. In addition to possible coating effects, an increase in superheat could act to alter the potency of internal nuclei present in the melt. Thus, the ultimate melt temperature was varied over the levels 550°, 700°, 750° and $800^{\circ}C$, the results of which are illustrated in Figure 31. The undercooling in each case varied less than 2°, with the nucleation temperature being $552^{\circ}C$.

b) Undercooling of Crushed Antimony

Following initial trials with bulk Sb ingots, crushing was used to create powder which would have a coating similar to that of the bulk material, but would make use of nucleant isolation techniques to enhance undercooling. Due to the relatively low melting point of the oxide coating, the Sb powder was diluted with 0.05μm Al_2O_3 to maintain droplet independence during

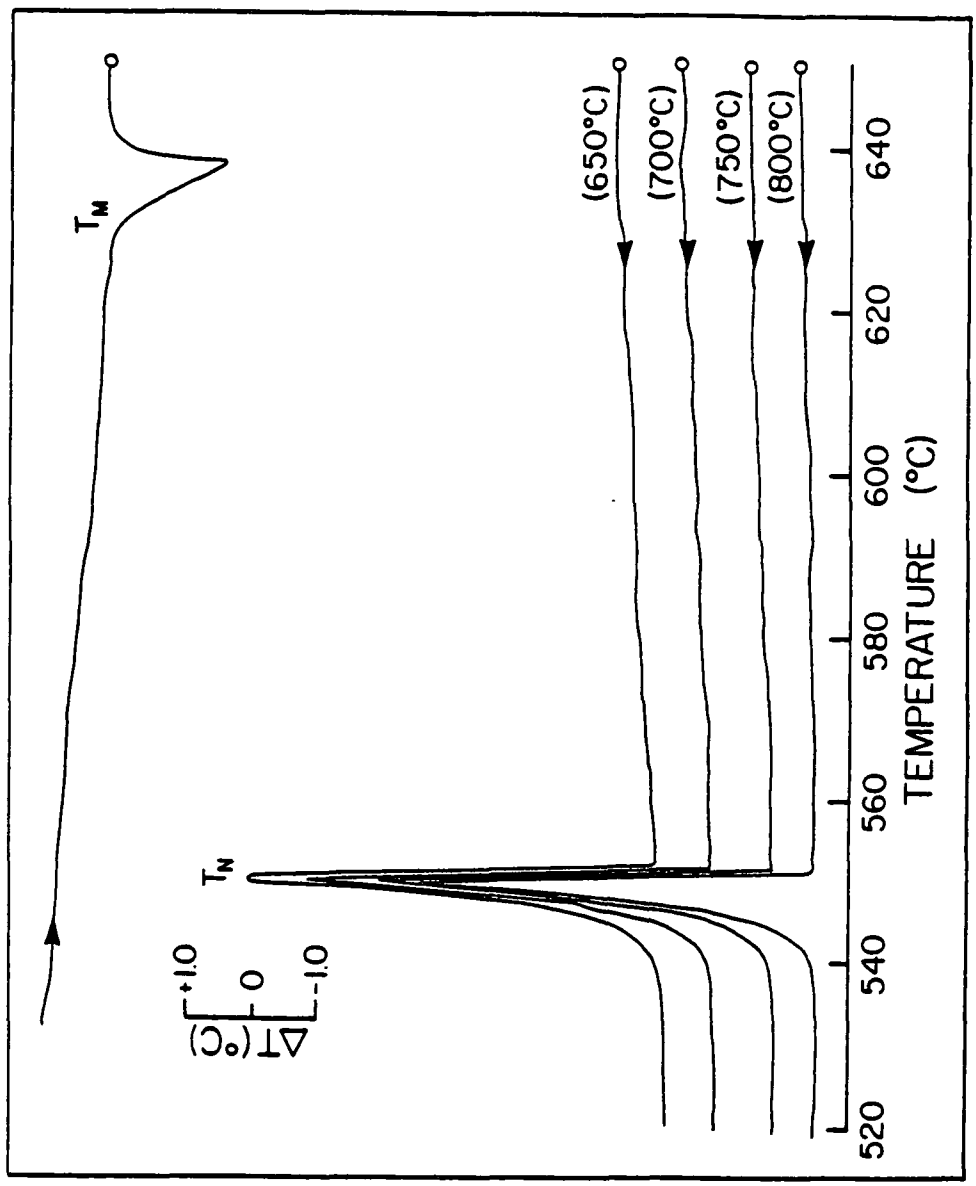

Figure 31. Effect of superheat on the level of undercooling in 99.999% pure bulk Sb.

thermal cycling. A comparison of undercooling response for 20-44μm powder to that of the bulk Sb is illustrated in Figure 32. The undercooling of the droplet sample (T_N = 472°C, ΔT = 159°C) exceeds that of the bulk by approximately 80°C.

c) Emulsification of Antimony

Examination of the undercooling and crystallization behavior of Sb droplets was carried out primarily using emulsified powder. Proper use of this technique yielded droplets whose surface coating was stable to temperatures in excess of 800°C. Dissolution of the carrier salt, however, was accompanied by formation of a white precipitate which remained with the Sb powder throughout subsequent processing. While this diluent played no observable role in the undercooling behavior of the droplets, its presence was detected during the x-ray diffraction portion of the study.

The surface coating produced during emulsification treatment was approximately 1-3μm in depth. While this coating was successful in maintaining droplet independence, its thickness significantly reduced the thermal signal for the finest powder and made precise size classification more difficult. A reduction in

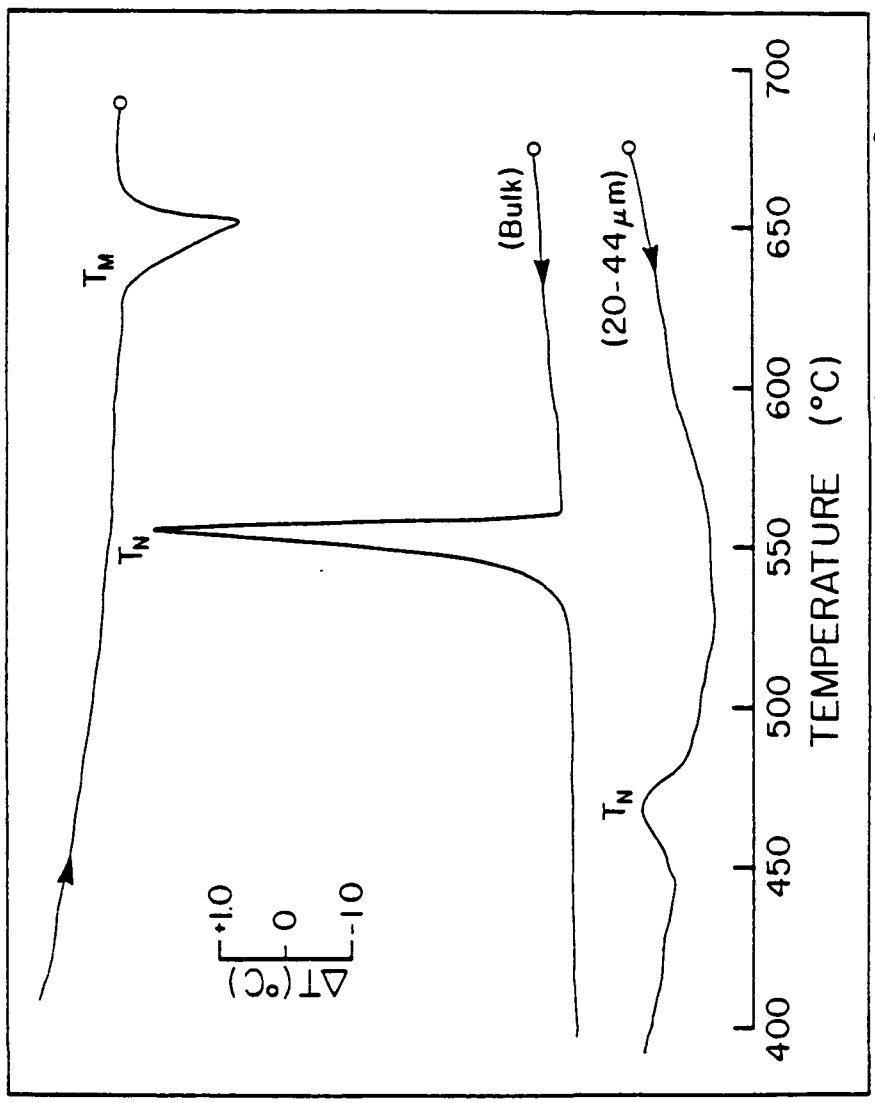

Figure 32. Comparison of undercooling response for bulk and crushed antimony.

emulsification time reduced the thickness of the coating, however, below a certain limit (approximately 3 minutes) the particle size distribution became very coarse. Figure 33 presents both exterior and cross-sectional views of the emulsified powders following DTA processing.

In order to detect evidence of solute contamination in the powder, representative samples were chemically etched both before and after DTA treatment. In no case was there any indication of contamination. In addition, all sample cross-sections were examined under polarized light in order to reveal grain boundaries within the droplets. For both the crushed and emulsified samples no evidence of multiple grain particles was found either before or after thermal processing.

d) Size Effect on Undercooling

According to theories on nucleant isolation, subdivision of a bulk material into individual particles should isolate the most potent catalysts into a small fraction of the droplet population allowing the remainder to undercool to a greater extent prior to nucleation (19). In the case of pure Sb this effect of droplet size on undercooling was examined using emulsified

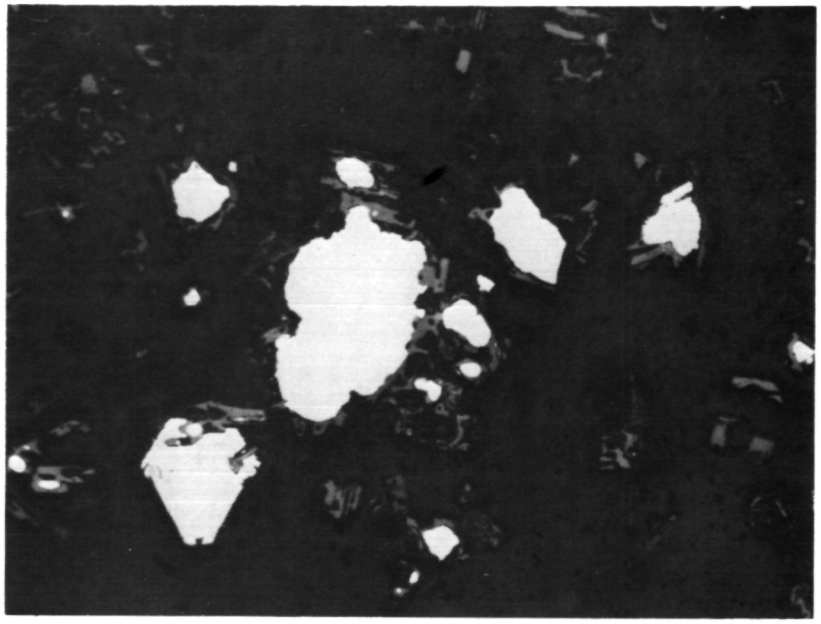

(a)

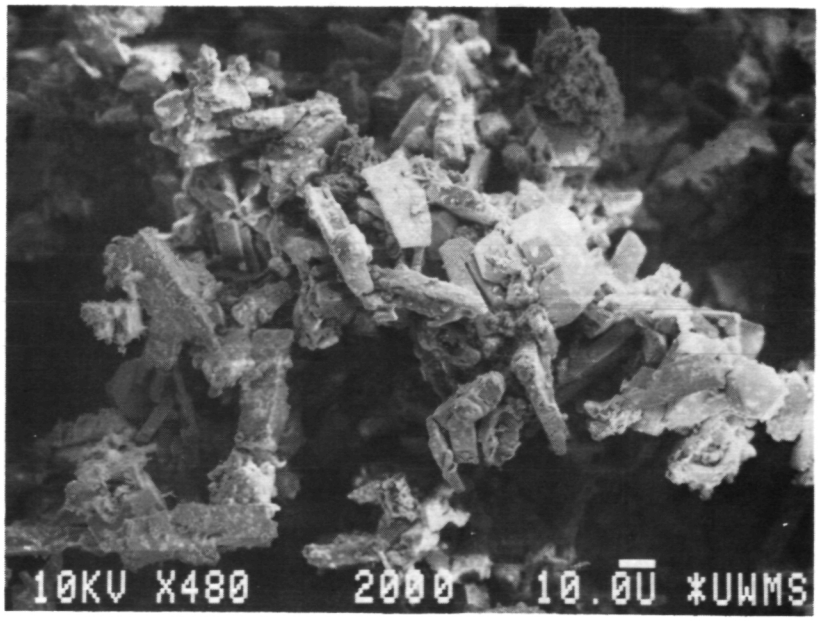

(b)

Figure 33. (a) Optical micrograph of Sb powder in cross-section. 400X.
(b) SEM micrograph showing exterior of Sb powder. 480X.

powder with size ranges of 18-28, 28-38, 38-44, 63-88 and 88-150μm. The results are presented in Figure 34. As the droplet size is reduced an increase in the level of maximum undercooling (T_N = 499°, 496°, 489°, 481° and 461° respectively) is observed. There is also a considerable overlap in the nucleation peaks indicating that a variety of catalysts were active in each droplet sample. Thermal cycling treatments in which the liquid sample is cooled slightly into the nucleation region, quickly reheated to a temperature below the melting point and cooled once again through the nucleation region have shown these crystallization exotherms to be a series of overlapping peaks which can account for the broadness and roughness of the curves illustrated in Figure 34.

e) Superheat Effect on Undercooling

One way in which the level of undercooling obtained in a droplet sample may be altered is through a change in the degree of applied superheat (i.e. the temperature above the melting point to which the sample is heated) (87). This change in undercooling may arise due to a number of reasons including alterations (either temporary or permanent) in the droplet surface coating and/or potency of internal catalytic sites. For Sb droplets

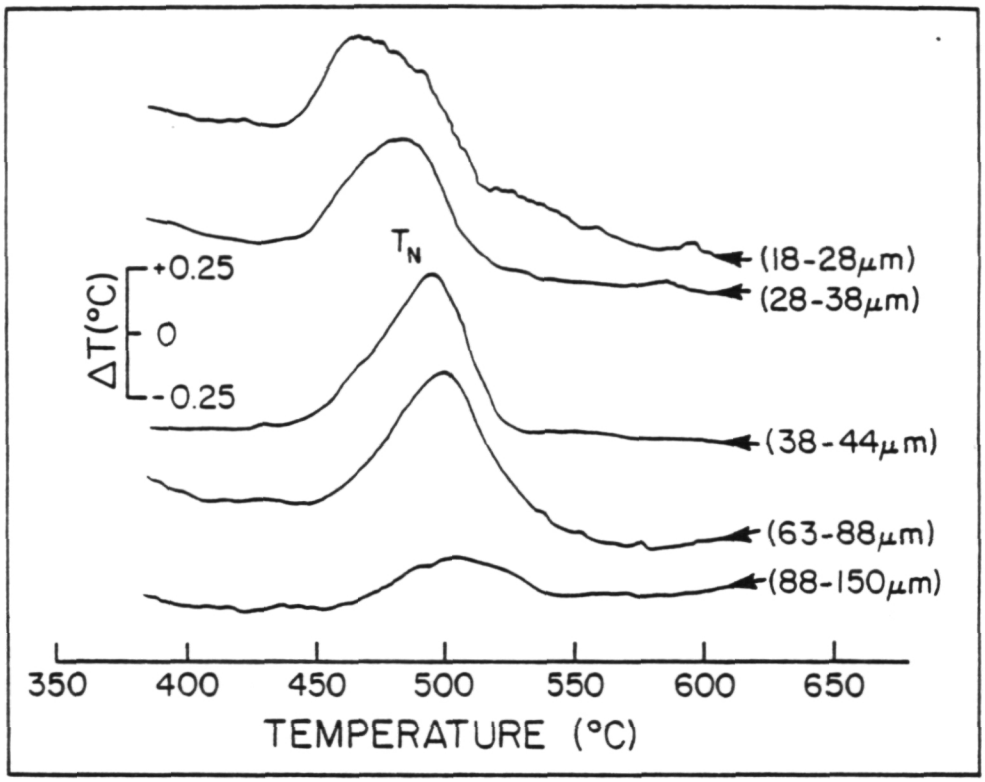

Figure 34. Effect of droplet size on the undercooling of pure (99.8%) antimony.

created through emulsification the levels of superheat examined included 640°, 680°, 700°, 750° and 800°C. Above 800°C the coating on the droplets began to fail allowing a large degree of coalescence to occur with a subsequent degradation in undercooling. Figure 35 presents the results of this portion of the study for which the droplet size distribution remained relatively unchanged. Little change in undercooling is observed until 700°C is exceeded, whereupon the nucleation temperature increases slightly (T_N = 490°C) before decreasing once again as the temperature is extended to 750°C (T_N = 471°C). At the highest level of superheat, 800°C, the peak of the crystallization exotherm returns to approximately the original value (T_N = 486°C) however a more significant variation in undercooling is now found to exist. Further cycling revealed that a retreat to lower levels of superheat returned the peaks to their previous positions indicating that the change in level of superheat did not permanently alter the undercooling characteristics of the droplet sample.

f) Purity Effect on Undercooling

In order to examine the effect of initial material purity on undercooling behavior two size ranges of droplets (28-38μm and 44-63μm) were selected from emulsions

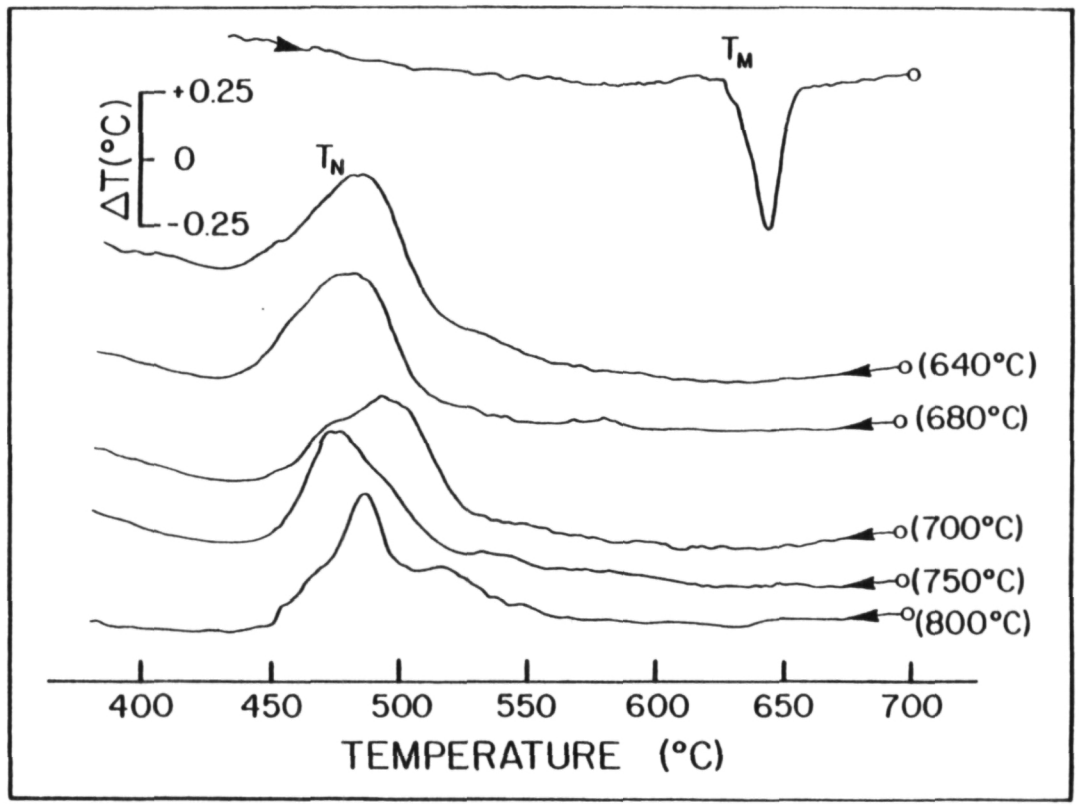

Figure 35. Effect of a change in superheat temperature on the undercooling behavior in pure (99.8%) antimony droplets (28-38μm).

of 99.8% and 99.999% purity. The responses obtained during identical thermal cycling treatments are presented in Figure 36. The larger size droplets (44-63μm) produced undercoolings of 136° and 153°C while the smaller droplets (28-38μm) gave 150° and 167°C of undercoolings for the 99.8% and 99.999% pure samples, respectively. In addition, for both size groups the higher purity material produced a more uniform crystallization behavior in which the major portion of the sample solidified over a relatively narrow temperature range (when compared to that of the less pure material).

g) Coating Effect on Undercooling

Based upon previous studies (21) the nature of the droplet surface coating may have a significant influence upon the level of undercooling obtained in a droplet sample. In order to explore this contingency in pure Sb a comparison may be made between droplets produced through crushing and those obtained by emulsification. The crushed droplets' coating is that of a simple oxide, Sb_2O_3, while the emulsified droplets are encased within a more complex surface coating. In order to minimize extraneous effects due to droplet size differences, 20-44μm crushed powder and 28-38μm emulsified powder

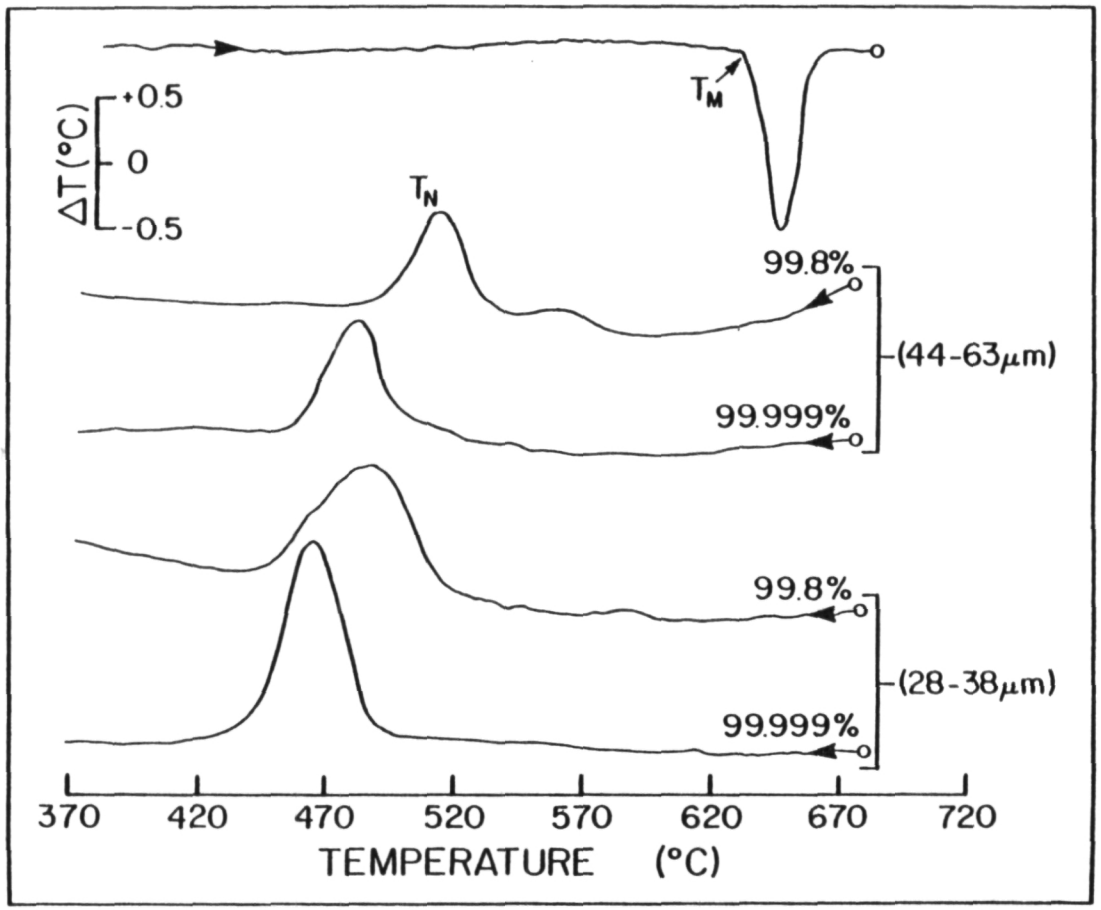

Figure 36. Effect of initial material purity on the undercooling behavior of antimony droplets.

was used in the comparison. Figure 37 presents the results of this portion of the study which reveal undercooling levels of 141°C and 167°C for the crushed and emulsified samples respectively. Thus, altering the surface coating has led to an increase of 26°C in the level of undercooling for pure antimony.

h) Quenching Study

In order to both reduce possible annealing effects of the relatively slow cooling of DTA samples from the nucleation region to ambient temperature and to evaluate the effect of an increase in cooling rate on the undercooling behavior of Sb, a rapid quench technique was employed using emulsified powder of size 38-44μm. While this size of droplets did not provide the deepest levels of undercooling in DTA studies, the increased volume was deemed necessary in order to enhance detection of transformation peaks. Cooling rates obtained using this technique were approximately 16°C/sec for air cooling and 500°C/sec for quenching into an ice water bath. Upon heating, the melting endotherm was centered at 630°C but extended approximately $\pm$ 5°C. Nucleation temperatures were determined to $\pm$ 5°C with air cooling, but were less well defined when using the water quench and are thus cited as $\pm$ 10°C for this method. Table III presents

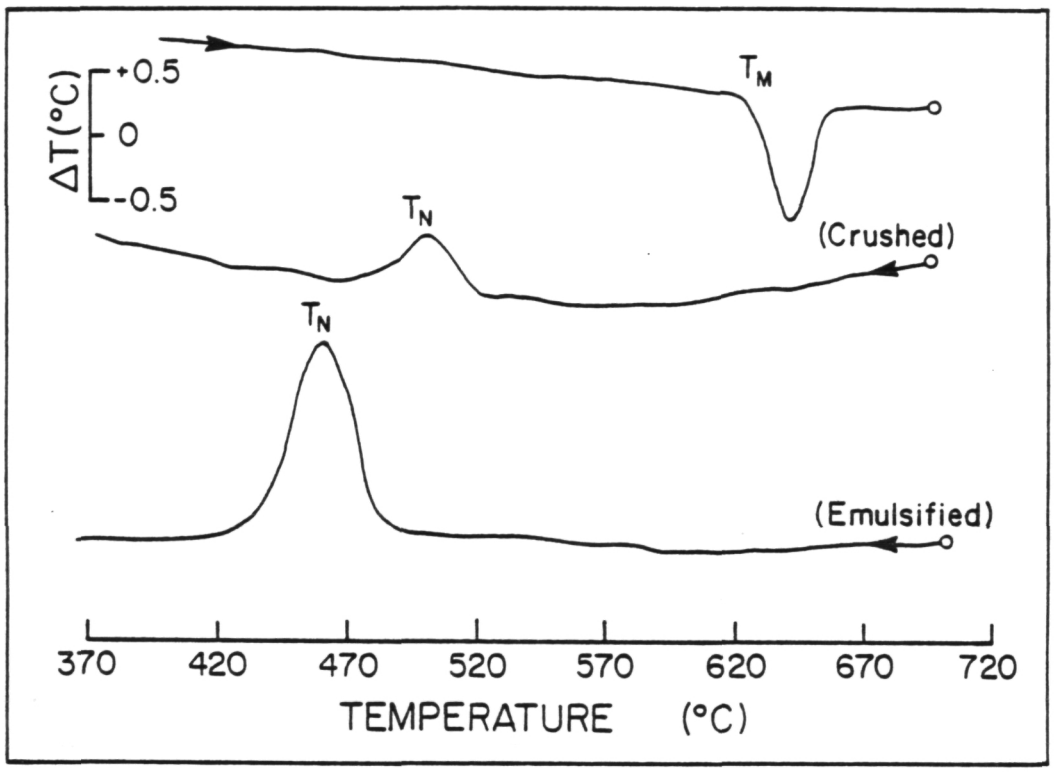

Figure 37. Comparison of the undercooling behavior for crushed and emulsified Sb powders.

TABLE III

Undercooling values obtained with emulsified Sb powder (38-44μm).

Technique	Approximate Cooling Rate (°C/sec)	ΔT (°C)
DTA	0.33	142
Air Quench	18	139 ± 5
	15	141 ± 5
Water Quench	540	213 ± 10
	560	216 ± 10

undercooling data for this portion of the study, comparing DTA values to those obtained with the quenching technique. Air quenching data indicate no appreciable increase in level of undercooling compared to that obtained using DTA, however, when water is used as a quench medium an approximately 74°C increase in undercooling is detected.

i) Melting Behavior of Antimony Droplets

Through use of the droplet emulsion technique previous efforts have been successful in producing metastable crystalline phases in pure materials which undergo high pressure polymorphic transformations such as Ga and Bi (3). As antimony falls in a similar category, the possibility of producing metastable phases from undercooled Sb droplets was considered during the application of thermal cycling treatments in this investigation. While no visible exothermic reactions (indicative of a metastable→stable solid state phase transformation) were encountered upon heating with DTA the melting endotherm often appeared as a slightly asymmetric peak. One cause of asymmetry in DTA peaks can lie in the overlap of two transformation peaks occurring at near equivalent temperatures. To explore this possibility for the melting

behavior of Sb droplets, the thermal cycling treatment illustrated in Figure 38 was applied. The powder sample was first carried through a complete melting/solidification cycle to determine the temperature range of these reactions. After cooling well below the nucleation peak (to approximately 300°C) the sample was reheated to a temperature slightly beyond the initial deviation from the baseline (approximately 627°C), point "A" in Figure 38. At this point an isothermal hold was imposed for 6 minutes in order to allow adequate time for any thermal gradients within the furnace chamber to be eliminated. The sample was then cooled to approximately 560°C to establish a new baseline and reheated completely through the melting region. A distinct melting endotherm is once again observed, however, the onset temperature has now increased slightly over the initial onset (cycle 1). The entirely liquid droplet sample is then cooled to approximately 560°C and reheated again through the entire melting region. The occurrence of a relatively minor melting endotherm confirms that no significant degree of crystallization had occurred during the previous cooling cycle. Thus, thermal cycling suggests that the asymmetry of melting endotherms

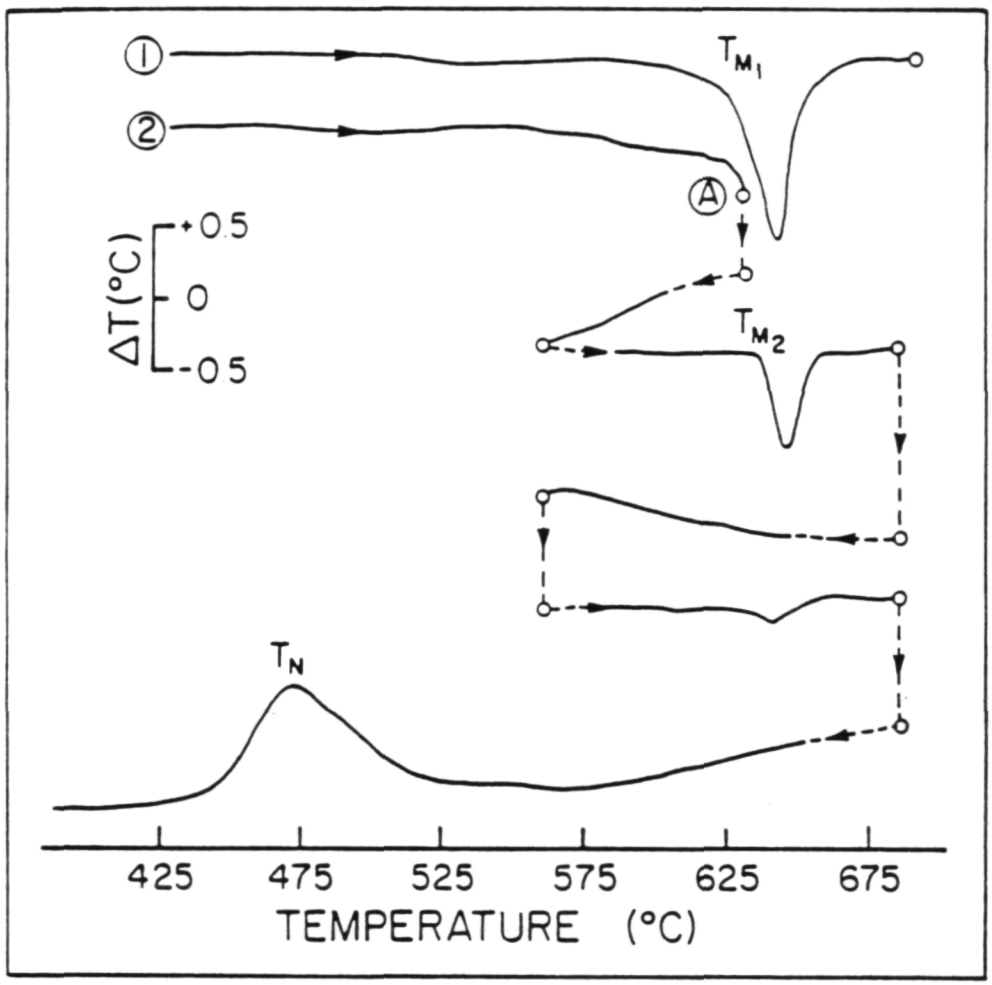

Figure 38. Illustration of the thermal cycling treatment applied to a -18μm emulsified Sb sample. Point A denotes the temperature at which the sample was isothermally held for 6 minutes.

observed following initial crystallization of undercooled Sb droplets may in fact be attributed to the overlap of dual melting peaks separated by only a few degrees.

j) Drop Tube Studies

Droplet samples produced through both crushing and emulsification were thermally processed using the laboratory scale drop tube with the solidification structures being compared to DTA, air- and water-quenched samples. The level of superheat was minimized through the use of numerous trial runs in which the heating coil power setting was gradually increased until crushed droplets spherodized during free fall. Figure 39 presents micrographs of the crushed powder specimen both prior to, and following, drop tube processing. Due to the relatively low melting point of Sb_2O_3 the droplet coating as well as interior become molten upon heating, enabling the droplet to easily spherodize during free fall. The surface shrinkage observed in the processed droplets may be attributed to the occurrence of thermal dendrites present due to growth into the undercooled melt. Numerous fractured droplets are also observed; more detailed photos of which are presented

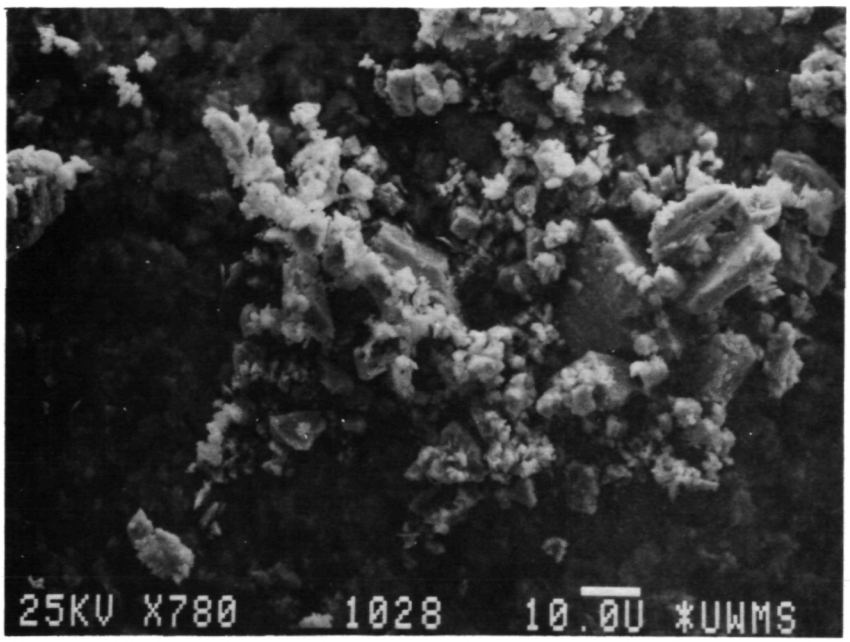

(a)

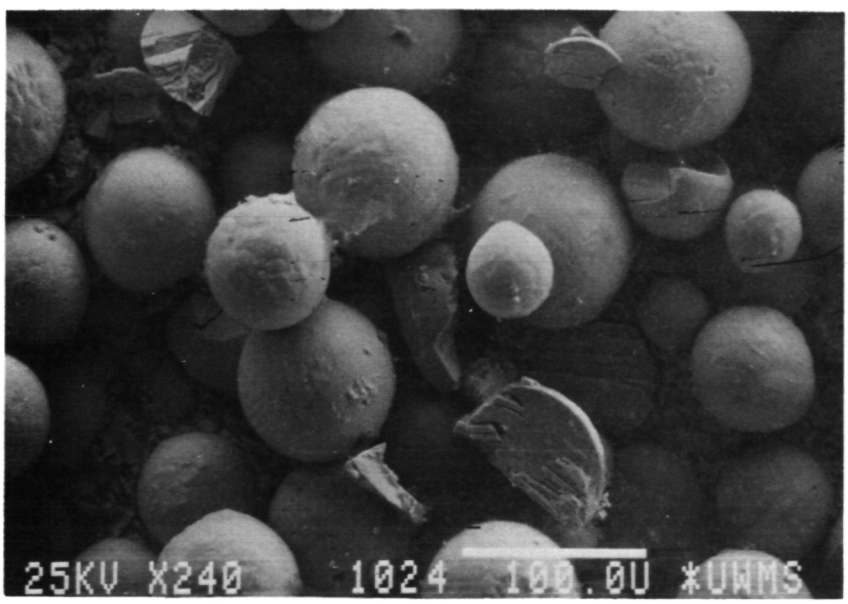

(b)

Figure 39. SEM micrographs showing the exterior of crushed Sb powder both before (a) and after (b) drop tube processing. (a) 780X, (b) 240X

in Figure 40. The fracture surface presented in Figure 40(b) reveals isolated spherical pores, the origin of which may lie in the rapid expulsion of He gas during solidification which had been absorbed as the droplet melted.

Drop tube processing of emulsified Sb powder was carried out under conditions identical to that of the crushed specimens. In this case however the droplet shape remained unaltered (i.e. identical to that presented in Figure 33). This indicates that not only did the coating remain solid during processing but it also remained rigid enough to inhibit spherodization of the Sb powder during free fall. Exterior examination revealed that no significant droplet fracturing had occurred during processing of the emulsified powder.

k) X-ray Diffraction Studies

In order to evaluate the crystal structures produced in undercooled Sb droplets, as well as to compare the results of using various processing techniques (i.e. DTA, H_2O quench, drop tube, etc.), x-ray diffraction analysis was employed both prior to and following each processing treatment. This technique was successful in producing crystal structure data which in turn

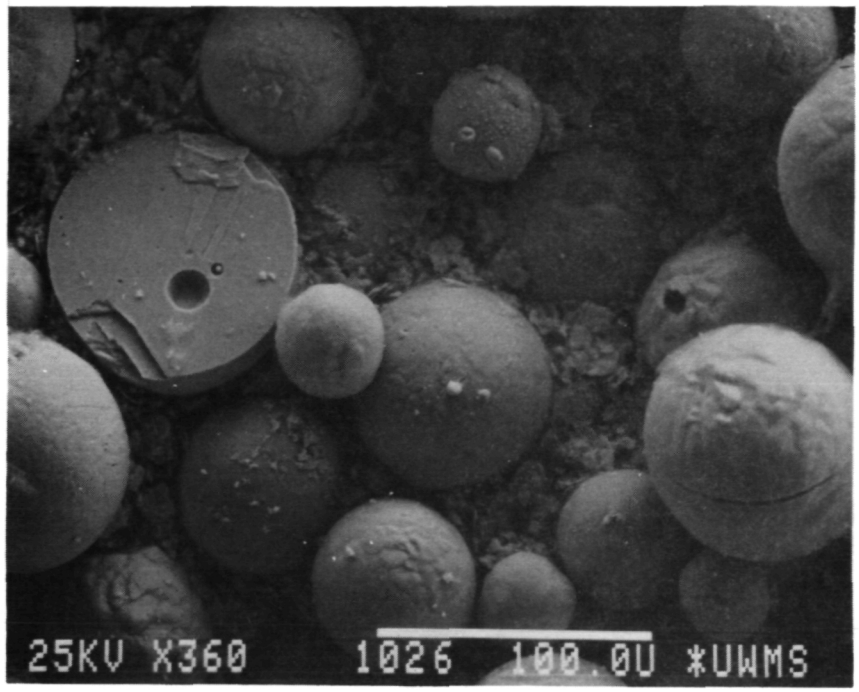

(a)

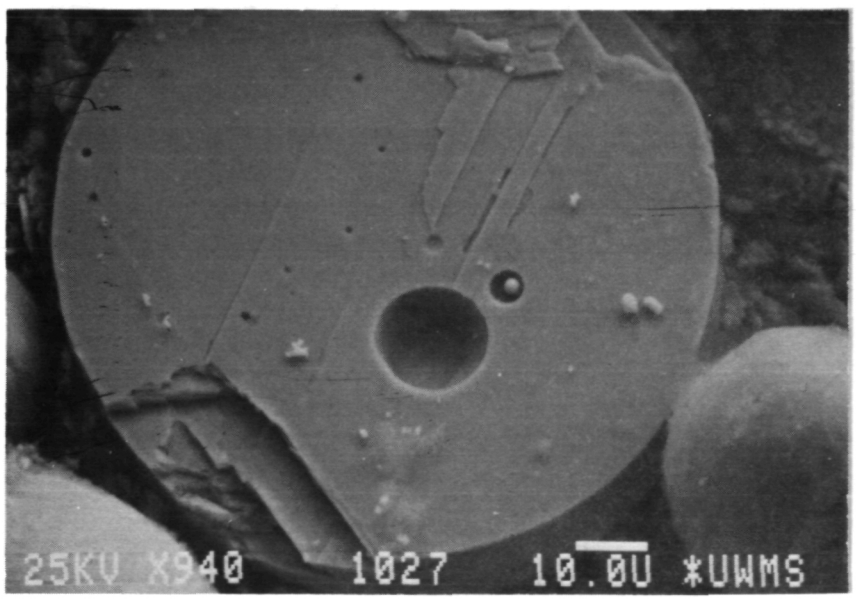

(b)

Figure 40. SEM micrograph of crushed Sb powder following drop tube processing. (a) 360X, (b) 940X

indicated which phase (s) were present in the material. While the diffraction peaks were defined well enough to be evaluated to approximately $\pm 0.2^{o}$, the complexity of the patterns required extensive analysis in order to select the proper phases. Candidate phases (with corresponding crystal structure data) were initially chosen for evaluation by considering both the starting components for emulsification (K_2SO_4, $ZnSO_4$ and Sb) and the alternative crystal structures for pure Sb. Also, the possibility of secondary reactions with both H_2O (during dissolution) and air had to be considered.

Following the conclusion of all pure Sb trials (both with crushed and emulsified powders) a comparison was made between each of the diffraction results. This revealed that each emulsified powder sample contained a similar set of phases independent of the type of processing treatment applied (however the volume fraction in each case was not identical). In a similar fashion, all crushed powder samples yielded diffraction patterns which were very similar to one another. Table IV provides a general summary of the d-spacings obtained for both types of droplet samples as well as the most probable phases which produced these patterns. For all emulsified samples the presence of $Zn(OH)_2$ was indicated

TABLE IV

X-Ray Data: Processed Sb

(d-spacings)

Emul. Sb	Crushed Sb	$Zn(OH)_2$ (s)	$ZnSb_2O_4$ (tet.)	Sb (rh.)	Sb (s.c.)
4.27			4.261 (200)		
3.75	3.71			3.753 (003)	
3.21		3.21 (020)	3.206 (211)		
3.09	3.08	3.11 (121)		3.109 (102)	
3.02		3.00 (123)	3.015 (220)		
2.97			2.964 (002)		
2.95					2.94 (100)
2.81		2.838 (222)			
2.79					
2.70			2.694 (310)		
2.46					
2.42		2.437 (511)			
2.24	2.23			2.248 (014)	
2.14	2.14			2.152 (110)	
2.01					2.09 (110)
1.95			1.9509 (411)		
1.90	1.87			1.878 (006)	
1.75			1.7552 (213)		
1.73			1.7296 (402)		
1.72					1.71 (111)
1.66			1.6625 (332)		
1.48					1.48 (200)
1.41	1.41			1.416 (116)	
1.33					1.33 (210)
1.26	1.26			1.261 (124)	
1.19					1.21 (211)

which seemed to originate as a precipitate from the dissolution of the carrier salt in water. This was consistent with the visual observation of a white powder which had limited solubility in H_2O following removal of the salt. In addition, the emulsified samples produced peaks which can be attributed to $ZnSb_2O_4$, a tetragonal oxide which may have been the observed thick coating encasing each of the Sb droplets. The numerous remaining peaks may be explained using both the rhombohedral and simple cubic forms of pure Sb, implying the existence of both phases in the processed powders. In all cases the crushed powder samples yielded diffraction patterns which could be adequately explained by the presence of the rhombohedral form of pure antimony. The oxide coating present on the crushed droplets however could not be detected due to its extremely small volume fraction in the sample.

In order to determine the relative stability of the simple cubic antimony phase, an emulsified powder sample, processed using DTA, was examined by x-ray diffraction both immediately after processing and following a 4 hour anneal at 540°C. Figure 41 presents a comparison of the x-ray results showing the strongest

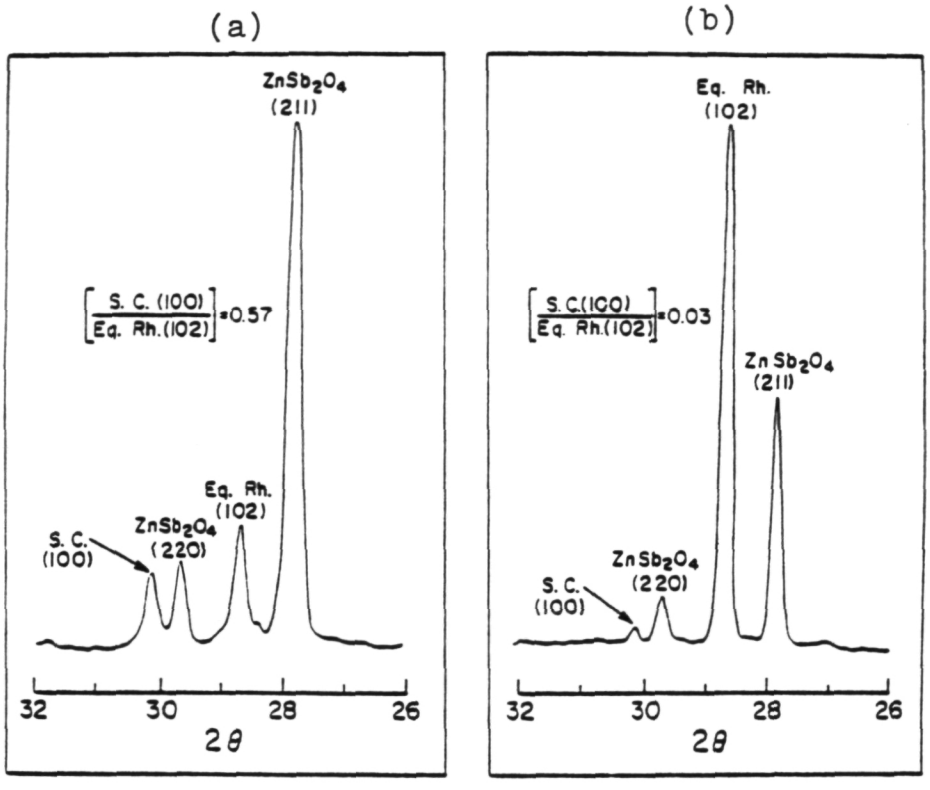

Figure 41. Comparison of the x-ray diffraction peak intensities for both the equilibrium rhombohedral and simple cubic phases of pure antimony: (a) immediately following DTA processing; (b) following a 4 hour anneal at 540°C.

peak for each antimony phase (the equilibrium rhombohedral (102) and the simple cubic (100)) both prior to, and following, the annealing treatment. The ratio of the strongest peaks are included as a qualitative comparison of the relative abundance of each phase. As can be seen by the change in this ratio, the annealing treatment has reduced the amount of the simple cubic phase from approximately 50% to approximately 3% that of the equilibrium rhombohedral phase. The slight decrease in the oxide peak intensities are due to vaporization of a small portion of the coating, the evidence of which (in the form of a deposited film) could be seen in the furnace following the annealing treatment.

Undercooling Behavior of Pure Indium Antimonide

a) Undercooling of Bulk InSb

In a manner similar to that of pure antimony, the second eutectic alloy constituent, indium antimonide (InSb), was examined initially in bulk form to determine its basic undercooling behavior. Upon initial heating of the bulk InSb a slight eutectic melting signal was detected indicating that the material composition was shifted slightly from the nominal 50/50 at.% line compound. Subsequent microstructural examination revealed

that the alloy had become slightly Sb rich. Due to the high purity of the original alloy (99.999% InSb) this compositional shift may be attributed to either the formation of a surface oxide layer which depleted the material of In causing a slight change in nominal composition or a deviation in the initial ingot composition. Figure 42 illustrates the undercooling behavior of bulk InSb as it is subjected to thermal cycling. The initial cycle produced a nucleation temperature of 451°C (ΔT = 80°C) however the undercooling degraded rapidly as the material was thermally cycled with subsequent nucleation temperatures being 482°C (ΔT = 49°C) and 489°C (ΔT = 42°C). Upon further cycling the undercooling level tended to stabilize at approximately 40-45°C.

In order to examine the effect of cooling rate on the undercooling of bulk InSb it was first necessary to stabilize the undercooling response such that the longer duration of the thermal cycle for the slower cooling rate would not significantly influence the reported values. Figure 43 presents the result of this variation in cooling rate, with nucleation occurring at 486°C for $\dot{T}$ = 20 °C/min. and 482°C for $\dot{T}$ = 80°C/min.

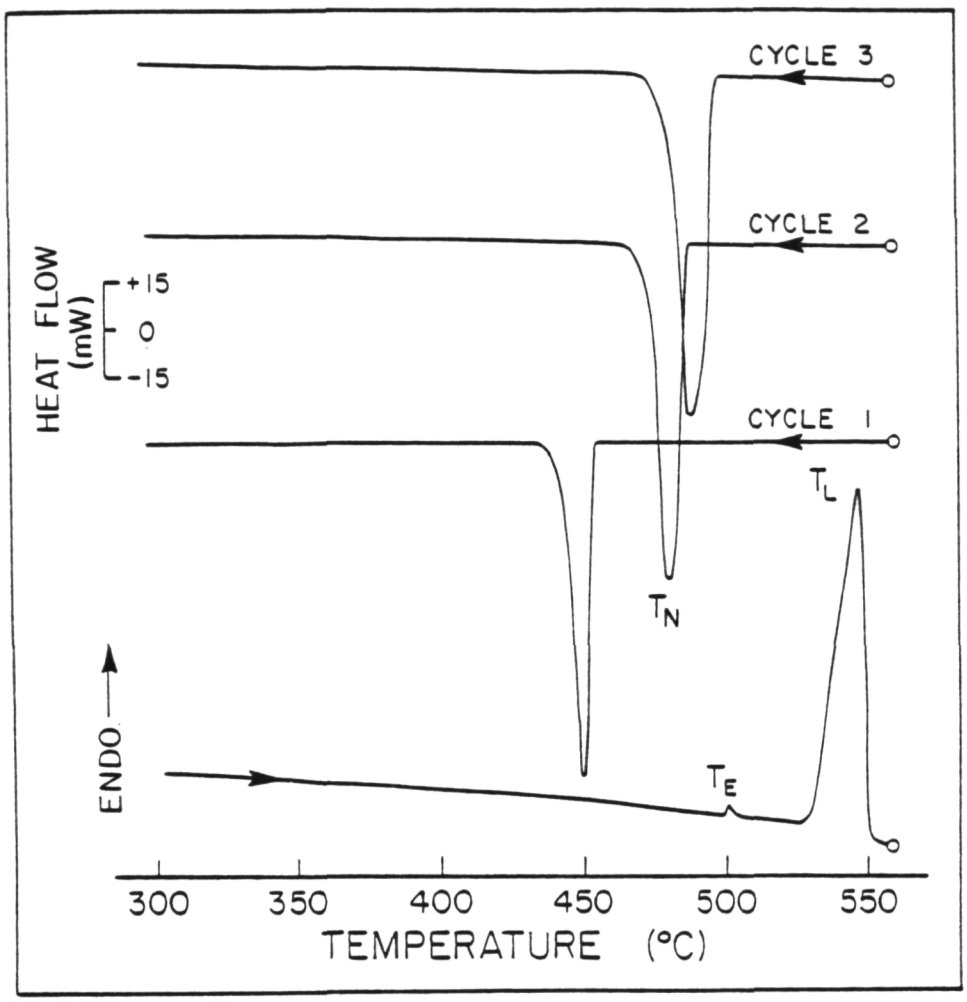

Figure 42. DSC thermogram showing the effect of thermal cycling on the undercooling behavior of bulk InSb ($\dot{T}$ = 80°C/min).

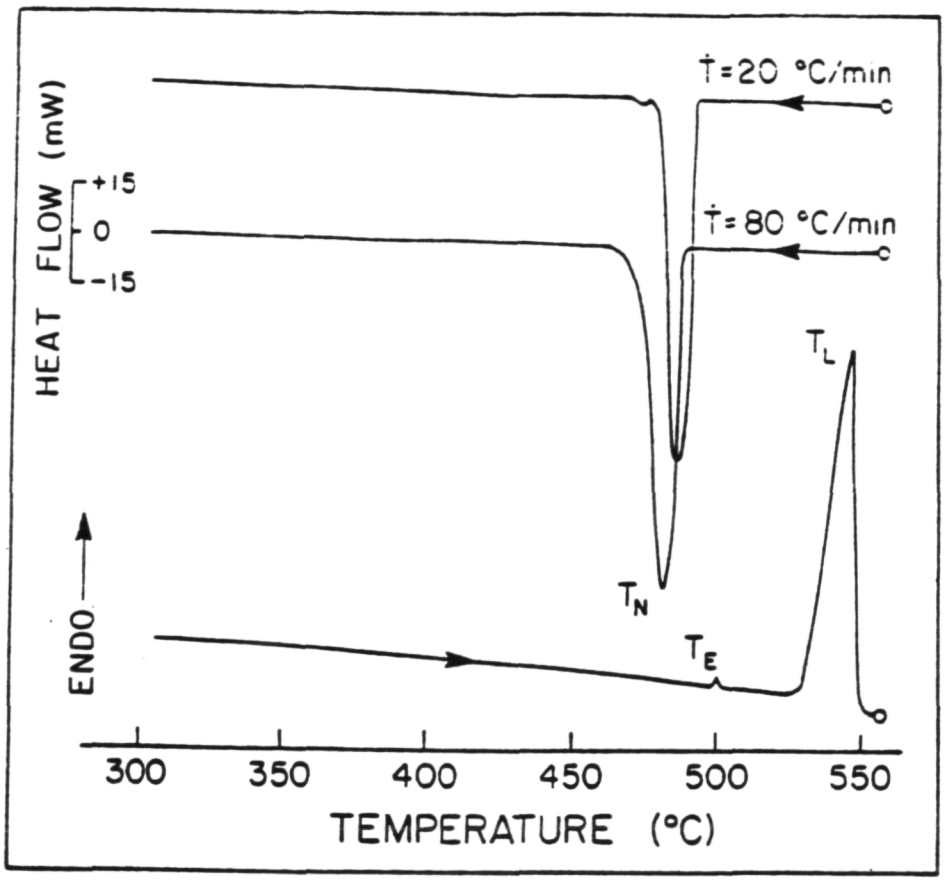

Figure 43. DSC thermogram showing the effect of cooling rate on the undercooling of bulk InSb.

b) Emulsification of InSb

Subdivision of the bulk alloy into droplet form was accomplished through the use of an emulsification treatment with a Li_2SO_4-K_2SO_4 carrier medium. The resulting powder was somewhat coarser than that of the pure Sb, however, it was possible to obtain sufficient droplet samples of size 20-30μm, 30-44μm, 44-63μm, 63-88 μm and 88-150μm for subsequent thermal processing. As with the bulk alloy, a slight depletion of In was detected following droplet formation which acted to shift the composition slightly to the Sb rich side of the phase diagram.

c) Size Effect on Undercooling

In order to examine the effect of droplet size on the undercooling behavior of InSb, samples were selected from each of the various size classes. Figure 44 presents the results of this portion of the study. Examination of the finest powder sample (20-30μm) reveals two major crystallization exotherms occurring at 392° (ΔT = 138°C) and 432°C (ΔT = 98°C). As the droplet size increases, the magnitude of the deepest undercooling peak decreases, becoming undetectable as the size reaches the 63-33μm class. The second crystallization exotherm

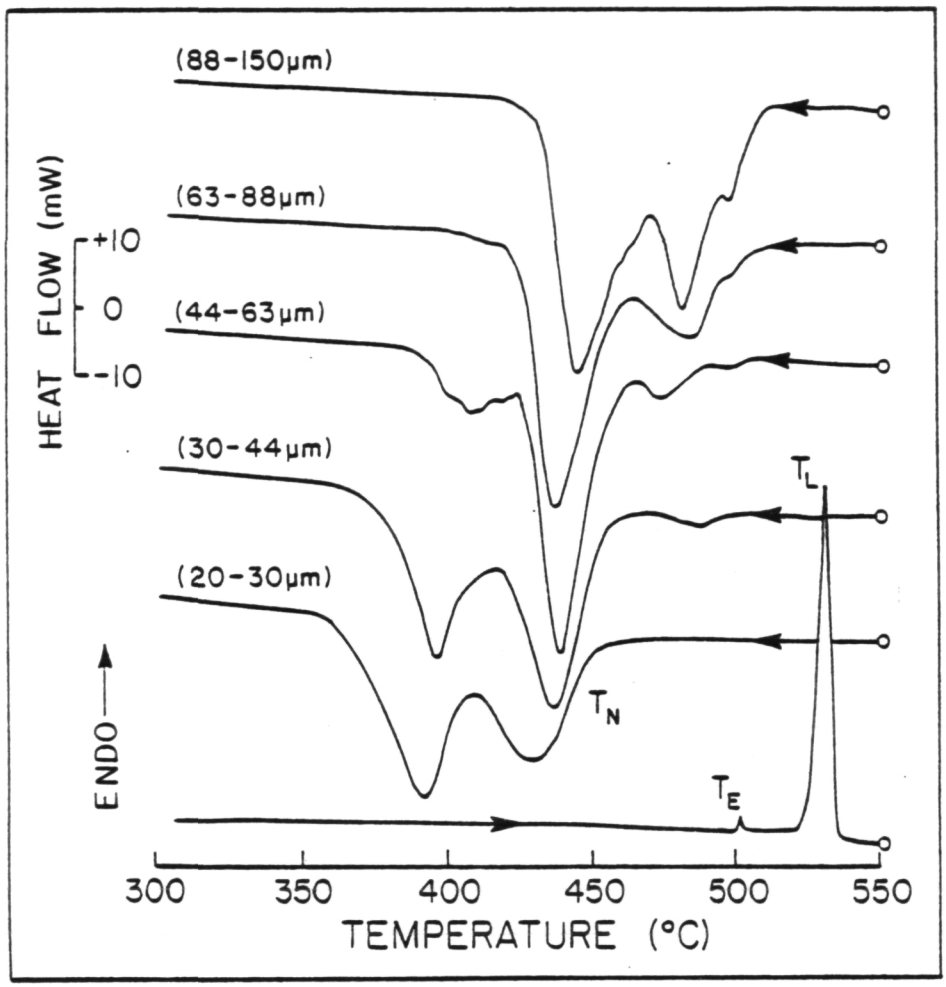

Figure 44. DSC thermogram illustrating the effect of droplet size on the undercooling of InSb.

($432^{o}C$) remains in each of the samples with the magnitude increasing as the droplet size becomes coarser. In addition, new exotherms at higher temperatures begin to appear as the droplet size increases. Thus, reducing the droplet size is apparently effective at isolating the more potent nucleants into a continually decreasing fraction of droplet population, allowing deeper levels of undercooling to be attained in the remainder of the droplet sample.

d) Cooling Rate Effect on Undercooling

In evaluating the effect of an alteration in cooling rate on the undercooling of InSb powder samples, droplets of 20-30μm and 44-63μm were chosen for cycling at $20^{o}C$/min. and $80^{o}C$/min., the results of which are presented in Figure 45. For the 20-30μm sample, increasing the cooling rate has two immediate effects: the nucleation temperatures are reduced as the cooling rate is increased ($T_{N1A} = 408^{o}C \rightarrow T_{N1B} = 392^{o}C$, $T_{N2A} = 434^{o}C \rightarrow T_{N2B} = 432^{o}C$); the relative magnitude of the deeper exotherm (i.e. the lower temperature nucleation peak) is increased as the cooling rate increases indicating that a larger fraction of the droplet population is becoming involved in this crystallization exotherm.

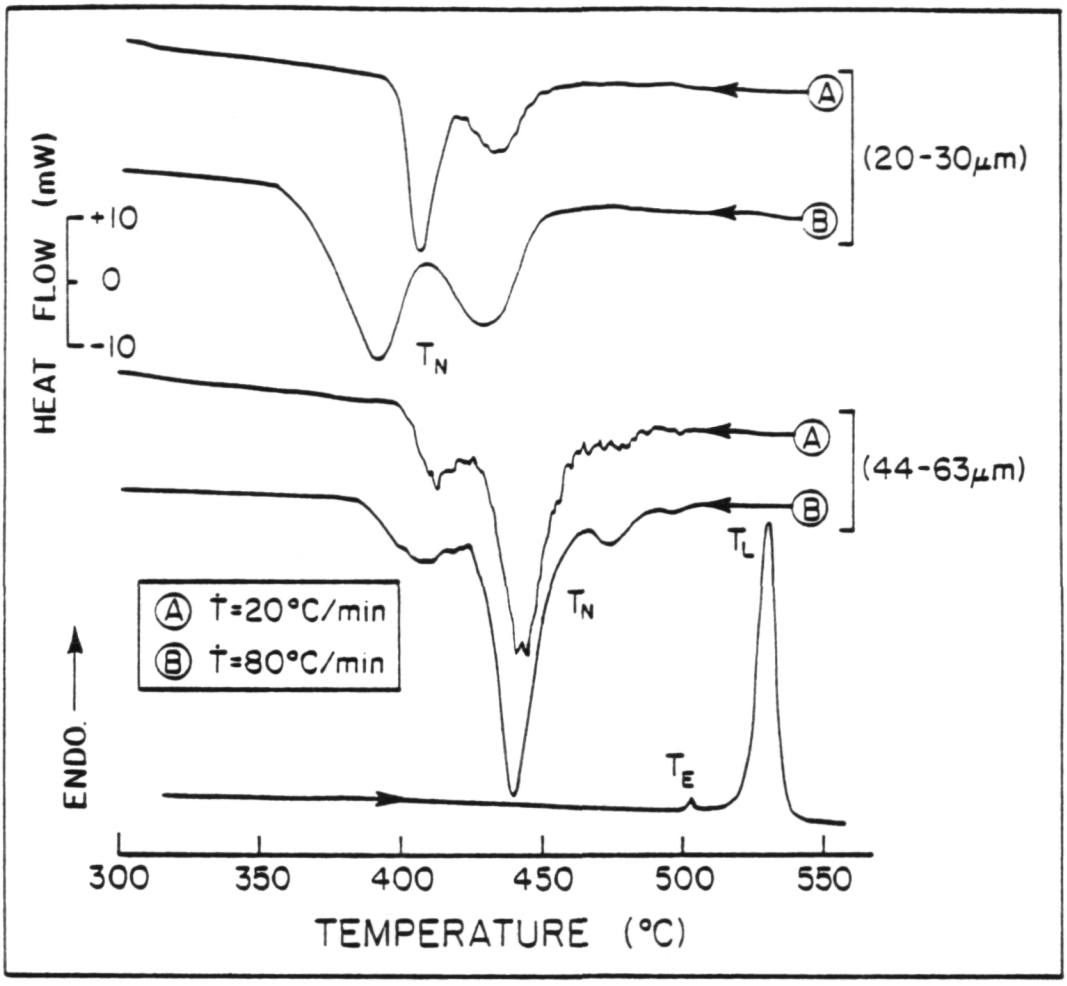

Figure 45. DSC thermogram illustrating the effect of cooling rate on the undercooling of InSb droplets.

The 44-63μm droplet sample shows only a slight (1-3°C) nucleation temperature dependence on cooling rate; however the crystallization behavior becomes somewhat more uniform as the cooling rate is increased.

e) Effect of Thermal Cycling on Undercooling

Due to the pronounced decay in undercooling with continued thermal cycling in bulk InSb it was of interest to evaluate the response of emulsified droplets to this cycling treatment. Figure 46 presents the results of this portion of the study for a 44-63μm InSb sample. The strongest exotherm (T_N = 440°C) shows a relative insensitivity to thermal cycling, however, droplets which undercool to a larger degree (T_N = 410°C) are adversely affected by this treatment, with this deeper exotherm being greatly diminished by the third thermal cycle. Thus, while there is a detrimental effect of cycling on the undercooling of emulsified InSb, it is much less severe than that encountered in the bulk alloy.

f) Effect of Droplet Coating on Undercooling

The single phase nature of the InSb compound allows crushing to be used as an alternative method of powder production by eliminating possible segregation effects which could create a variation in composition throughout

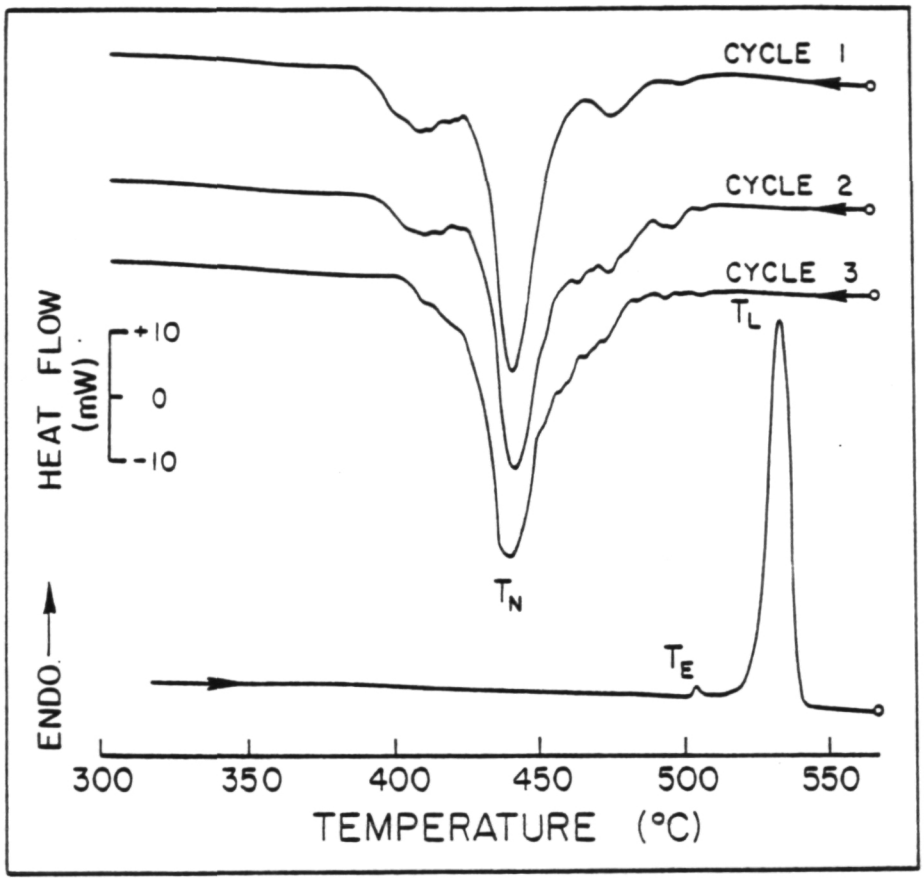

Figure 46. DSC thermogram showing the effect of thermal cycling on the undercooling behavior of InSb droplets (44-63μm).

the powder sample. Through this method droplets may be created with an alternate surface coating which can influence the undercooling response of the material. Figure 47 contrasts the undercooling behavior of crushed and emulsified powder samples of similar size during two consecutive cooling cycles. Comparing the first cooling cycles, the undercooling behavior is much more uniform for the emulsified powder than for the crushed sample with the former also yielding a significant exotherm at deeper levels of undercooling. The crushed sample (as in the bulk material) shows a large degradation in undercooling response upon application of a second cycle implying that a similar reaction to that seen in the bulk material has occurred. This effect is much less pronounced in the droplet sample produced through emulsification, presumably due to a protective coating introduced during emulsification.

g) Drop Tube Studies

Droplets produced through both emulsification and crushing techniques were processed in the laboratory scale drop tube with the resulting structure being compared to that produced using DSC. As with pure Sb, trial runs were carried out using crushed powder in

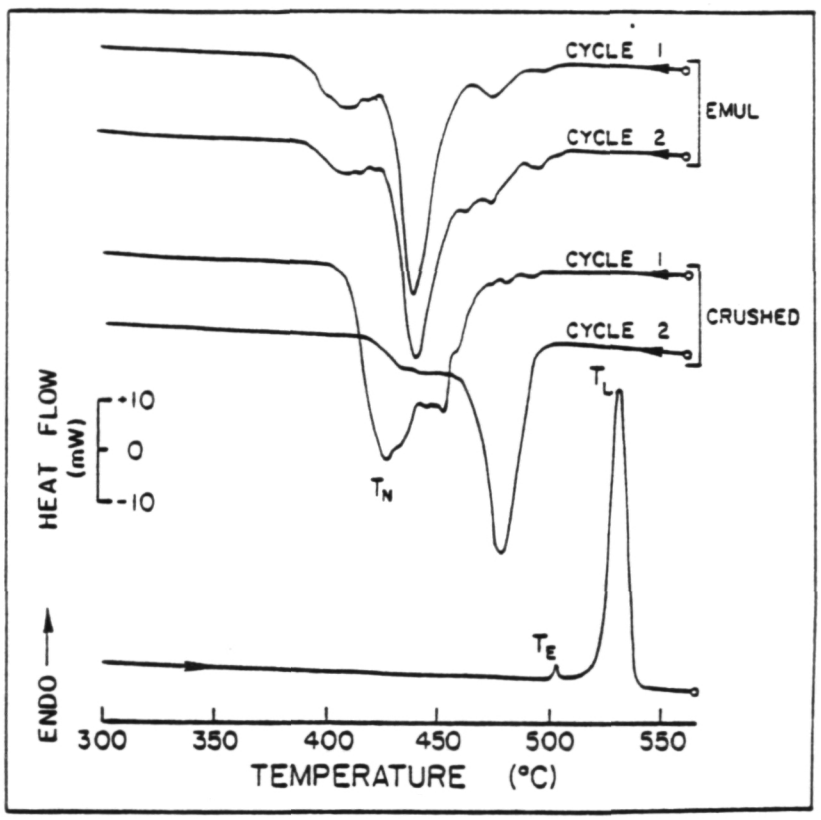

Figure 47. DSC thermogram illustrating the undercooling behavior during thermal cycling of both crushed and emulsified InSb droplets (44-63um).

order to determine the optimum power settings for sample processing. Following this procedure, -10μm crushed InSb and 20-30μm emulsified InSb samples were processed. In both cases the droplets spherodized during free fall indicating that both melting and solidification occurred during this period. Immediately following the sample processing, x-ray diffraction analysis was performed to detect possible metastable phase formation. As with all DSC InSb powder samples, the drop tube processed powder revealed no evidence of metastable phase formation in the structural analysis portion of the study.

Undercooling Behavior of an InSb-Sb Eutectic Alloy

Following evaluation of the undercooling and crystallization behavior of the pure constituents, Sb and InSb, examination of a eutectic mixture of these phases was carried out. Initially, certain factors which could influence the level of undercooling in the alloy were explored while the final stages of the study focused upon characterization of the resulting solidification microstructures.

a) Emulsification of the Eutectic Alloy

Subdivision of the eutectic alloy was accomplished through the use of a $LiSO_4$-K_2SO_4 carrier medium which readily produced droplets of size range: -20, 20-30, 30-44, 44-63, 63-88, and 88-150μm. Figure 48 presents exterior images of the as-emulsified alloy droplets. Examination of the droplets' surface reveals both the rough surface coating produced during emulsification as well as some scattered remnants of the carrier salt.

b) Effect of Thermal Cycling on Undercooling

Based upon the experience gained with pure InSb in which thermal cycling led to a rapid deterioration in undercooling, the initial parameter examined with the eutectic alloy was also the effect of thermal cycling on the undercooling behavior of droplet samples. With the eutectic powder, application of either numerous cycles at higher heating/cooling rates (80°C/min.) or fewer cycles at lower heating/cooling rates (20°C/min.) led to an increase in undercooling of the liquid. Figure 49 illustrates this behavior in a 20-30μm droplet sample. Thus, for the remainder of the study a "conditioning treatment" of two cycles at $\dot{T}$ = 20°C/min. was imposed to ensure consistency in the undercooling

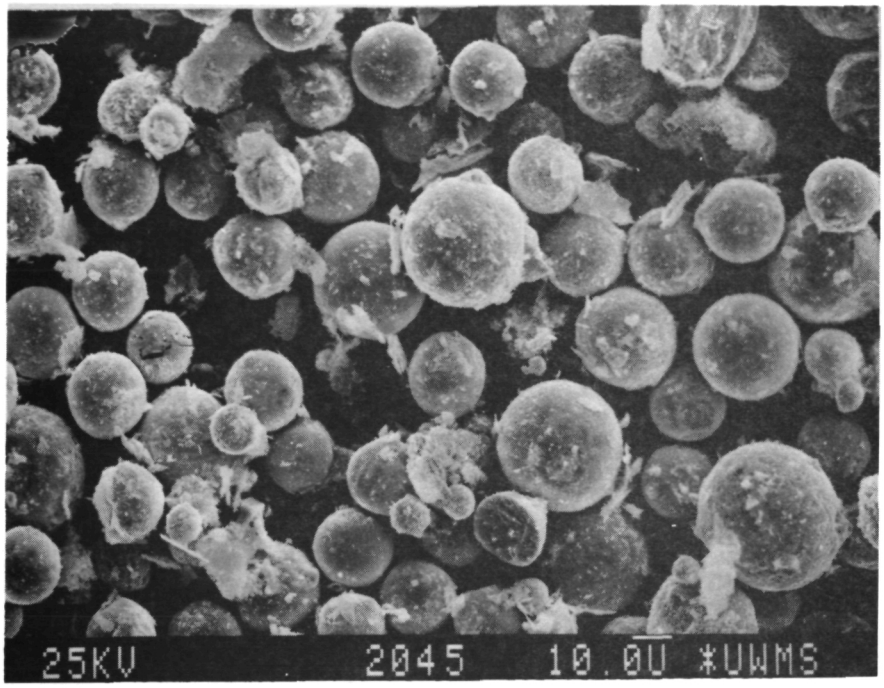

(a)

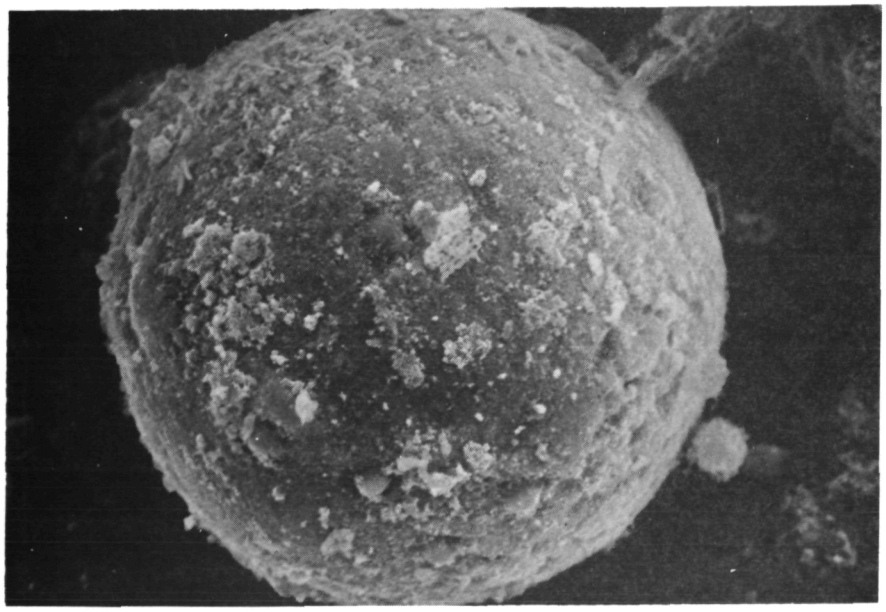

(b)

Figure 48. SEM micrographs showing the surface of as-emulsified eutectic alloy droplets. (a) 500X. (b) 4000X.

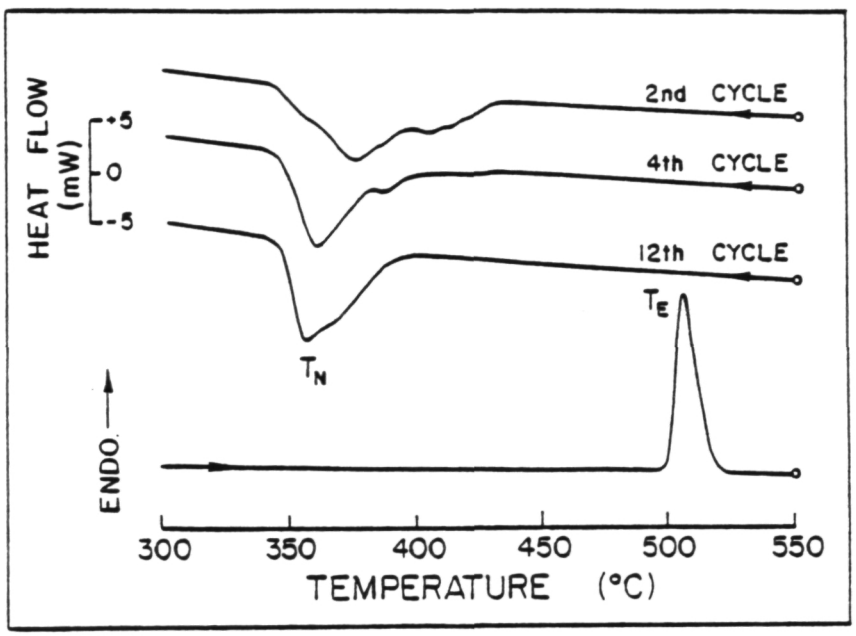

Figure 49. Illustration of the undercooling behavior of 20-30μm eutectic droplets during thermal cycling at $\dot{T}$ = 80°C/min.

values for comparative purposes.

c) Size Effect on Undercooling

Another factor which exerted significant influence on the undercooling behavior of both pure constituents was the droplet size. To investigate this parameter in the eutectic alloy, samples were selected from each of the available size categories for processing. Figure 50 presents the results for three of these samples indicating a significant increase in undercooling as the droplet size is reduced from 63-88μm (T_N = 411.8°C) to 30-44μm (T_N = 379.0°C) and finally to 20-30μm (T_N = 356.3°C).

d) Effect of Cooling Rate on Undercooling

An increase in cooling rate can result in the attainment of deeper undercoolings or possibly a shift from one nucleation site to another. As such, cooling rates of both 20°C/min. and 80°C/min. were imposed during the thermal cycling of each droplet sample. In addition, a quenching apparatus was used for processing a 30-44μm sample at a cooling rate of approximately 500°C/sec. Table V presents a summary of the undercooling data obtained with each processing technique for the range of eutectic droplet samples examined. In each case the

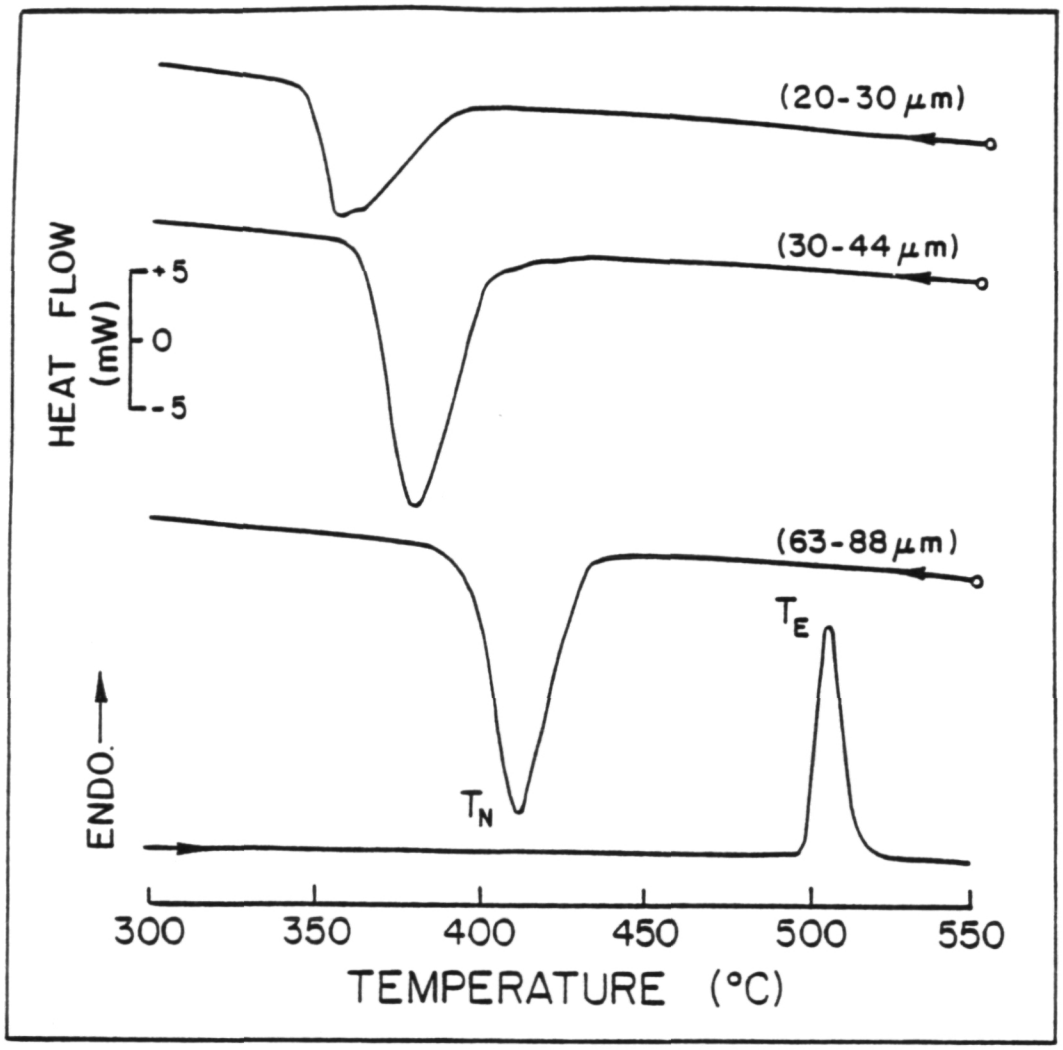

Figure 50. Illustration of the undercooling behavior for various droplet sizes at $\dot{T}$ = 80°C/min. Note: T_N is taken as the maximum in each exothermic peak.

TABLE V

Summary of undercooling data for eutectic droplet samples.

Droplet Size (μm)	Processing Method	Cooling Rate (°C/sec)	T_N (°C)	ΔT(°C)
-20	DSC	0.33	375.6	124.4
	DSC	1.33	371.8	128.2
20-30	DSC	0.33	371.3	129.0
	DSC	1.33	356.3	143.6
30-44	DSC	0.33	393.8	101.8
	DSC	1.33	379.0	121.8
	H_2O Quench	500	343	157
44-63	DSC	0.33	419.0	76.2
	DSC	1.33	409.1	91.5
63-88	DSC	0.33	421.8	71.4
	DSC	1.33	411.8	85.9

application of higher cooling rates increased the level of undercooling prior to nucleation. This increase was, in general, larger as the droplet size increased. For all samples processed using DSC, the final cycle used a cooling rate of 80°C/min. Thus, all subsequent microstructural characteristics reflected the level of undercooling obtained at this cooling rate.

e) Enthalpy of Melting Measurements

The use of DSC for thermal processing of samples allows the enthalpy of melting to be evaluated, providing an accurate sample weight has been obtained. This procedure was carried out for 30-44, 44-63, and 88-150μm eutectic droplet samples, the results of which are summarized in Table VI. The average value of ΔH_m is 182.2 J/g. A 99% confidence interval (C.I.), calculated using the expression (89):

$$C.I. = \bar{X} \pm t_{(n-1,\ \alpha/2)} \cdot s.e.(\bar{X}) \qquad (30)$$

where $\bar{X}$ is the average value, n is the number of data points, α is the confidence level (i.e. for a 99% interval $\alpha = 0.01$), t is a tabulated probability value of the Student t distribution, and s.e. ($\bar{X}$) is the standard error of measure (i.e. standard deviation divided by $\sqrt{n}$), provides a reasonable estimate of the error

TABLE VI

Enthalpy of melting values measured using DSC.

Droplet Size Range (μm)	Heating Rate (°C/min.)	ΔH_m (J/g)
30-44	20	181.4
	80	183.0
44-63	20	178.8
	80	179.5
88-150	20	184.9
	80	185.4

$$\Delta \bar{H}_m = 182.2 \text{ J/g}$$

99% Confidence Interval: $177.6 \text{J/g} \leq \Delta H_m \leq 186.7 \text{ J/g}$

associated with the measure of ΔH_m and is given by:

$$177.6 \text{ J/g} < \Delta H_m < 186.7 \text{ J/g}$$

These measured values of ΔH_m compare favorably with the value calculated from the pure components' thermodynamic data coupled with the assumption of constant heat capacities of the solid and liquid (equal to their values at the respective melting points) and modified according to the volume fraction of each phase in the alloy. This calculation results in a value of 186.4 J/g for the enthalpy of melting of the eutectic at 500°C.

f) Containerless Processing

Droplet samples of size range 20-30μm were thermally processed using the laboratory scale drop tube, with the solidification structures being compared to DSC and water-quenched samples. The heating coil power setting was selected by gradually reducing the level from that used for pure InSb until crushed powder no longer spherodized during free fall. A setting slightly above this was chosen in order to minimize the level of superheat in the specimens. Emulsified droplet samples were then processed both under a helium environment ($p_{He} \doteq 1$ atm) and under vacuum conditions. In both cases the processed powder was completely spherical

indicating that the droplets had solidified during the free fall period. Subsequent x-ray analysis revealed no metastable phase formation in either droplet sample.

g) Microstructural Characterization

As with other systems in which both eutectic phases tend to facet, the microstructure of the InSb-Sb eutectic is highly sensitive to the growth conditions present during solidification. Directional solidification studies (using positive thermal gradients) have indicated a rod morphology to be the stable growth form over only a limited range of moderate growth rates, beyond which a lamellar structure dominates (73); however, extension of this characterization to conditions in which growth occurs in an undercooled melt has not previously been undertaken. In addition, the extent and shape of the coupled growth region in this f./f. eutectic has not been well defined.

The use of emulsification and thermal processing techniques outlined thus far have allowed characterization of the solidification microstructures produced at various levels of undercooling to be carried out. The lack of solubility in the solid state helped minimize potential coarsening effects thereby assuring that the

observed microstructure was that produced during solidification. Figure 51 presents micrographs of the processed powder which are representative of those produced with each technique. Two distinct morphological regions may be observed, the first being a fine rod-type eutectic structure originating at the surface of the droplet and spreading inward as a hemispherical cap. This region is associated with the onset of nucleation and subsequent recalescence. At the end of this recalescence region a sharp morphological transition occurs after which the droplet is comprised of a lamellar-type eutectic structure. This region is associated with post-recalescence growth in which the external heat flow controls the rate of solidification. Figures 52, 53, and 54 present magnified images of both eutectic regions as well as the transition zone.

The existence of a well-defined normal-type eutectic microstructure implies that a significant degree of cooperation between the two phases occurred during growth. As such, the interphase spacing (λ) should accurately reflect the thermal history of the droplet during solidification. Thus, by measuring the finest rod spacings within each droplet (reflecting the spacing formed at the onset of solidification) a correlation

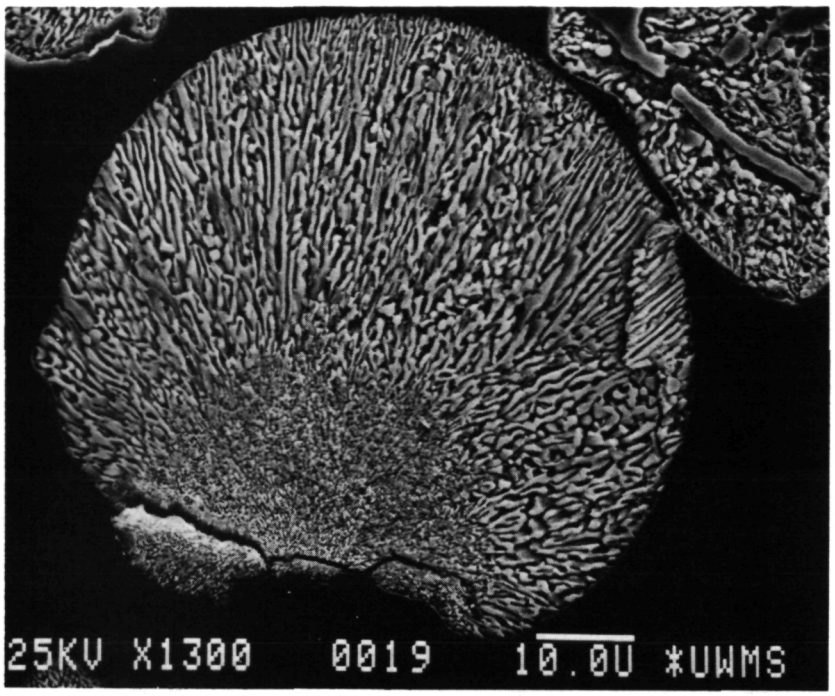

(a)

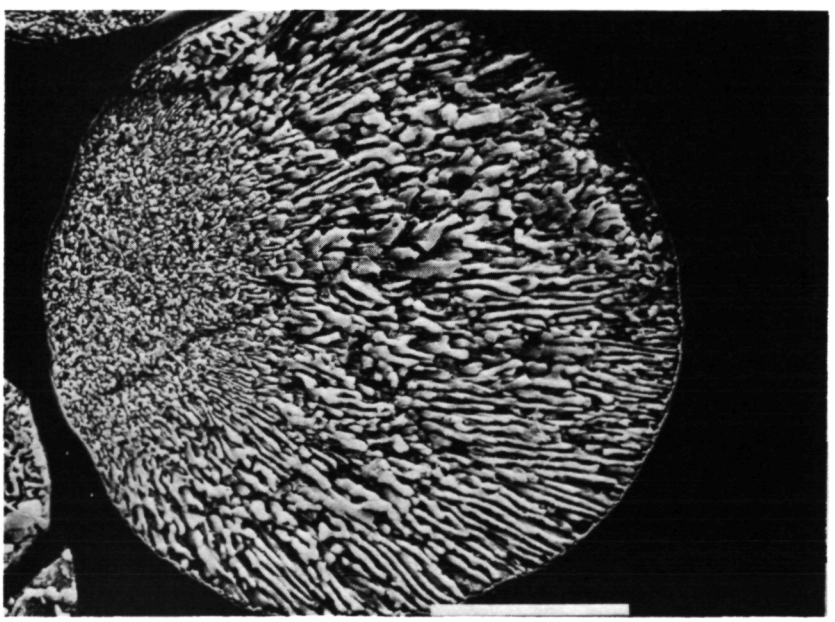

(b)

Figure 51. SEM micrographs showing the solidification structure following DSC processing. (a) 1300X. (b) 2600X.

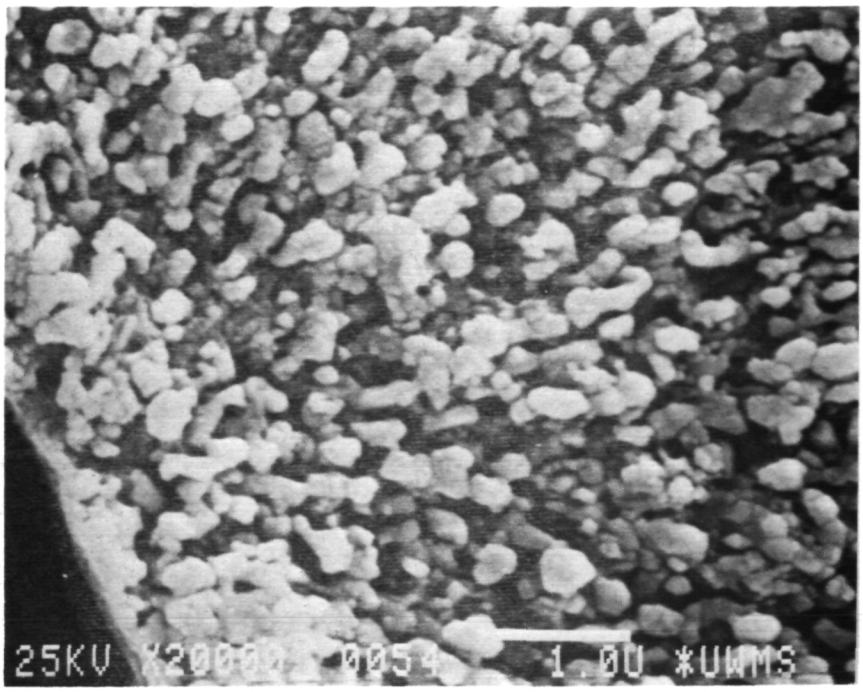

(a)

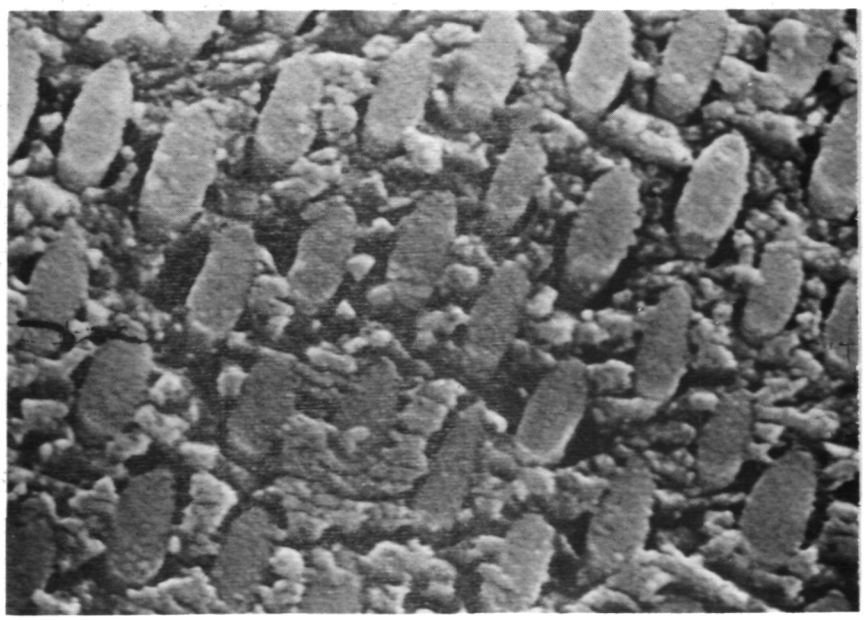

(b)

Figure 52. SEM micrographs illustrating the rod-type eutectic structure. (a) and (b) 20,000X.

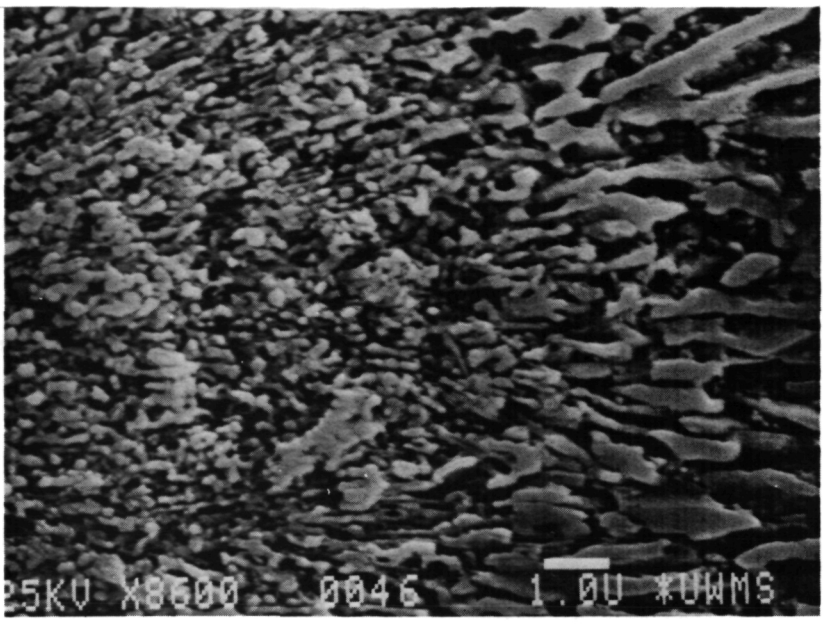

(a)

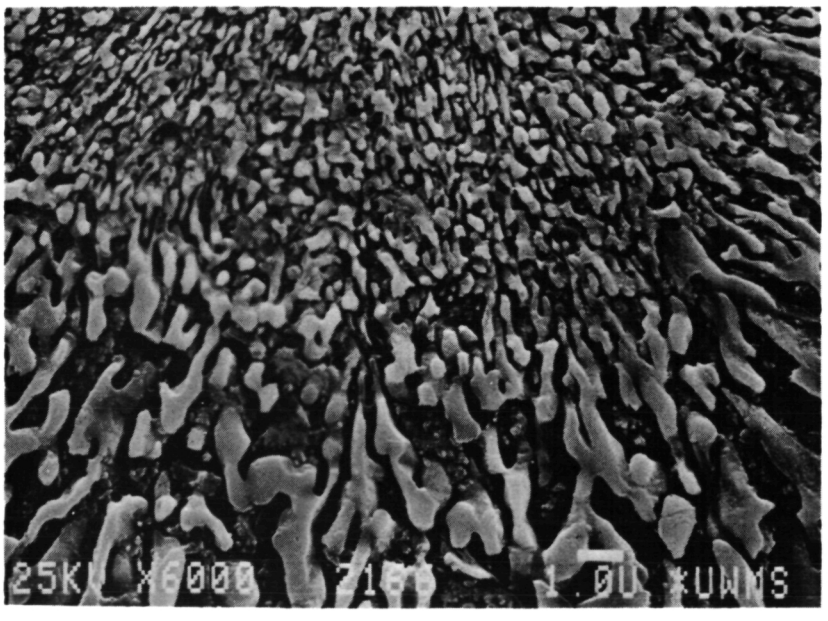

(b)

Figure 53. SEM micrographs illustrating the transition from a rod to lamellar morphology. (a) 8600X. (b) 6000X.

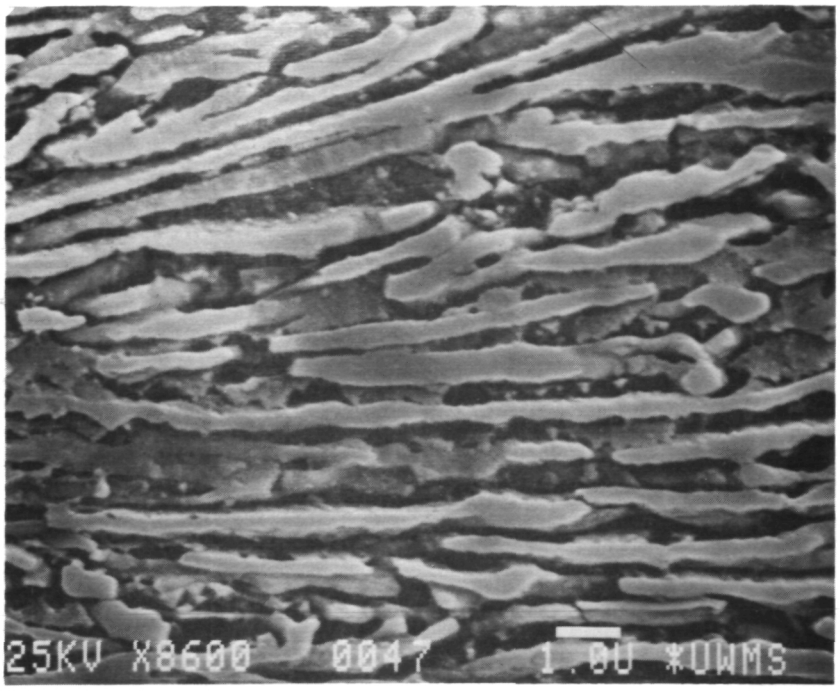

(a)

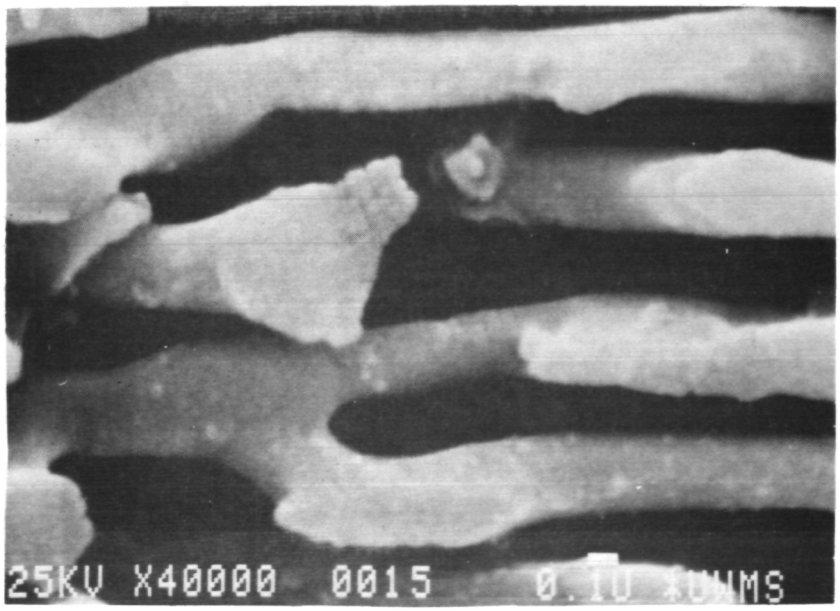

(b)

Figure 54. SEM micrographs illustrating the lamellar-type eutectic structure.
(a) 8600X. (b) 40,000X.

may be made between the level of undercooling obtained prior to the onset of solidification (ΔT_N) and the associated spacing produced by nucleation at this level of undercooling. In obtaining these rod spacing values, approximately 30 measurements were taken from each of 5-15 droplets randomly chosen from each sample. Typical magnifications required were 30,000X, however, for the finest spacings magnifications of 50-80,000X were used. Error bars were obtained through the formation of a 95% confidence interval for each data set (equation 30). Figure 55 presents the results of this correlation between λ and ΔT_N. In agreement with theory (81), the ln-values appear to be linearly related, with a least-squares fit of the data yielding the expression:

$$\ln\lambda(\text{Å}) = 14.94-1.56\ln \Delta T(^{o}C) \qquad (31)$$

Using this model, calculated undercooling values were obtained from the rod-spacings measured in samples processed in the drop tube (under both vacuum and helium conditions), the results of which are also shown in Figure 55. Thus, the eutectic spacing formed in the initial stage of solidification varies from 2750 Å to 930 Å as the undercooling is increased from 86°C (0.11 T_E) to 157°C (0.20T_E).

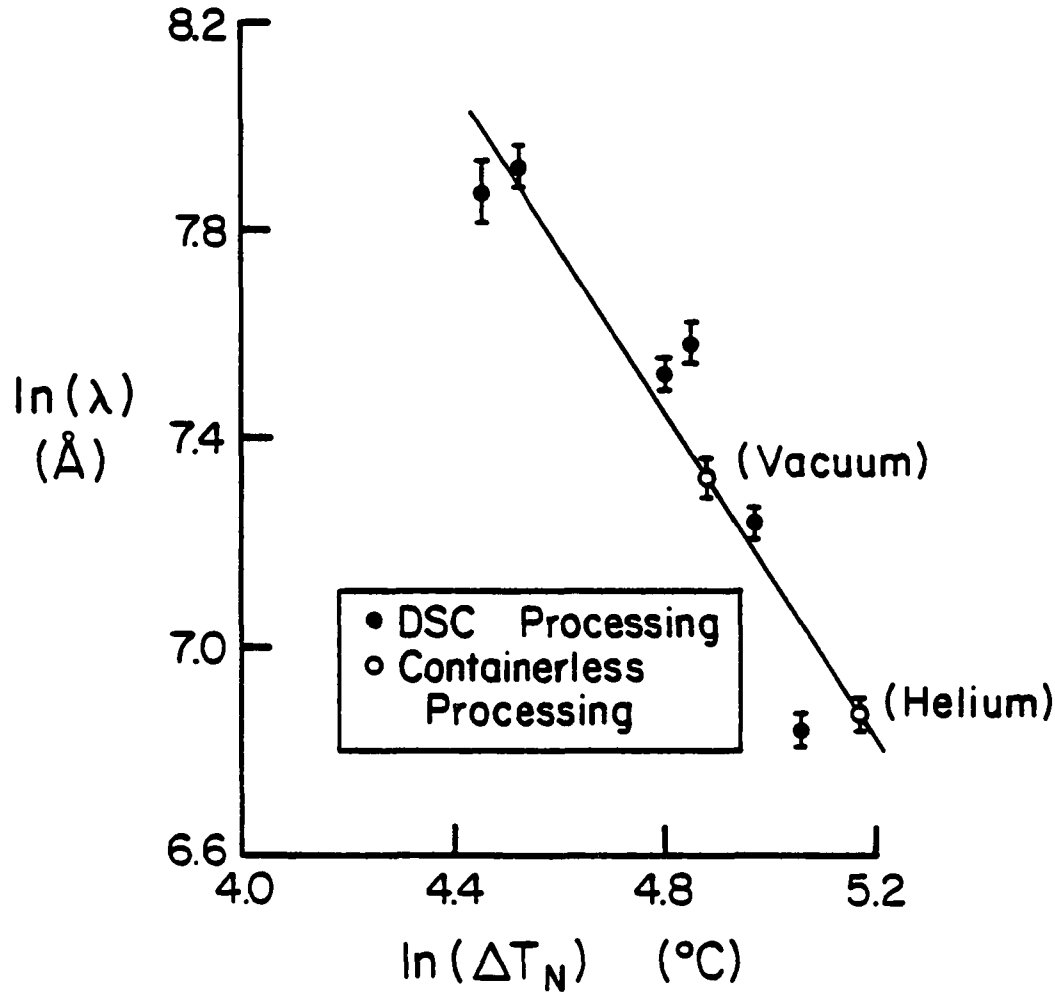

Figure 55. Initial interphase spacing as a function of nucleation undercooling for an InSb-Sb eutectic alloy.

Based upon previous data (83) obtained using directional solidification techniques (Figure 22) an expression relating rod spacing to solidification rate (R) was derived as:

$$\ln (R) = -4.16 - 2.09 \ln (\lambda) \qquad (32)$$

where λ units are μm and R units are cm/sec. Application of equation (32) to the current rod spacing measurements allows an estimation to be made of the growth rate at the onset of solidification, the results of which are presented in Figure 56. The finest spacing, 930 Å, represents a growth rate of approximately 2.2 cm/sec while the coarsest, 2750 Å, corresponds to a rate of 0.23 cm/sec. It is interesting to note that, although the solidification rates are based on an expression extrapolated over three orders of magnitude from its original data, the values obtained correspond favorably tothose obtained by Boettinger et al (79) in their study of rapidly solidified Ag-Cu eutectics.

By combining the data contained in Figures 55 and 56 it was possible to relate the onset solidification rate to the level of undercooling obtained in the sample, the results of which are presented in Figure 57. In this instance no estimation of experimental error is available (error in the measure of ΔT_N is assumed to be zero),

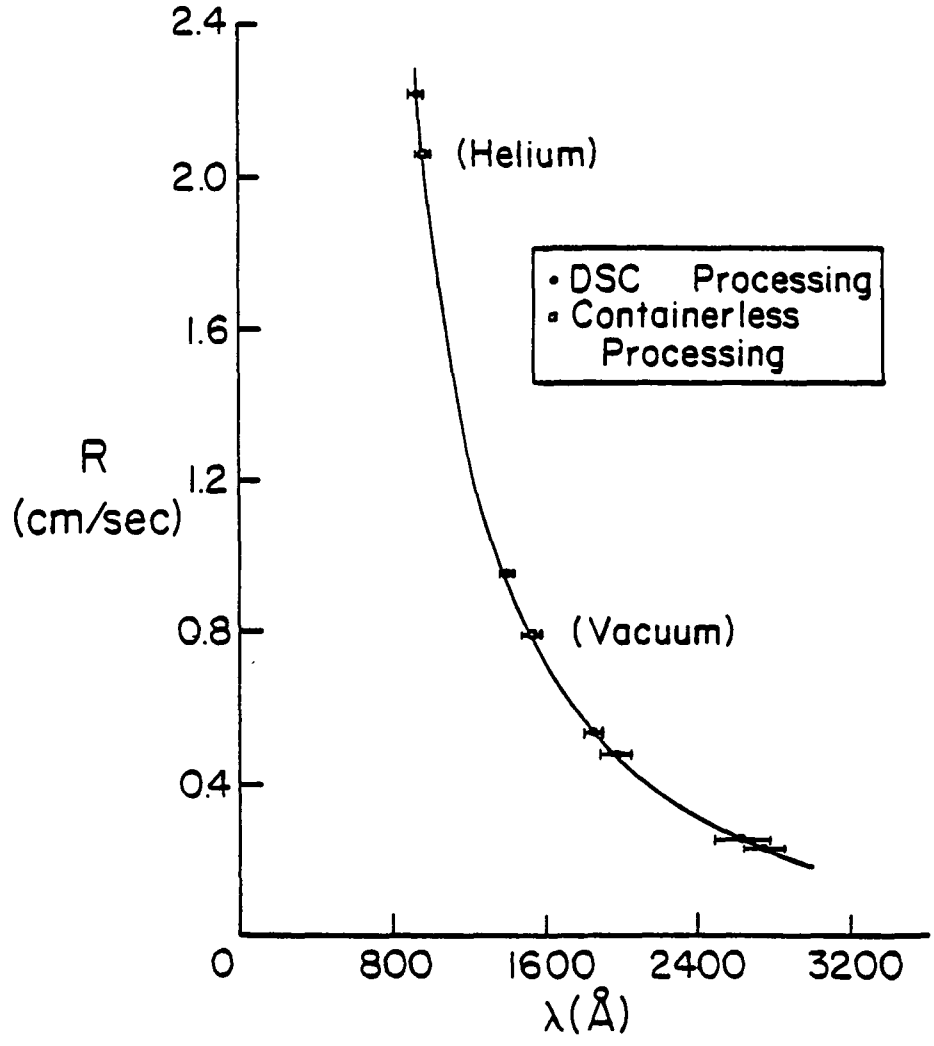

Figure 56. Onset solidification rate as a function of initial interphase spacing for an InSb-Sb eutectic alloy.

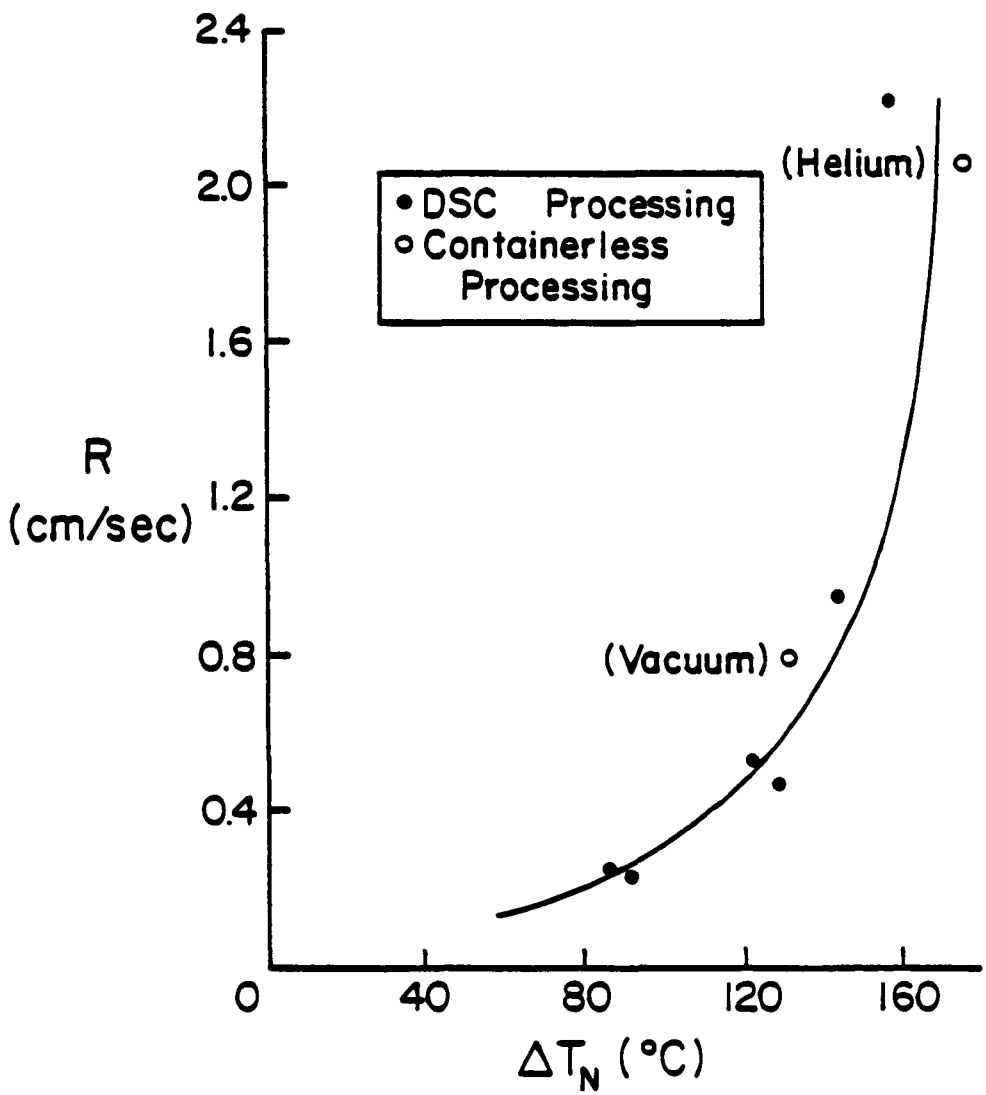

Figure 57. Onset solidification rate as a function of nucleation undercooling for an InSb-Sb eutectic alloy.

however a parabolic relationship is predicted between R and ΔT_N which once again is in agreement with eutectic growth theory (81).

Following the onset of solidification in an undercooled droplet, the release of latent heat acts to lessen the degree of undercooling and thus reduce the growth rate of the advancing interface. This change in conditions within the droplet is reflected in the interphase spacing and, as such, may be detected through precise measurement of rod spacing as a function of interface position during solidification. In order to carry out such measurements the region of finest rod spacing was assumed to represent the nucleation region (in all cases this area was adjacent to the droplet surface). Starting at this point, successive arcs were struck at fixed intervals from the origin (i.e. nucleation area) until the entire recalescence region had been spanned. The distance of each arc from the origin could then be translated into fraction solidified (g) (assuming the solid grows as a hemispherical cap) through the expression (90):

$$g = 0.5(1 + Z)^3 - 0.1875(1 + Z)^4 \quad (33)$$

where (1 + Z) is the (dimensionless) distance measured along the growth axis. Rod spacings were then measured

from which an average value could be extracted for each arc. Using this technique, data relating rod spacing to fraction solidified during recalescence was obtained for droplets of size 20-30, 30-44, 44-63 and 63-88μm, a composite plot of which is presented in Figure 58. In each case the spacing increases as recalescence proceeds, however both the rate at which this occurs and the ultimate extent of the spacing increase varies for each droplet size. In general, both the rate of increase and ultimate rod-spacing become larger as the droplet size increases (and the corresponding undercooling decreases). Additionally, for any given droplet size, the rate of increase in rod spacing continually declines following the onset of solidification until ultimately the spacing approaches a constant value near the end of recalescence.

Through the use of equation (32), the spacings shown in Figure 58 may be translated into corresponding solidification rates. Figure 59 presents this relationship between solidification rate and fraction solid for each of the droplet sizes. As recalescence proceeds there is a continual decay in the growth rate, however, as the droplet size is reduced, the extent to which this decay occurs is lessened.

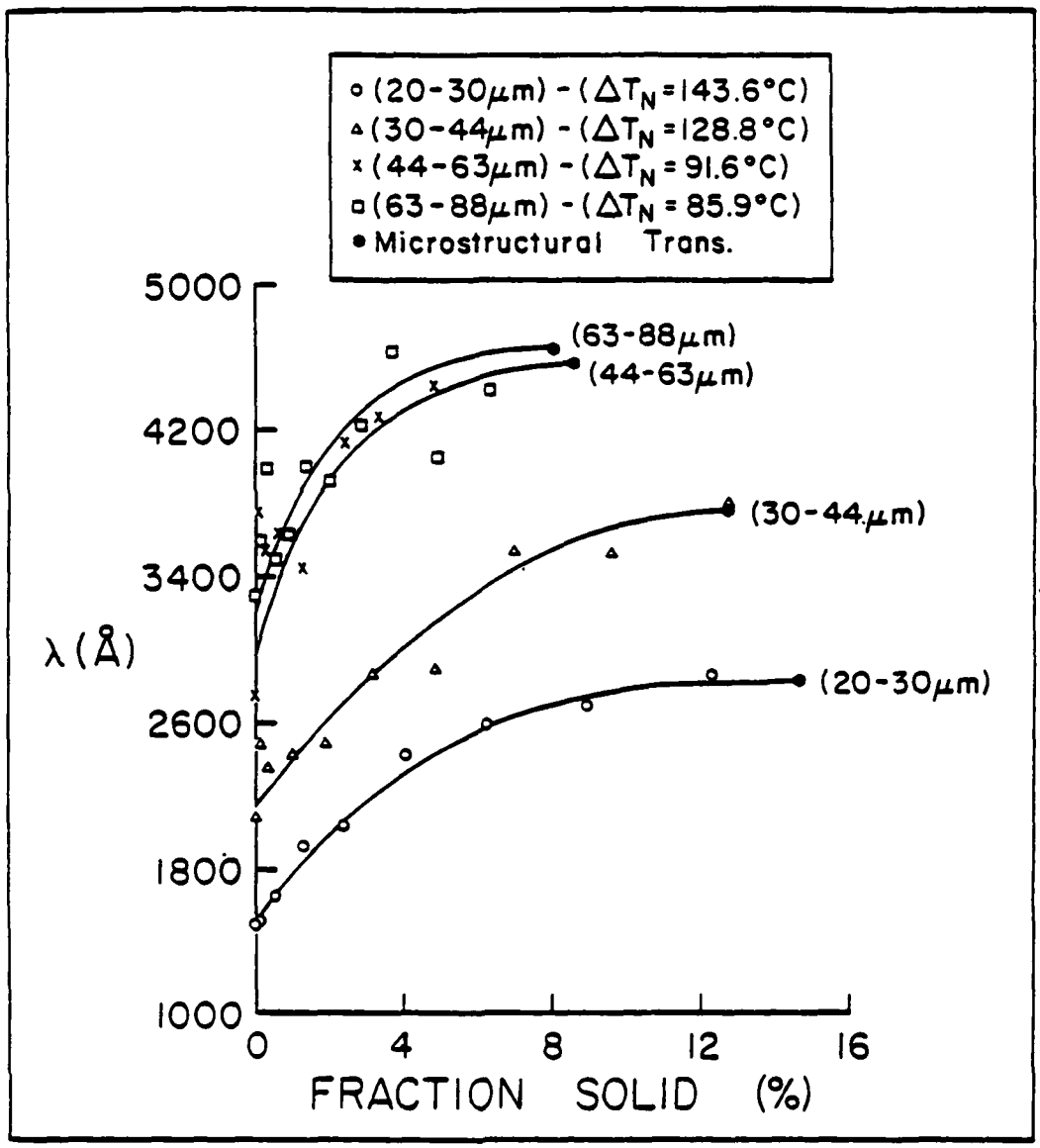

Figure 58. Interphase spacing as a function of fraction solidified (during recalescence) for InSb-Sb eutectic droplet samples.

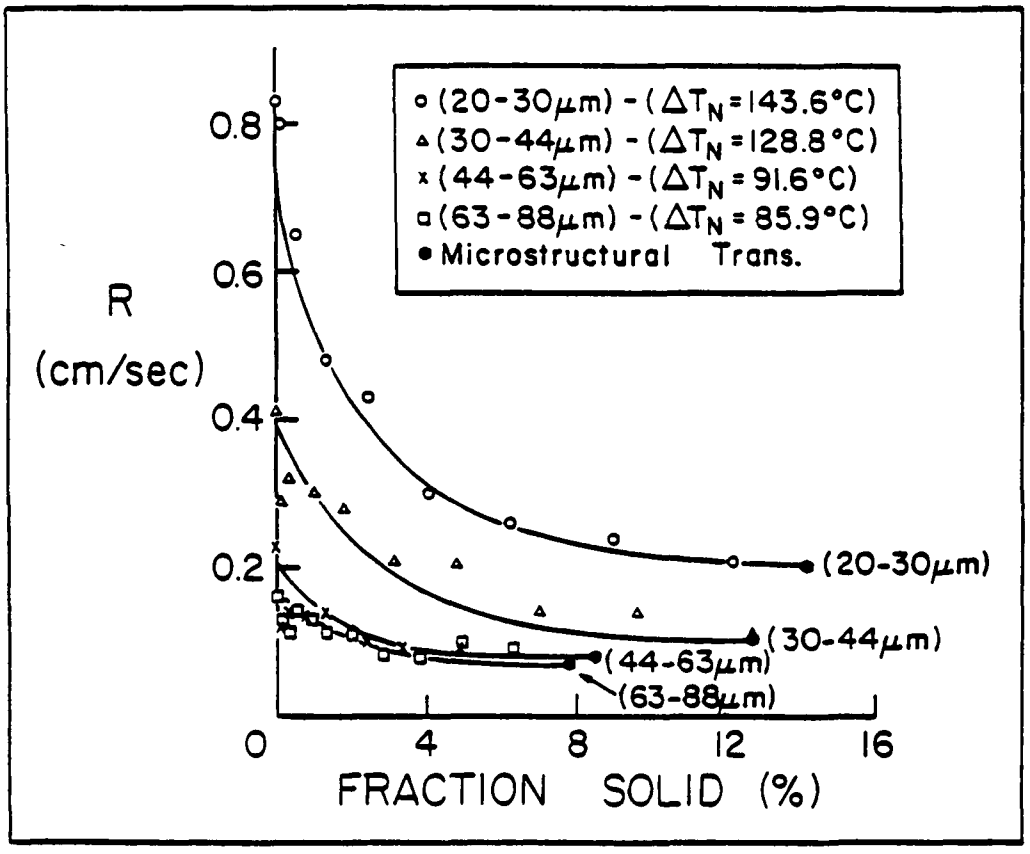

Figure 59. Interface velocity as a function of fraction solidified (during recalescence) for InSb-Sb eutectic droplet samples.

In an attempt to examine the undercooling variation during recalescence of the droplets, the linear expression relating undercooling to initial rod spacing (equation (31)) was used. The results of this calculation are illustrated in Figure 60 for each of the droplet samples. As recalescence proceeds the release of latent heat acts to decrease the level of undercooling seen by the droplet. A caution must be made however in the interpretation of this figure, in that the undercooling values now correspond to those experienced at the interface, not necessarily those seen throughout the liquid. Under certain conditions these values may differ substantially from one another (90).

Thus, the occurrence of a normal-type eutectic microstructure in the InSb-Sb alloy system has allowed a quantitative correlation to be made between the level of undercooling prior to nucleation and the interphase spacing of the eutectic structure. This data, combined with a rate relationship, has provided insight into the conditions experienced during the cooperative growth of a eutectic into an undercooled melt. An extension of this approach also allows a reasonable estimate to be made of the level of undercooling obtained during containerless processing of the eutectic powders.

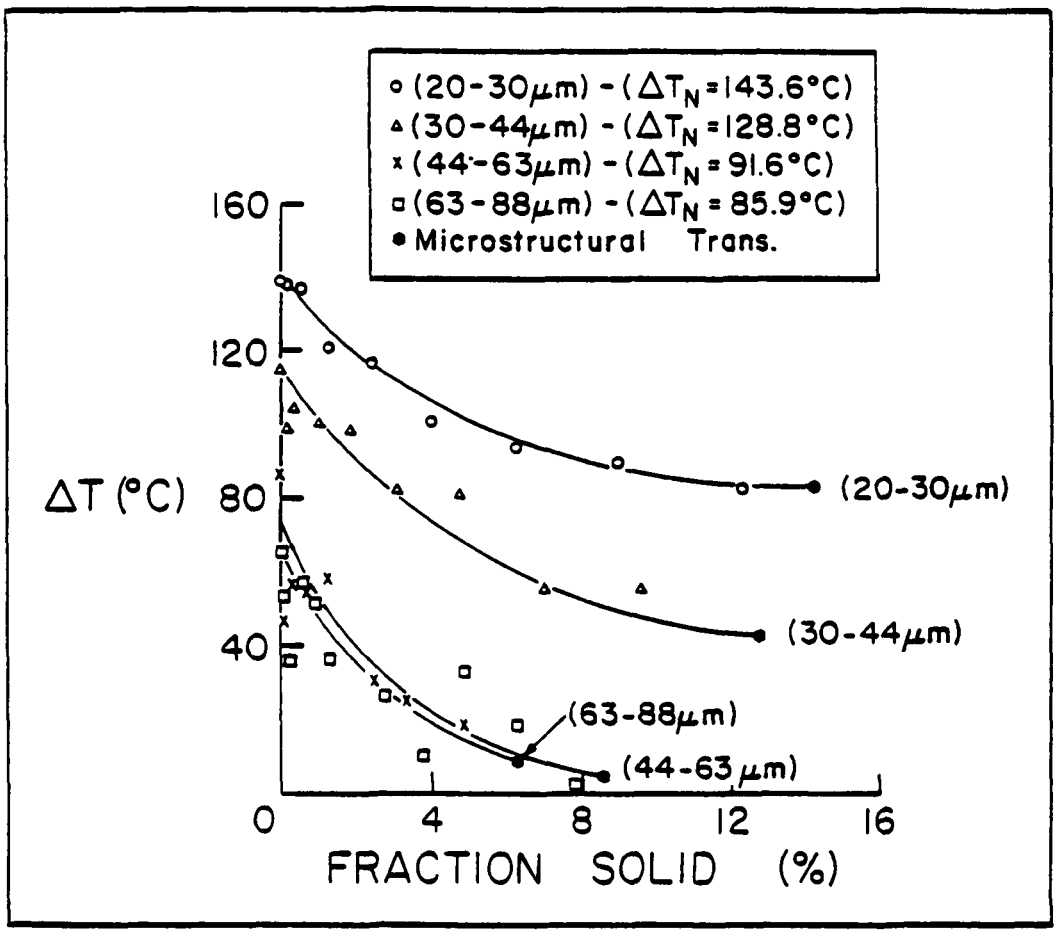

Figure 60. Estimated interfacial undercooling as a function of fraction solidified (during recalescence) for InSb-Sb eutectic droplet samples.

DISCUSSION

Pure Antimony

Use of the droplet emulsion technique has been successful in not only extending the maximum undercooling of pure Sb from $0.08T_m$ to $0.23T_m$ but also in providing conditions under which nucleation kinetics favorable to the formation of a metastable simple cubic structure can operate. The subsequent discussion focuses initially on the factors which influence undercooling in the liquid which is followed by examination of metastable phase formation aspects of the material.

a) Undercooling Characteristics

A number of processing parameters have been identified which influence the optimization of undercooling in pure Sb. Of primary importance is the degree of size refinement in the sample. As with all materials, bulk Sb contains a variety of internal nucleants which inhibit the attainment of large undercoolings. Application of simple crushing techniques yield powder which exhibit greatly enhanced undercooling ($0.18T_m$) while retaining an oxide coating identical to that of the bulk Sb. This suggests that the bulk undercooling is limited by either the influence of isolated internal

catalysts or a catalyst/coating interaction effect. By dispersing the more catalytic sites into a small fraction of droplets, other less potent nucleants are allowed to operate at deeper levels of undercooling.

Application of the droplet emulsion technique retains the nucleant isolation advantage. In addition it produces a surface coating which is less catalytic in nature thereby encouraging the attainment of even greater levels of undercooling ($0.23T_m$). The emulsified samples exhibit a less uniform crystallization behavior which may be attributed to both the thickness of the surface coating (creating a wider size distribution than implied by outer diameter measurements) and possibly to a variation of surface coating characteristics within each droplet sample (similar to that observed in pure In droplet emulsions (91)).

The cooling rate applied to a sample can greatly influence the level of undercooling prior to nucleation. For emulsified Sb droplets an increase of 10^2 in cooling rate (10^{-1} to 10^1 ^oC/sec) produced little change in undercooling, however a further increase to 500^oC/sec was accompanied by a substantial increase in undercooling ($0.14 \rightarrow 0.23T_m$). This implies that the heterogeneous nucleation site operating at the slower cooling rates

was kinetically "bypassed" by increasing the cooling rate to a level at which the corresponding T-T-T curve was no longer intersected and thus a site of lesser potency was allowed to operate at a deeper level of undercooling.

Of lesser influence in controlling the undercooling was the level of applied superheat and initial purity of the melt. The slight deviations experienced as the level of superheat was increased may have arisen due to a number of reasons including alterations in the catalytic potency of either the surface coating or internal catalytic sites. The reversibility of these superheat effects implies that the change is, however, not a permanent modification. The purity effect, while smaller in magnitude, was fairly well defined. Increasing the level of purity alters the nucleant distribution in the parent ingot. This reduction in initial internal sites is apparently effective at both slightly increasing the undercooling of emulsified droplets and at creating a more uniform crystallization behavior in the sample. This implies that elimination of certain internal impurities allows the undercooling of each droplet size range to be controlled by fewer (or possibly single) catalytic sites.

b) Metastable Phase Formation

1) Analysis of Previously Reported Results

Previous investigations (47,58) using splat-quenching techniques and subsequent TEM analysis have reported the production of numerous metastable Sb structures including hcp, simple cubic (s.c.), fcc, "new" rhombohedral and tetragonal phases. Using the reported lattice parameter values for each phase it is possible to calculate molar volumes and rank the phases according to increasing density. Table VII presents a summary of the volume data and indicates that:

$$\rho_{fcc} > \rho_{s.c.} > \rho_{tet} > \rho_{hcp} > \rho_{new\ rh.} > \rho_{eq.rh.}$$

Examining the temperature-pressure (T-P) diagram for pure Sb (Figure 15) we see that:

$$\rho_{Sb_{III}} > \rho_{Sb_{II}} > \rho_{Sb_{I}}$$

where Sb_I is the equilibrium rhombohedral phase, Sb_{II} is a simple cubic phase, and Sb_{III} is of an undetermined crystal structure. Based upon a comparison of the above rankings, the Sb_{III} phase would have to be fcc, a result as yet unsubstantiated in any of the numerous high-pressure studies conducted with pure Sb. Additional data concerning the heats of transformation (ΔH_t) have been reported (Figure 16) and may be used to calculate

TABLE VII

Volume data for metastable Sb based on experimentally determined lattice constants (58).

Crystal Structure	Molar Volume (m^3/mole)
tetragonal	2.71×10^{-5}
simple cubic	1.90×10^{-5}
fcc	1.47×10^{-5}
hcp	3.02×10^{-5}
"new" rhombohedral	3.04×10^{-5}
eq. rhombohedral	3.62×10^{-5}

a slope for the phase boundaries of both the $Sb_I \rightarrow Sb_{II}$ and $Sb_{II} \rightarrow Sb_{III}$ (assuming Sb_{III} is fcc) phase transformations. As a first approximation an assumption is made that the ΔH values are independent of temperature (i.e. $\Delta C_p = 0$); the Clausius-Clapyron equation is then employed in the form:

$$(dT/dP)_{eq} = T_{eq}\Delta V/\Delta H_t$$

where T_{eq} is the equilibrium transformation temperature (obtained by extrapolation of the true T-P phase boundaries to one atmosphere pressure) and ΔV and ΔH_t are the volume and heat of transformation respectively. Using this approach the slope of the boundary between the rhombohedral and s.c. phase has a calculated value of -81 ^oC/kbar. This value is over six times greater than could be expected from the equilibrium T-P diagram. Similarly the s.c./fcc boundary calculation results in a slope of -44^oC/kbar, once again over twice the expected value.

An additional calculation can be made which provides an approximate value of the melting point for each metastable constituent, although in this case also no ΔC_p correction is possible. At the melting temperature of the metastable phase the following equation applies:

$$\Delta G_{S\rightarrow L} = \Delta H_f' - T_m' \Delta S_f' = 0$$

where $\Delta H_f'$ and $\Delta S_f'$ are the heat and entropy of fusion for the metastable phase respectively and T_m' is the metastable phase melting point. Assuming that $\Delta S_f'$ is approximately equal to ΔS_f (equilibrium phase entropy of fusion) and that $\Delta H_f'$ may be approximated by $(\Delta H_f - \Delta H_t)$, where ΔH_f is the latent heat of fusion for the equilibrium phase, the free energy change may be expressed as:

$$\Delta G_{S\rightarrow L} = (\Delta H_f - \Delta H_t) - T_m' \Delta S_f = 0$$

or

$$T_m' = (\Delta H_f - \Delta H_t)/\Delta S_f$$

Replacing ΔS_f with $\Delta H_f/T_m$ (where T_m is the melting point of the equilibrium phase) we obtain:

$$T_m' = (\Delta H_f - \Delta H_t)/\Delta H_f \cdot T_m$$

Using values of $\Delta H_f = 4.75$ kcal/mole and $T_m = 631^{\circ}C$ combined with the reported ΔH_t values, calculated metastable melting points are obtained as: $T'_{m(tet)} = 250^{\circ}C$, $T'_{m(s.c.)} = 177^{\circ}C$, $T'_{m(fcc)} = 406^{\circ}C$, $T'_{m(hcp)} = 562^{\circ}C$, $T'_{m(new\ rh.)} = 401^{\circ}C$. A comparison with the reported thermal analysis data indicates that T_m' for both the s.c. and fcc phase is below the cited temperature of transformation ($T_{t(s.c.)} = 350^{\circ}C$, $T_{t(fcc)} = 427^{\circ}C$) and both are also far from the values expected by simple extrapolation of the S/L phase boundaries to one atmos-

phere pressure on the equilibrium T-P diagram.

The inconsistency of both the calculated phase boundary slopes and approximated metastable melting points when compared to the equilibrium T-P diagram seems to arise from assumptions made (in the previous work) in measuring the ΔH_t values for each metastable phase. In producing these values a key assumption was made that equal amounts of each of the five metastable phases were present within a given splat-quenched foil. The resulting inconsistency of the current calculations indicates that this assumption is not valid.

2) Analysis of Current Results

As a liquid is progressively cooled below its equilibrium melting point it may become metastable not only with respect to the equilibrium solid phase, but also to solids which are thermodynamically disallowed under normal solidification conditions. Based upon extrapolation of the S/L phase boundaries to one atmosphere pressure on the equilibrium T-P diagram for Sb, an undercooling of only a few degrees is required to create a thermodynamic driving force for the formation of the metastable simple cubic Sb phase. As the undercooling exceeds this value the driving force for the

formation of both the equilibrium and metastable phase continues to increase. The solid which ultimately forms is determined by nucleation kinetics, with the phase having the lower barrier to nucleation at a given level of undercooling being favored. Thus both the thermodynamic driving force and favorable nucleation kinetics must be present in order to form the metastable solid from an undercooled melt.

The level of undercooling obtained in crushed Sb powder was well in excess of thermodynamic requirements for formation of the simple cubic phase. The occurrence instead of the equilibrium rhombohedral phase is thus attributed to nucleation kinetics which favored equilibrium phase formation.

Emulsified droplets experienced undercoolings slightly in excess of those produced in crushed powders thus increasing the driving force for formation of both the equilibrium and metastable phase. The production of an alternative coating on these droplets created a condition in which the nucleation kinetics for a significant portion of the sample favored the formation of simple cubic Sb. The importance of the droplet coating in influencing the nucleation kinetics may be seen by

comparing 88-150μm emulsified powder to 20-44μm crushed powder. Although the undercooling of the crushed powder exceeds that of the emulsified powder by approximately 15°C, a significant portion of the emulsified sample yields the metastable s.c. phase while the crushed droplets produce an entirely equilibrium structure.

Formation of a metastable product from the undercooled melt lowers the free energy of the system, however, there remains a driving force for the metastable→equilibrium solid-state transformation. Retention of the s.c. Sb phase following the relatively slow cooling of DTA to ambient temperatures, as well as evidence of the melting of this phase upon reheating, testifies to the stability of the metastable product. One reason for this stability lies in the single crystal nature of the emulsified powder. The lack of favorable grain boundary sites for initiation of decomposition encourages retention of the metastable structure.

Based upon x-ray diffraction data it is possible to calculate a lattice parameter for the simple cubic Sb phase. Results indicate a mean value of approximately 2.9350Å with a corresponding 95% confidence interval being given by:

$$2.8795\text{Å} \leqslant a_{s.c.} \leqslant 2.9905\text{Å}$$

This value, while representing only an approximation, compares favorably with the value of 3.05Å reported for the Sb simple cubic phase produced in an InSb-Sb alloy through splat-quenching (85). The slight discrepancy stems from a small amount of solid solution In trapped in the Sb during the splat-quenching process.

Indium Antimonide

Interpretation of the InSb results is complicated by an apparent deviation in composition from the nominal 50/50 at. %. As a result the undercooling of the Sb rich alloy may be influenced by the formation of a primary phase. The lack of an increasing deviation for crushed powder as the droplet size is reduced, as well as there being no similar shift in composition of the eutectic alloy powder, suggests that the deviation is not attributable to a coating reaction. Therefore, the underlying cause of the compositional shift appears to lie in a deviation in the original ingot composition.

The degradation in undercooling with thermal cycling for both the bulk sample and crushed powder stems from an adverse coating reaction at elevated temperature. The original coating is altered irreversibly

with each consecutive cycle which ultimately leads to an undercooling plateau of approximately $0.05T_L$ in both bulk and powder samples. Emulsification of the alloy imparts a somewhat more protective coating on the droplets which resists this adverse coating reaction to a large extent.

As with pure Sb, subdivision of the InSb alloy isolates the most potent nucleants into a small fraction of the droplets allowing the remainder to experience larger undercoolings. The pronounced shift in crystallization exotherms to lower temperatures as the droplet size is reduced from 88-150μm to 20-30μm attests to the effectiveness of this nucleant isolation method.

The presence of two major crystallization peaks upon cooling the molten (emulsified) powder implies that two catalytic sites operate within the droplet sample. The increased intensity of the exotherm occurring at the deeper level of undercooling with increased cooling rate implies that the more potent catalytic site has been kinetically bypassed in many of the droplets, allowing them to undercool to the point at which the less catalytic site initiates solidification.

InSb-Sb Eutectic Alloy

Application of the droplet technique to an InSb-Sb eutectic alloy has allowed examination of the nucleation and growth characteristics for this faceted/faceted eutectic at initial undercoolings ranging from 0.1 to 0.2 T_E. The combination of nucleant isolation (through control of droplet size) and a variation in applied cooling rate was effective at producing numerous, well defined undercooling levels within this range. A lack of solid solubility in both constituents tended to inhibit coarsening of the solidification microstructure (during subsequent cooling from nucleation to ambient temperature) by interphase volume diffusion; additionally, there was no microstructural evidence of fiber spherodization, the primary coarsening mechanism in this type of eutectic alloy (92).

Production of a normal-type eutectic structure from an undercooled melt requires both the successful nucleation of each constituent (virtually simultaneously) followed by growth of both phases at the same rate and with a common interface. The occurrence of such a structure in undercooled InSb-Sb droplets suggests that these requirements have been met and that a significant degree of cooperation has occurred between

the constituents during solidification. This implies that the entire solidification process (i.e. nucleation and subsequent recalescence) has occurred within the coupled zone and, furthermore, that this coupled region is somewhat symmetric about the eutectic composition.

Solidification of a eutectic alloy requires a diffusional sorting of the components in the liquid ahead of the advancing interface as well as the creation of surface area between the solid constituents. These requirements for coupled growth form the basis of the the relationship between interfacial undercooling (ΔT), eutectic spacing (λ) and interfacial velocity (R), namely:

$$\Delta T = (A_1/D_L(T))\,\lambda\, R + A_2/\lambda$$

where A_1 and A_2 are parameters approximated by $\bar{m}\Delta C/8$ and $2\gamma_{\alpha\beta}/\Delta S_f$ respectively; $\bar{m}$ is an average positive liquidus slope of the two phases, ΔC is the composition difference between the constituents, $\gamma_{\alpha\beta}$ is the surface energy between the solid phases, ΔS_f is the average entropy of fusion and D_L is the liquid interdiffusion coefficient (93). This governing expression permits a range of velocities for a given interface temperature depending on the spacing chosen. If growth is assumed to occur at the spacing which minimizes the interfacial

undercooling (i.e. the "extremum"), the velocity at which the eutectic structure can grow at a given interface temperature is given by:

$$R = D_L(T)(\Delta T)^2/4A_1A_2 \qquad (34)$$

and the eutectic spacing by:

$$\lambda = 2A_2/\Delta T \qquad (35)$$

Inclusion of a temperature dependent diffusion coefficient leads to a maximum velocity occurring at a certain level of undercooling, beyond which diffusion of the components in the liquid ahead of the interface limits the rate at which cooperative growth may occur. Using values of A_1 and A_2 determined by phase diagram and experimental (λ vs. ΔT_N) data (A_1 = 17.15°C and A_2 = 1.1 X 10^{-3}cm·K) it is possible to calculate the growth velocity as a function of interface temperature for the InSb-Sb eutectic. A plot of equation (34) is presented in Figure 61, based upon a diffusion coefficient of 2.1 X 10^{-5}cm^2/sec at T_E (83) and assuming Arrhenius behavior with an activation energy of 5kcal/mole·K to extend D_L to lower temperatures. A maximum growth rate of approximately 3.7cm/sec is predicted at a temperature of 268°C (ΔT = 232°C, 0.3 T_E). Should a larger activation energy be assumed, the result would be a decrease in the maximum growth rate and a shift

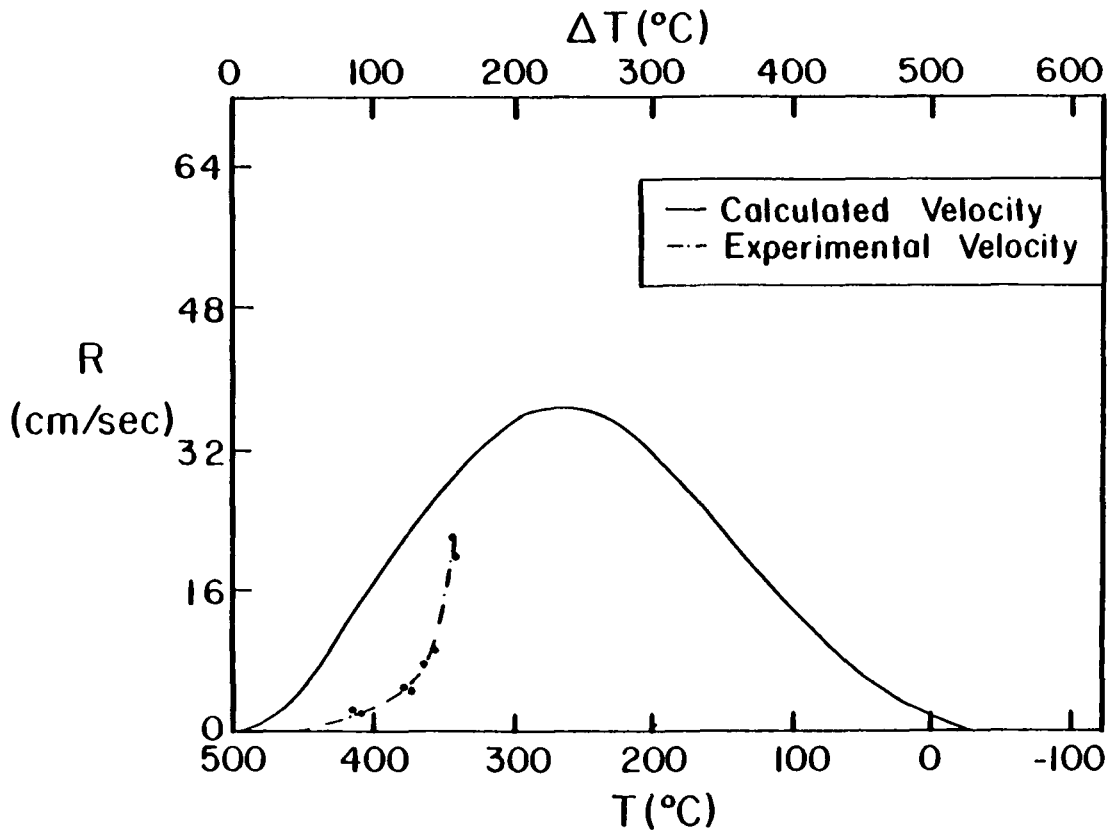

Figure 61. Comparison between calculated (extremum) growth rate and experimentally determined cooperative growth velocity as a function of interfacial undercooling.

in the corresponding undercooling to smaller values (e.g. for Q = 10kcal/mole·K, R_{max} = 1.26 cm/sec at $\Delta T \doteq 175^{o}C$, 0.23 T_E).

Experimentally determined values of R for ΔT = 0.1 to 0.2 T_E, also presented in Figure 61, are somewhat lower than those predicted by equation (34). The reason for this discrepancy may be related to the assumption of growth at the extremum. In eutectics having low entropy of fusion constituents both branching (to reduce spacing) and termination (to increase spacing) is relatively unconstrained, allowing growth to occur at or near extremum conditions. However, for eutectics such as InSb-Sb in which both phases have relatively large ΔS_f values, growth facets may form which inhibit the branching required to maintain the eutectic spacing at the value necessary for optimization of the growth rate. The eutectic spacing in this case lies between the value for extremum conditions (smaller values are inherently unstable) and a maximum spacing determined by morphological stability at the fiber tip (81). Thus, the faceted/faceted eutectic tends to have increased spacings and correspondingly larger interfacial undercoolings for a given growth velocity than those found in non-faceted eutectics. This may be seen by comparing the

$\lambda^2 R$ constant for InSb-Sb to that of a Ag-Cu (n.f./n.f.) eutectic (94):

$$\lambda^2 R_{(Ag\text{-}Cu)} = 1.4 \times 10^{-11} \text{ cm}^3/\text{sec}$$

$$\lambda^2 R_{(InSb\text{-}Sb)} = 1.8 \times 10^{-10} \text{ cm}^3/\text{sec}$$

The significantly larger value for the InSb-Sb alloy is consistent with branching limited growth theory for f./f. eutectics. It is interesting to note that, according to Figure 61, a maximum velocity could be achieved by extending the undercooling approximately 75°C (from the maximum experimental value). Should velocities greater than this maximum for eutectic growth be exceeded due to rapid heat extraction, the inability of this material to crystallize as a single phase could encourage the formation of a glass (95). Of course, before vitrification develops there may be a rapid solidification regime where coupled growth is not possible but independent formation and growth of each eutectic constituent develops to yield a biphasic mixture. Alternatively, while the metastable simple cubic Sb phase has not been produced at the present undercooling levels, extension of the liquid undercooling could produce the metastable product and thus avoid coupled growth of the equilibrium structure.

Directional solidification (D.S.) of InSb-Sb has produced both rod and lamellar-type structures, depending on the magnitude of the applied growth rate. At slow rates a rod structure forms due to the occurrence of a low-energy interface between the InSb $\{111\}$ and Sb $\{100\}$ planes, with formation of this interface requiring Sb rod growth in the preferred $[111]_{Sb}$ direction. However, since Sb has a high degree of thermal anisotropy, increasing the growth rate can force a deviation from the $[111]_{Sb}$ direction in order to allow alignment of the higher conductivity $(111)_{Sb}$ planes. This results in an increase in phase boundary energy as the low-energy orientation is destroyed thus encouraging a rod to lamellar transition (73).

The D.S. results offer a basis upon which to explain the observed microstructural transition in undercooled InSb-Sb droplets. Following the successful nucleation of both constituents, growth occurs, with the latent heat being absorbed by the undercooled liquid. Little heat transfer through the solid is required and the eutectic adopts the morphology which minimizes interphase boundary energy, namely a rod-type structure. This period of growth continues until external heat extraction (from the droplet surface) begins to assist

in removal of the latent heat. At this point the eutectic adopts a morphology most conducive to transfer of latent heat from the interface thus allowing for the most rapid growth of the solid. As indicated by D.S. studies, the most efficient heat transfer occurs by alignment of the $(111)_{Sb}$ planes and is accompanied by a rod to lamellar eutectic transition. The sharp morphology transition in undercooled InSb-Sb droplets may therefore be related to a change in heat flow conditions from one in which the undercooled liquid absorbs the latent heat, to one in which external heat flow becomes important. In support of this hypothesis, the rod structure undergoes a continuous increase in spacing from the nucleation region to the morphological transition zone (reflecting the continual decrease in interfacial undercooling associated with recalescence) while, following the transition to a lamellar structure, the spacing is approximately constant for the remainder of solidification (implying a relatively constant interfacial undercooling). Figure 62 presents a schematic illustration of the proposed thermal history for an undercooled InSb-Sb eutectic droplet. Following nucleation (point 1) recalescence occurs to a temperature, T_R, (point 2) at which external heat flow begins to dominate. The temperature (and thus undercooling)

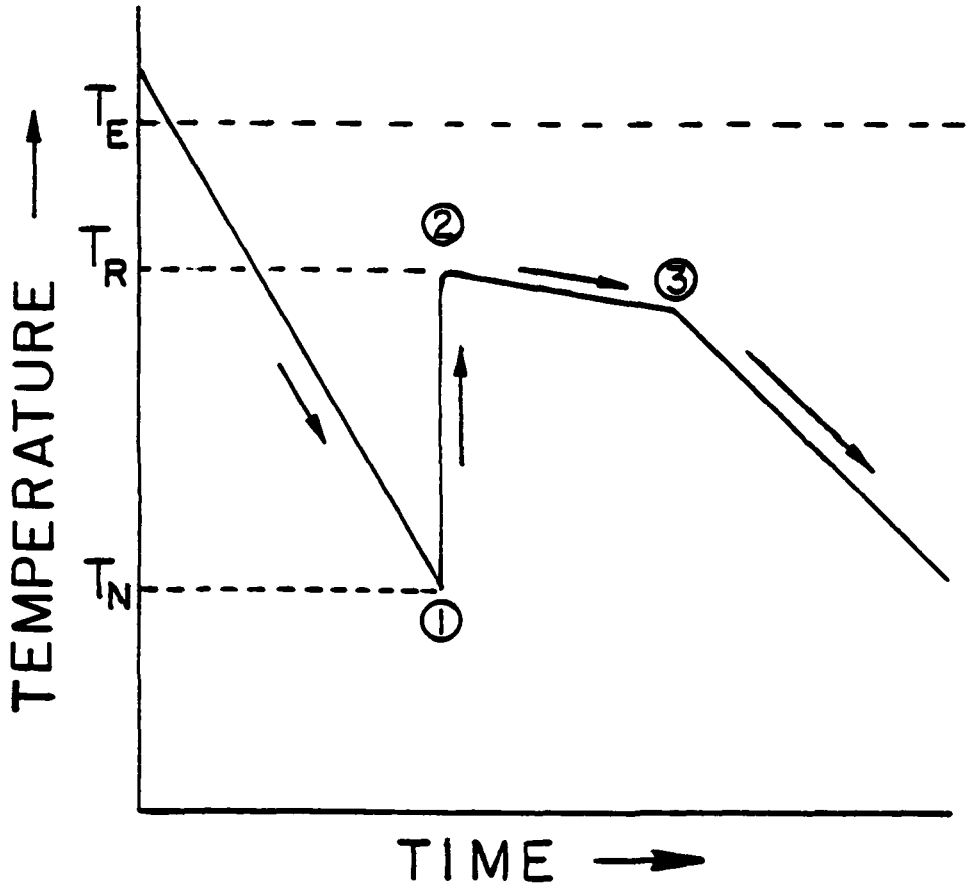

Figure 62. Proposed thermal history of an undercooled InSb-Sb eutectic droplet. Path 1→2 represents recalescence and corresponds to rod-type eutectic growth. Path 2→3 represents external heat flow dominance and corresponds to lamellar-type eutectic growth. Solidification is completed at point 3.

then remains approximately constant for the remainder of solidification (i.e. to point 3).

The microstructural transition which occurs in the InSb-Sb eutectic provides insight into the temperature distribution in the droplet prior to the onset of solidification. As illustrated in Figure 51, the transition zone (and thus the S/L interface at that position) is approximately hemispherical in shape, suggesting that Newtonian conditions existed within the droplet prior to nucleation (90).

Use of the λ vs. ΔT_N data to provide information on interfacial undercooling during recalescence, while representing only an approximation, indicates that a significant degree of undercooling remains at the onset of the morphological transition. If this transition is taken to represent the termination of recalescence, the remaining stage of droplet solidification is clearly nonadiabatic. Furthermore, as the droplet size is reduced, the deviation from adiabaticity increases (i.e. ΔT_{min} departs further from zero). This trend is similar to that sited by Clyne et al (96) for Al droplets in which, as the droplet size was reduced, a corresponding increase in heat transfer coefficient (h) occurred. The increase in h was significant enough

to reduce the ultimate recalescence temperature of the droplet. While this critical level of h was proposed only for droplets less than approximately 3μm in diameter for pure Al, the cooperative growth of the eutectic with the accompanying greatly reduced interfacial velocity may extend this critical droplet size, or equivalently, reduce the value of h necessary to alter the ultimate recalescence temperature.

The occurrence of a normal-type eutectic structure in an InSb-Sb alloy provides an opportunity to evaluate the undercooling produced in processes for which direct temperature measurement is difficult, by a postmortem examination of the solidification microstructure. This technique has provided seemingly reasonable estimates of the undercooling produced in drop tube processed samples, whose accuracy has been enhanced by minimizing the need to extrapolate to values of ΔT_N beyond the range of those directly measured (using DSC, etc.). The significant levels of undercooling achieved through drop tube processing of the InSb-Sb droplets, both under vacuum (0.17 T_E) and helium (0.23 T_E) conditions, testifies to the potential of containerless processing for the inducement of rapid

solidification effects. In fact, the largest level of undercooling (and correspondingly highest initial solidification rate) was produced through drop tube processing of the eutectic powder. In addition, characterization of the crystallization behavior of this material has provided insight into both the factors which influence liquid undercooling as well as conditions which exist during droplet solidification. The undercooling potential, while effectively demonstrated in this relatively low melting point eutectic alloy, could become even greater for higher temperature alloys (such as Fe and Ni-based) in which the cooling rate during processing may be enhanced by the contribution of radiation heat loss from the droplet surface. Thus, based upon current results, drop tube processing appears to offer conditions favorable to production of rapid solidification effects in droplet samples.

SUMMARY AND CONCLUSIONS

Use of the droplet emulsion technique has been effective in increasing the undercooling potential for pure Sb, InSb and an InSb-Sb eutectic alloy. Subdivision of the bulk ingot into droplets of size 10-150μm isolates the most potent nucleants into a small fraction of the droplet population, allowing the remainder to experience greater levels of undercooling. The application of higher cooling rates (10^{2}°C/sec) can also assist in extending the metastable liquid state to lower temperatures by kinetically bypassing certain of the remaining catalytic sites. Of significant importance in determining both the extent of undercooling and the resulting solidification product structure is the droplet surface coating; initial ingot purity and level of applied superheat are of lesser importance.

Through proper control of the droplet size and surface coating the maximum undercooling of pure Sb has been extended from 0.08 to $0.23T_m$. While simple crushing of the material is effective at increasing the undercooling through nucleant isolation, the oxide surface coating encourages formation of the equilibrium Sb structure. Using emulsification techniques an alternative coating is produced which provides condi-

tions under which nucleation kinetics favorable to the formation of a metastable simple cubic Sb phase can operate. The single crystal nature of the droplets allows retention of the metastable product to temperatures approaching the melting point. The simple cubic phase has been detected in emulsified droplets processed in a variety of ways including DTA, air and water quench and drop tube processing under a helium gas atmosphere. X-ray diffraction results indicate a lattice parameter of approximately 2.9350Å for the simple cubic structure.

A deviation in the InSb parent ingot composition limited interpretation of the line compound results, however emulsification techniques still proved effective at extending the undercooling of this material to approximately $0.17T_L$. Both bulk and crushed powder samples revealed a large degradation in undercooling following initial cycling to elevated temperatures. Emulsification of the alloy significantly reduced this effect by providing a more protective surface coating on the droplets.

Following evaluation of the undercooling and crystallization behavior of the pure constituents, Sb and InSb, examination of a eutectic mixture of these

phases was carried out. The droplet emulsion technique was effective at producing various levels of undercooling between 0.1 and 0.2 T_E, primarily through control of droplet size and applied cooling rate. Microstructural examination of the faceted/faceted alloy revealed the formation of a normal-type eutectic structure in the undercooled droplets indicating that the entire solidification process (i.e. nucleation and subsequent recalescence) occurred within the coupled growth region and, furthermore, that this region was somewhat symmetric about the eutectic composition. This enabled a correlation to be made between initial interphase spacing and undercooling at nucleation, the results of which provide the relationship:

$$\ln\lambda(\text{Å}) = 14.94 - 1.56 \ln \Delta T(^{\circ}C)$$

in approximate agreement with eutectic growth theory.

Based upon directional solidification data, an expression relating growth velocity to eutectic spacing was developed and used to estimate growth rates at the onset of solidification. The increase in undercooling (0.1 to 0.2 T_E) led to a reduction in spacing from 2750 to 930 Å and a corresponding increase in growth velocity from 0.23 to 2.2 cm/sec. A theoretical

calculation of growth rate as a function of interface temperature, based upon an assumption of growth at the extremum and using experimentally determined constants, predicts a maximum velocity of 3.7cm/sec at an undercooling of 0.3 T_E. While only an approximation, the calculation supports use of the (D.S.) growth rate expression over the range of undercoolings obtained in this investigation.

A morphological transition from a rod to lamellar structure is observed during solidification which may be attributed to a change in heat flow conditions from one in which the undercooled liquid absorbs the latent heat, to one in which external heat flow becomes important. The thermal anisotropy of Sb encourages a change in growth orientation to allow alignment of the high conductivity (111) planes as external heat flow begins to remove the latent heat originating at the interface. This change in growth orientation destroys the low energy orientation relationship between the Sb rods and InSb matrix causing the transition from a rod to lamellar structure. In addition, the hemispherical shape of this transition region indicates that Newtonian conditions held prior to the onset of solidification.

The eutectic spacing, measured as a function of fraction solidified within the droplet, provides insight into the growth conditions during recalescence. Following nucleation, the rod spacing continually increases (or equivalently the growth velocity decreases) until the transition zone is reached. If the transition is taken to represent the end of recalescence, the droplet solidification must be nonadiabatic due to the nonzero value of undercooling present at this point. Moreover, the undercooling remaining at the transition region increases as the droplet size is reduced. A possible explanation is that, due to the relatively slow growth rate required for cooperative growth of the eutectic (compared to that of a dilute alloy at equivalent undercooling), the external cooling rate is more effective at reducing the degree of recalescence. In addition, as the droplet size is reduced, the effect of heat transfer to the surrounding may become more significant, accounting for the larger transition undercoolings in the finer droplets.

Extension of this approach has allowed estimation of the undercooling produced during drop tube processing of the eutectic powder under both vacuum and helium atmospheres. Estimated nucleation undercoolings

of 0.17 and 0.23 T_E were obtained for vacuum and helium processed samples, respectively.

RECOMMENDATIONS

1) The production of an alternative surface coating for pure Sb should be attempted through use of an appropriate carrier medium. The thickness of the $ZnSb_2O_4$ coating present on the Sb droplets in this study inhibited accurate sizing of the powder and complicated x-ray diffraction analysis.
2) Further thermal analysis of pure Sb should be carried out in order to define the melting behavior of the metastable simple cubic phase more accurately.
3) Use of an InSb ingot of precise composition should allow examination of the pure constituent by eliminating possible primary phase formation effects.
4) Melt spinning (or similar rapid heat extraction methods) should be employed with the eutectic alloy in order to determine the effect of exceeding the theoretical growth velocity limit for coupled growth. This may lead to the formation of a glass.
5) Analysis of the eutectic spacing as a function of fraction solid should be made for drop tube samples processed under various gas atmospheres (such as He, Ar, N_2 etc.). The change in thermal conductivities should produce a variation in undercooling and provide insight into the effect of an alteration in

heat transfer coefficient on the morphological transition in the undercooled droplets.

6) A detailed analysis of the post-transition eutectic spacing should be carried out in order to understand better the growth conditions during this phase of solidification.

7) Investigation of the eutectic spacing/undercooling relationship in similar faceted/faceted alloys, such as InSb-NiSb, could provide further insight into cooperative growth of f./f. eutectics.

BIBLIOGRAPHY

1. B.C. Giessen, "Developments in the Structural Chemistry of Alloy Phases", B.C Giessen (Ed.), Plenum Press, N.Y., 227 (1969).

2. J.Z. Kattamis and M.C. Flemings, Trans. A.F.S. 75, 195 (1967).

3. J.H. Perepezko and I.E. Anderson, "Synthesis and Properties of Metastable Phases", Machlin and Rowland (Eds.), TMS-AIME (1980).

4. J.C. Baker and J.W. Cahn, "Solidification", ASM, Metals Park, OH, 23 (1971).

5. G.A. Colligan and B.J. Bayles, Acta Met. 10, 895 (1962).

6. J.L. Walker, "Physical Chem. of Process Met. Part II", G.R. St. Pierre (Ed.), Interscience Pub., N.Y., 845 (1961).

7. J.Z. Kattamis and M.C. Flemings, Trans. of Met. Soc. AIME 236, 1523 (1966).

8. G.J. Abbaschian and M.C. Flemings, Met. Trans. 14A, 1147 (1983).

9. L.L. Lacy, M.B. Robinson, and T.J. Rathz, J. Crystal Growth 51, 47 (1981).

10. J.H. Perepezko, D.H. Rasmussen, I.E. Anderson and C.R. Loper Jr., Sheffiels Conf. on "Solidification and Casting of Metals", The Metals Society, London, 169 (1979).

11. S.Y. Shiraishi and R.G. Ward, Canadian Met. Quart. 3, 117 (1964).

12. B. Vonnegut, J. Colloid Sci. 3, 563 (1948).

13. D. Turnbull and R.C. Cech, J. Applied Phys. 21, 805 (1950).

14. C.C. Wang and C.S. Smith, J. of Metals 188, 136 (1950).

15. R.T. Southin and G.A. Chadwick, Acta Met. 26, 223 (1978).

16. T.R. Anantharaman and C. Suryanarayana, J. Mat. Sci. 6, 1111 (1971).

17. E. Meyer and L. Rinderer, J. Crystal Growth 28, 199 (1975).

18. R.E. Cech and D. Turnbull, Trans. AIME 206, 124 (1956).

19. J.H. Perepezko, "Rapid Solidification Processing: Principles and Technologies II", M. Cohen, B.H. Kear and R. Mehrabian (Eds.), Claitor's Pub., Baton Rouge, LA, 56 (1980).

20. D.R. Rasmussen and C.R. Loper, Acta Met 24, 117 (1976).

21. J.J. Richmond, M.S. Thesis, Univ. of Wis.-Madison (1983).

22. J. Feder, K.C. Russell, J. Lothe and G.M. Pound, Advances in Physics 15, 111 (1966).

23. D. Turnbull, J. Chem. Phys. 20, 411 (1952).

24. B. Vonnegut, J. Appl. Phys. 18, 593 (1947).

25. B. Chalmers, "Growth and Perfection of Crystals", R.H. Doremus, D. Turnbull and B.W. Roberts (Eds.), John Wiley and Sons, N.Y., 291 (1958).

26. J.W. Cahn, W.B. Hillig and G.W. Sears, Acta Met. 12, 1421 (1964).

27. K.A. Jackson, "Crystal Growth and Characterization", R. Ueda and J.B. Mullin (Eds.), North-Holland, Amsterdam, 21 (1975).

28. J.W. Cahn, Acta Met. 10, 161 (1962).

29. M.C. Flemings, "Solidification Processing", McGraw-Hill, 301 (1974).

30. J.H. Magill and D.J. Plazek, J. Chem. Phys. 46, 3757 (1967).

31. G.A. Alfintsev and D.E. Ovsienko, Sov. Phys.-Dolk. 9, 489 (1964).

32. F.C. Frank, Dis. Faraday Soc. 5, 48 (1949).

33. E. Billig, Proc. Roy. Soc. (London) 229, 346 (1955).

34. R.S. Wagner, Acta Met. 8, 57 (1960).

35. D.R. Hamilton and R.G. Seidensticker, J. App. Phys. 31, 1165 (1960).

36. N. Albon and A.E. Owen, J.Phys. Chem. Solids 24, 899 (1963).

37. H.D. Keith and F.J. Padden Jr., J. App. Phys. 34, 2409 (1963).

38. K.F. Hulme and J.B. Mullin, Phil Mag. 4, 1286 (1959).

39. B. Cockayne, J. Crystal Growth 3, 60 (1968).

40. M.E. Glicksman and R.J. Schaefer, J. Crystal Growth 1, 297 (1967).

41. R.J. Schaefer and M.E. Glicksman, J. Crystal Growth 5, 44 (1969).

42. S.C. Huang and M.E. Glicksman, Acta Met. 29, 701 (1981).

43. L. Bosio, A. Defrain and K. Epelboin, Le J. de Physique 27, 61 (1966).

44. L. Bosio, A. Defrain and M. Dupont, J. Chem. Phys. 68, 542 (1971).

45. A. Bizid, L. Bosio, H. Curien, A. Defrain and M. Dupont, Phys. Stat. Sol. 23, 135 (1974).

46. J.H. Perepezko, C. Galup and D.H. Rasmussen, Proceedings of the 3rd European Symposium on Materials Science in Space (1979).

47. D. Akhtar, V.D. Vaknar, J.C. Goel and K.L. Chopra, J. Mat. Sci. 14, 998 (1979).

48. P. Bridgman, Proc. Am. Acad. Act. Sci. 74, 425 (1942).

49. L.F. Vereshchagin, A.A. Semerchan, N.N. Kuzin and S.V. Popova, Sov. Phys.-Dok. 6, 41 (1961).

50. S.S. Kabalkina and V.P. Mylov, Sov. Phys.-Dok. 8, 917 (1964).

51. W. Klement Jr., A. Jayaraman and G.C. Kennedy, Phys. Rev. 131, 632 (1963).

52. S. M. Stishov and N.A. Tikhomivova, J. Exptl. Theoret. Phys. (U.S.S.R.) 48, 1215 (1965).

53. S.A. Ivakhnenko and Ye. G. Ponyatovsky, Phys. Met. Metall. 47, 1314 (1979).

54. V.P. Butuzov, E.G. Ponystovski and G.P. Shakhovskii, Transl. of Dokl. Akad. Nauk. SSSR 109, 519 (1956).

55. G.C. Kennedy and R.C. Newton, in "Solids Under Pressure", W. Paul and D.M. Warschauer (Eds.), McGraw-Hill Book Co., N.Y., 163 (1963).

56. C.W.F.J. Pistorius, Pro. Sol. St. Chem. 11, 1 (1976).

57. M.J. Duggin, J. Phys. Chem. Sol. 33, 1267 (1972).

58. D. Akhtar, V.D. Vankar, J.C. Goel and K.L. Chopra, J. Mat. Sci. 14, 2422 (1979).

59. D. Akhtar, V.D. Vankar, J.C. Goel and K.L. Chopra, Thin Solid Films 58, 327 (1979).

60. F.L. Brady, J. Inst. Metals 28, 369 (1922).

61. A.M. Portevin, J. Inst. Metals 29, 239 (1923).

62. E. Scheil, Z. Metallk 45, 298 (1954).

63. L.M. Hogan, R.W. Kraft and F.D. Lemkey, "Advances in Materials Research", H. Herman (Ed.) 5, John Wiley & Sons, N.Y., 83 (1971).

64. V. de L. Davies, J. Inst. Metals 93, 10 (1964).

65. J.A.E. Bell and W.C. Winegard, J. Inst. Metals 93, 457 (1964).

66. W.M. Rumball and V. Kondec, "The Solid of Metals", Iron and Steel Inst. Pub. 110, London, 149 (1967).

67. C.W. Haworth and E.P. Whelan, J. Aust. Inst. Metals 10, 184 (1965).

68. J.D. Hunt and K.A. Jackson, Trans. Met. Soc. AIME 236, 843 (1966).

69. R.S. Fidler, M.N. Crocker and R.W. Smith, J. Crystal Growth 13/14, 739 (1972).

70. M.N. Crocker, R.S. Fidler and R.W. Smith, Proc. Roy. Soc. London 335, 15 (1973).

71. J.D. Hunt and D.T.J. Hurle, Trans. Met. Soc. AIME 242, 1043 (1968).

72. H.E. Cline, J.L. Walter, E. Lifshin and R.R. Russell, Met. Trans. 2, 189 (1971).

73. M.N. Crocker, M. McParlan, D. Garagor and R.W. Smith, J. Crystal Growth 29, 85 (1975).

74. A. Kofler, Z. Metallk. 41, 221 (1950).

75. J.D. Hunt and J.P. Chilton, J. Inst. Metals 91, 338 (1962).

76. K.A. Jackson and J.D. Hunt, Trans. Met. Soc. AIME 236, 1129 (1966).

77. D.J. Fisher and W. Kurz, Acta Met. 28, 777 (1980).

78. A. Moore and R. Elliott, "The Solid. of Metals", Iron and Steel Inst. Pub. 110, London, 167 (1967).

79. W.J. Boettinger, R.J. Schaefer, F. Biancaniello and D. Shechtman, "Rapid Solid. Processing: Prin. and Tech. (III)", R. Mehrabian (Ed.), N.B.S. Internal Report (1983).

80. H.E. Cline, J.L. Walker, E. Lifshin and R.R. Russell, Met. Trans. 2, 189 (1979).

81. D.J. Fisher and W. Kurz, Acta Met. 28, 777 (1980).

82. M. Hanson, "Const. of Binary Alloys", McGraw-Hill Book Co., N.Y. (1958).

83. W.K. Liebmann and E.A. Miller, J. App. Phys. 34, 2653 (1963).

84. B.C. Giessen, U. Wolff and N.J. Grant, Trans. Met. Soc. AIME 242, 597 (1968).

85. C.B. Jordan, J. Chem. Phys. 39, 1613 (1963).

86. S. LeBeau, Ph.D. Thesis, Univ. of Wisconsin-Madison, (1982).

87. B. Mueller, M.S. Thesis, Univ. of Wisconsin-Madison, (1983).

88. J. Regan, M.S. Thesis, Univ. of Wisconsin-Madison, (1983).

89. G.E.P. Box, W. Hunter, J.S. Hunter, "Statistics for Experimenters", Bradley, Hunter, Kendall and Watson (Eds.), John Wiley & Sons, N.Y. (1978).

90. C.G. Levi and R. Mehrabian, Met. Trans. 13A, 221 (1982).

91. J.H. Perepezko and J.S. Paik, Proceeding of the MRS Symp.: Rapidly Solid. Am. and Cryst. Alloys", B.H. Kear and B.C. Giessen (Eds.), North Holland, N.Y., (1982).

92. T.F. Marinis and R.F. Sekerka, "In-Situ Composites IV", F.D. Lemkey, H.E. Cline and M. McClean (Eds.), Elsevier Sci. Pub., 315 (1982).

93. W.J. Boettinger, "Rapidly Solidified Amorphorous and Crystalline Alloys", B.H. Kear, B.C. Giessen and M. Cohen (Eds.), North-Holland, N.Y., 15 (1982).

94. W.J. Boettinger, D. Shechtman, R.J. Schaefer and F.S. Biancaniello, Met. Trans. 15A, 55 (1984).

95. W.J. Boettinger, F.S. Biancaniello, G.M. Kalonji and J.W. Cahn, "Rapid Solidification Processing: Principles and Technologies II", R. Mehrabian, B.H. Kear and M. Cohen (Eds.), Claitor's, Baton Rouge, LA, 50 (1980).

96. T.W. Clyne, R.A. Ricks and P.J. Goodhew, Intl. J. Rapid Solid. 1, 59 (1984).

1. Report No	2 Government Accession No	3 Recipient's Catalog No
NASA CR-175013		

4. Title and Subtitle	5 Report Date
Undercooling and Solidification Behavior in the InSb-Sb System	September 1985
	6 Performing Organization Code

7. Author(s)	8. Performing Organization Report No
J.A. Graves	None
	10 Work Unit No

9 Performing Organization Name and Address	11 Contract or Grant No
University of Wisconsin Madison, Wisconsin	NAS 3-14
	13 Type of Report and Period Covered
	Contractor Report

12. Sponsoring Agency Name and Address	14 Sponsoring Agency Code
National Aeronautics and Space Administration Washington, D.C. 20546	505-63-01

15 Supplementary Notes

Final report. Project Manager, T.K. Glasgow, Materials Division, NASA Lewis Research Center, Cleveland, Ohio 44135. This report was submitted in partial fulfillment of the requirements for the degree Master of Science to University of Wisconsin.

16. Abstract

Use of the droplet emulsion technique has been successful in studying the undercooling and crystallization behavior of Sb, InSb, and an InSb-Sb eutectic alloy. Both droplet size and imposed cooling rate were influential in controlling the extent of liquid undercooling. The droplet surface coating was of significant importance in determining the resultant solidification product structure through its effect on nucleation kinetics. The maximum undercooling for pure Sb was extended from 0.08 to 0.23 T_m. While simple crushing techniques provided a dramatic increase in droplet undercooling over the bulk material, emulsification treatments both enhanced this undercooling and allowed successful formation of a metastable simple cubic Sb phase. This phase was stable to temperatures approaching the melting point. The simple cubic phase was detected in droplet samples processed using DTA, air and water quenching, and drop tube processing under a helium gas atmosphere. A deviation in the InSb parent ingot composition limited interpretation of the line compound results, however emulsification techniques extended the undercooling of this material to 0.17 T_L and provided a stable, protective surface coating for the droplets. Emulsification of the eutectic alloy was effective at producing various levels of undercooling from 0.1 to 0.2 T_E. Microstructrual examination revealed a normal-type eutectic structure in the undercooled droplets indicating that solidification occurred within the coupled zone and that this zone is somewhat symmetric about the eutectic composition. A correlation was made between the initial interphase spacing and nucleation undercooling which yielded a quantitative relationship in agreement with eutectic growth theory. Initial growth rates were estimated based upon directional solidification data. The increase in undercooling (0.1 to 0.2 T_E) led to a reduction in initial spacing from 2750 to 930 Å and a corresponding increase in growth velocity from 0.23 to 2.2 cm/sec. A morphological transition from a rod to lamellar structure occurred during solidification and was attributed to a change in heat flow conditions from one in which the undercooled liquid absorbs the latent heat, to one in which external heat flow becomes important. Based upon eutectic spacing variation with fraction solidifed, a certain level of undercooling apparently remained following droplet recalescence. This undercooling level increased as the droplet size was reduced. The effectiveness of external cooling in limiting the degree of recalescence was attributed to the relatively slow growth rate required for cooperative eutectic growth. Extension of this approach allowed estimation of the undercooling produced during containerless drop tube processing of the eutectic powder. Estimated undercoolings of 0.17 and 0.23 T_E were obtained under vacuum and helium conditions respectively.

17. Key Words (Suggested by Author(s))	18 Distribution Statement
Undercooling; Nucleation; Atomization; Eutectics	Unclassified - unlimited STAR Category 26

19 Security Classif (of this report)	20. Security Classif. (of this page)	21. No. of pages	22 Price*
Unclassified	Unclassified	216	A10

*For sale by the National Technical Information Service, Springfield, Virginia 22161